

รายงานวิจัยฉบับสมบูรณ์

โครงการ: การแก้ปัญหาย้อนกลับร่วมสำหรับข้อมูลคลื่น
แม่เหล็กไฟฟ้าและไฟฟ้า

(Joint inversion for electromagnetic and electrical data)

รศ. ดร. วีระชัย สิริพันธ์วรารักษ์

ภาควิชาฟิสิกส์ คณะวิทยาศาสตร์ มหาวิทยาลัยมหิดล

สนับสนุนโดยสำนักงานกองทุนสนับสนุนการวิจัย
และมหาวิทยาลัยมหิดล

(ความเห็นในรายงานนี้เป็นของผู้วิจัย สกว. ไม่จำเป็นต้องเห็นด้วยเสมอไป)

บทคัดย่อ

รหัสโครงการ : RSA5780010

ชื่อโครงการ : การแก้ปัญหาย้อนกลับร่วมสำหรับข้อมูลคลื่นแม่เหล็กไฟฟ้าและไฟฟ้า

นักวิจัย : รศ. ดร. วีระชัย สิริพันธุ์วรารมณ
ภาควิชาฟิสิกส์ คณะวิทยาศาสตร์ มหาวิทยาลัยมหิดล

อีเมล : wsiripun@gmail.com; weerachai.sir@mahidol.ac.th

ระยะเวลาโครงการ: 16 มิ.ย. 2557 – 15 มิ.ย. 2560

ในโครงการนี้ เราได้พัฒนาโปรแกรมใหม่ที่ใช้ในการแปลความหมายข้อมูลธรณีฟิสิกส์ร่วมกันของสอง การสำรวจ ได้แก่ การวัดสภาพต้านทานไฟฟ้าด้วยไฟฟ้ากระแสตรง (DC Resistivity Survey) และการสำรวจแมกนีโตเทลลูริกซ์ (Magnetotelluric) ซึ่งเป็นการสำรวจโดยใช้คลื่นแม่เหล็กไฟฟ้า ทั้งสองเทคนิค จะให้ค่าสภาพต้านทานไฟฟ้าออกมา เพื่อนำไปใช้ในการแปลความหมายทางธรณีวิทยาต่อไป โปรแกรมนี้จะรวมเอาข้อดีของแต่ละเทคนิคไว้ด้วยกัน และกำจัดข้อด้อยของแต่ละเทคนิคออกไป กล่าวคือ เทคนิคการสำรวจสภาพต้านทานไฟฟ้าด้วยไฟฟ้ากระแสตรงจะให้สภาพต้านทานไฟฟ้าในบริเวณตื้น และรายละเอียดตามแนวนอนได้ดี ส่วนเทคนิคแมกนีโตเทลลูริกซ์จะให้สภาพต้านทานไฟฟ้าในระดับลึกได้ดี และรายละเอียดตามแนวนอนจะดีกว่า เมื่อรวมทั้งสองเทคนิค ก็จะทำให้สภาพต้านทานไฟฟ้าที่ดีทั้งในระดับตื้นและระดับลึก ปัญหาหลักของเทคนิคแมกนีโตเทลลูริกซ์ คือ ข้อมูลมักถูกบิดเบือน (distort) ด้วยสภาพธรณีวิทยาระดับตื้น เช่นโครงสร้างที่มีค่าสภาพต้านทานไฟฟ้าที่สูงมาก หรือต่ำมากที่อยู่ใกล้พื้นผิว เมื่อถูกบิดเบือน การนำเอาข้อมูลไปใช้งานโดยตรงก็ทำให้เกิดการแปลความหมายที่ผิดพลาดได้ ดังนั้น การทำสำรวจร่วม เพื่อเอาข้อมูลระดับตื้นที่ได้จากเทคนิคการวัดสภาพต้านทานไฟฟ้าด้วยไฟฟ้ากระแสตรงไปช่วยแก้ไข จะช่วยให้การแปลความของข้อมูล MT ได้ถูกต้องมากขึ้น

นอกจากนี้ ในโครงการ นอกจากจะพัฒนาโปรแกรมแปลความหมายร่วมแล้ว และทดสอบโปรแกรมกับข้อมูลเทียมแล้ว ผู้ดำเนินโครงการยังได้นำเอาโปรแกรมนี้ไปใช้งานจริง ในการสำรวจเพื่อหาแหล่งพลังงานความร้อนใต้พิภพ ในพื้นที่แม่จัน และฝาง ร่วมทั้งใช้ในการสำรวจเพื่อหาสาเหตุที่ทำให้รอยเลื่อนแม่ลาวเคลื่อนตัว ส่งผลให้เกิดแผ่นดินไหวครั้งใหญ่ที่สุดในประเทศอีกด้วย

คำหลัก: การแก้ปัญหาย้อนกลับ เทคนิคการวัดสภาพต้านทานไฟฟ้าด้วยไฟฟ้ากระแสตรง
เทคนิคแมกนีโตเทลลูริกซ์ พลังงานความร้อนใต้พิภพ แผ่นดินไหวแม่ลาว

Abstract

Project Code : RSA5780010

Project Title : Joint inversion for electromagnetic and electrical data

Investigator : Associate Professor Dr. Weerachai Siripunvaraporn
Department of Physics, Faculty of Science, Mahidol University

E-mail Address : wsiripun@gmail.com

Project Period : 16 June 2014 – 15 June 2017

In this project, we have developed a joint inversion program of the direct current resistivity (DCR) method and the magnetotelluric (MT) method. Both techniques yield resistivity cross-section of the survey area which can later be linked to the geology for the interpretation. The developed joint inversion program merges pros of both techniques together, and at the same time overcome the cons of both techniques. The DCR method often yields the resistivity cross-section only of the near subsurface but provide high lateral resolution, while MT can yield deeper structure with lesser lateral resolution. By combining both data sets, our joint inversion program can provide resistivity cross-section of both shallow and deeper structures. One major problem for the MT survey is the data distortion mainly by geology of the subsurface such as very high or resistivity bodies in the near surface. Without correction, the distorted data can mislead the interpretation. A joint survey can also help overcome this problem. A near surface resistivity from the DCR survey can be used to correct the MT distortion which will help guide the interpretation to the right direction.

In addition, in this project, besides testing our code with the synthetic data, we also used the code in the real surveys to explore the geothermal system of Mae Chan and Fang, and also used to investigate the cause of the slip of the Mae Lao fault which produce the largest earthquake in Thailand history.

Keywords: inverse problem, DC resistivity, magnetotelluric, geothermal system, Mae Lao earthquake

กิตติกรรมประกาศ

ข้าพเจ้าขอขอบคุณ สำนักงานกองทุนสนับสนุนการวิจัย (สกว.) และ มหาวิทยาลัยมหิดล ที่ให้โอกาสข้าพเจ้าได้ทำวิจัยในเรื่องที่ข้าพเจ้าถนัดต่อเนื่องมาตลอด สามารถทำให้ข้าพเจ้าได้ใช้เวลาทำงานวิจัยได้อย่างเต็มที่และทำงานวิจัยที่มีคุณภาพเป็นที่ยอมรับในกลุ่มคนทำวิจัยด้วยกัน ทูนิวิจัยนี้ยังสามารถทำให้ข้าพเจ้าได้ใช้เวลาเต็มที่ ในการพัฒนานักศึกษาในการทำวิจัยในสาขาธรณีฟิสิกส์อีกด้วย ซึ่งจะเป็นประโยชน์ต่อประเทศมากมาย เพราะนักศึกษาที่จบออกมามีคุณภาพและผลงานที่เทียบเท่ากับมาตรฐานสากล

นอกจากนี้ ข้าพเจ้าขอขอบคุณ ท่านหัวหน้าภาควิชา คณาจารย์ของทั้งภาควิชาฟิสิกส์ที่ช่วยสนับสนุนข้าพเจ้ามาโดยตลอด รวมทั้งท่านคณบดีและทีมงานคณะวิทยาศาสตร์ มหาวิทยาลัยมหิดล ที่คอยกระตุ้นและสนับสนุนงานวิจัยมาตลอด และที่สำคัญที่สุดคือ นักศึกษาและบุคลากร ในกลุ่มวิจัยธรณีฟิสิกส์ ภาควิชาฟิสิกส์ คณะวิทยาศาสตร์ มหาวิทยาลัยมหิดล ที่ร่วมกันฝ่าฟันอุปสรรคต่างๆ เพื่อความเป็นเลิศในงานวิจัยด้านนี้ ทั้งเหน็ดเหนื่อยในการออกภาคสนามเก็บข้อมูล และร่วมกันประมวลผลข้อมูลจำนวนมหาศาล รวมทั้งรวมกันเรียนรู้สิ่งใหม่ๆ อีกกลุ่มหนึ่งที่ข้าพเจ้าจะไม่ขอบคุณไม่ได้ คือ บุคลากรของสกว. ฝ่ายวิชาการ ทุกๆ คน ที่เป็นมิตรอันดี และคอยช่วยเหลือในเรื่องต่างๆ เป็นอย่างดี

สุดท้ายนี้ ข้าพเจ้าต้องขอขอบคุณบุคคลที่คอยเป็นกำลังใจ เข้าใจในทุกสิ่งทุกอย่าง บุคคลเหล่านี้คือ ภรรยาข้าพเจ้า ลูกสาวสุดที่รัก คุณแม่และคุณพ่อที่ล่วงลับไปแล้ว และครอบครัวพี่น้องของข้าพเจ้า ขอขอบคุณมากครับ

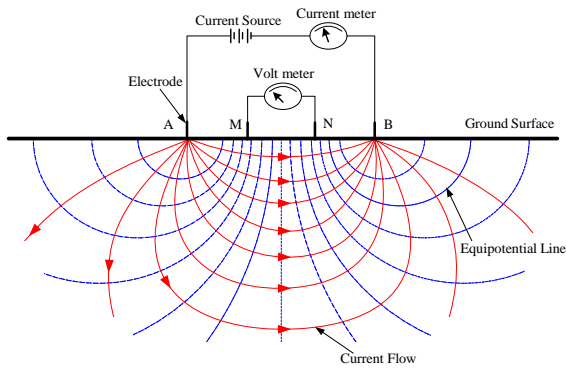
รศ. ดร. วีระชัย สิริพันธ์วรารณ

1. บทนำ

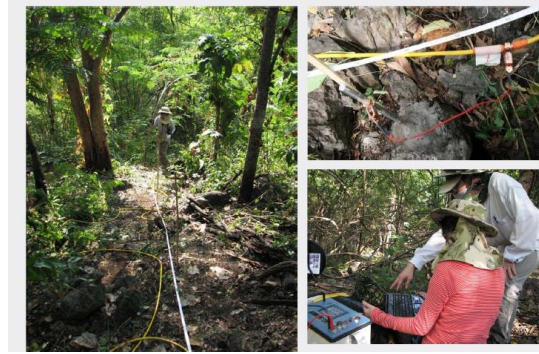
การสำรวจทางธรณีฟิสิกส์ ที่ให้ข้อมูลออกมาเป็นสภาพต้านทานไฟฟ้า (resistivity) มีหลากหลายวิธี โดยวิธีหลักๆ ที่จะกล่าวถึงในโครงการนี้ มีสองวิธี ด้วยกัน คือ Direct Current Resistivity (DCR) technique หรือเทคนิคการวัดสภาพต้านทานไฟฟ้าด้วยไฟฟ้ากระแสตรง และเทคนิค magnetotelluric (แมกนีโตเทลลูริกซ์) ซึ่งเป็นเทคนิคที่วัดคลื่นแม่เหล็กไฟฟ้าที่พื้นผิวโลก ค่าสภาพต้านทานไฟฟ้าที่ได้มานั้น มีประโยชน์มากมาย เพราะสามารถนำไปใช้เชื่อมโยงกับธรณีวิทยาเพื่อบ่งบอกถึง แร่ธรรมชาติ (e.g. Legault et al., 2007; Goldie, 2007; Turcer et al., 2006; Constable and Weiss, 2006; Vozoff, 1972; Orange, 1989) ใช้ศึกษาเทคโนโลยีระดับมหภาค (e.g. Boonchaisuk et al., 2017; Boonchaisuk et al., 2013; Shemang and molwalefhe, 2009; Holz et al., 2007; Unsworth et al., 2000; Chen et al., 1996; Jone, 1992) สำรวจแหล่งพลังงานความร้อนใต้พิภพ (e.g., Amatyakul et al., 2016; Amatyakul et al., 2015; Newman et al., 2008; Heise et al., 2008; Harinayana et al., 2006) ใช้ศึกษาปัญหาสิ่งแวดล้อม และวิศวกรรม (e.g., Satitpittakul et al., 2013; Chen et al., 2006; Lenkey et al., 2005; Pedersen et al., 2005; Benson et al., 1997).

DC Resistivity (DCR) survey เป็นเทคนิคการสำรวจชนิดหนึ่งทางธรณีฟิสิกส์ที่นิยมใช้กันอย่างแพร่หลาย ไม่ว่าจะเป็นการค้นหาน้ำมันบาดาล หาดแร่ต่างๆ ศึกษาความร้อน ศึกษาโพรงอากาศใต้ดิน ตรวจสอบโครงสร้างพื้นดินเพื่องานวิศวกรรมก่อสร้าง (e.g., Satitpittakul et al., 2013; Wilson et al., 2006; Buselli and Lu, 2001; Monteiro Santos and Sultan, 2008; Meju et al., 1999) เป็นต้น แต่โดยส่วนใหญ่แล้ว จุดประสงค์ของการนำไปใช้ คือ ใช้ในการสำรวจระดับตื้นๆ เท่านั้น กระบวนการ DCR เริ่มต้นโดยการยิงกระแสไฟฟ้าลงดินผ่านสองขั้วไฟฟ้า (electrode) และหลังจากนั้นก็ทำการวัดความต่างศักย์ระหว่างสองขั้วไฟฟ้าที่ตำแหน่งต่างกัน (รูปที่ 1 ก) อัตราส่วนระหว่างความต่างศักย์และกระแสไฟฟ้ารวมทั้งค่า geometry factor ระหว่างขั้วไฟฟ้าต่างๆ สามารถนำมาใช้เป็นตัวบ่งบอกถึงสภาพความต้านทานไฟฟ้า (resistivity) ได้

ข้อดีของการสำรวจด้วยเทคนิคนี้ คือ ได้สัญญาณที่ดี การสำรวจทำได้อย่างรวดเร็ว ค่าใช้จ่ายไม่สูงมากนัก ไม่ต้องทำการขุดดินเยาะเพื่อฝังเครื่องมือ ได้ข้อมูลที่มีความละเอียดแนวนอนสูง (เพราะสามารถวางขั้วไฟฟ้าได้ใกล้ๆ กัน) แต่ในแนวตามความลึกมีข้อจำกัดมาก ส่วนข้อเสีย ส่วนใหญ่จะอยู่ที่ได้ข้อมูลในแนวลึกไม่มากนัก ถ้าต้องให้ได้ข้อมูลที่ลึกมากขึ้น อาจต้องเสียค่าใช้จ่ายที่สูงมาก และยังได้ข้อมูลที่ไม่ดีอีกด้วย ด้วยเหตุผลนี้ การสำรวจด้วยเทคนิค DCR จึงมักจำกัดอยู่ที่การสำรวจในระดับตื้นๆ เท่านั้น ภาพแสดงการปฏิบัติงานเก็บข้อมูล DCR จริงแสดงในรูป 1ข)



(ก)



(ข)

รูปที่ 1: (ก) ภาพ diagram แสดงการเก็บข้อมูล DCR โดยมีขั้วไฟฟ้า A และ B ใช้จ่ายกระแสไฟฟ้า และขั้วไฟฟ้า M และ N ใช้วัดความต่างศักย์ (ข) ภาพแสดงการปฏิบัติงานจริงในพื้นที่ที่มีความลาดชันสูง

เทคนิคแมกนีโตเทลลูริกซ์ (magnetotelluric หรือ MT) เป็นอีกวิธีการสำรวจหนึ่งในทางธรณีฟิสิกส์ เพื่อตรวจสอบว่าใต้พื้นโลกมีโครงสร้างสภาพต้านทานไฟฟ้า (resistivity) เป็นอย่างไร ประโยชน์ของการนำไปใช้ มีหลากหลาย เช่นสำรวจหาแร่ยูเรเนียม (Tuncer et al., 2006) วิเคราะห์การเคลื่อนไหวของแมกมาใต้พื้นโลกก่อนเกิดภูเขาไฟ (Heise et al., 2008) วิเคราะห์กลไกของการเกิดแผ่นดินไหว (Unsworth et al., 2000; Boonchaisuk et al., 2017) วิเคราะห์สิ่งแวดล้อมและผลกระทบที่เกิดได้ดิน (Pedersen et al., 2005) รวมทั้งสำรวจแหล่งพลังงานความร้อนใต้พิภพ (Amatyakul et al., 2016; Amatyakul et al., 2015) และอื่นๆ อีกมากมาย วิธีการสำรวจแมกนีโตเทลลูริกซ์ในหนึ่งสถานีวัดประกอบไปด้วย เครื่องวัดสนามแม่เหล็ก (ดังรูปที่ 2ก) ในสามแกน (แกน x, y และ z ใช้สัญลักษณ์ว่า H_x , H_y และ H_z ในรูป 2ค) ตัววัด สนามไฟฟ้า (ดังรูปที่ 2ข ใช้สัญลักษณ์ว่า E_x และ E_y ในรูป 2ค) ในแกน x และ y ทั้งหมดเชื่อมต่อกันผ่านกล่องรับสัญญาณ (recording) ดังแสดงในรูปที่ 2ค โดยอัตราส่วนระหว่างสนามไฟฟ้ากับสนามแม่เหล็ก สามารถนำมาใช้บ่งบอกถึงสภาพต้านทานไฟฟ้าใต้ดินได้ โดยอัตราส่วนนี้จะบ่งบอกถึงค่าของความถี่ (หรือคาบ) ข้อมูลในคาบที่ต่ำหรือความถี่สูง จะบ่งบอกถึงสภาพพื้นดินที่ระดับตื้น ส่วนข้อมูลในคาบสูงหรือความถี่ต่ำ จะบ่งบอกถึงสภาพพื้นดินที่ระดับลึก ในการสำรวจ MT ถ้าทำเพียงจุดเดียวจะได้ภาพสภาพต้านทานไฟฟ้าแบบ 1 มิติ (ตามความลึก) ถ้าทำเรียงกันเป็นแถวยาว หรือที่เรียกว่า โปรไฟล์ ก็จะได้ภาพสภาพต้านทานไฟฟ้าแบบ 2 มิติ (ความยาวและความลึก) ถ้าทำกระจายครอบคลุมพื้นที่กว้าง ก็จะได้ภาพสภาพต้านทานไฟฟ้าแบบ 3 มิติ ซึ่งในขณะนี้เป็นที่นิยมกันมา

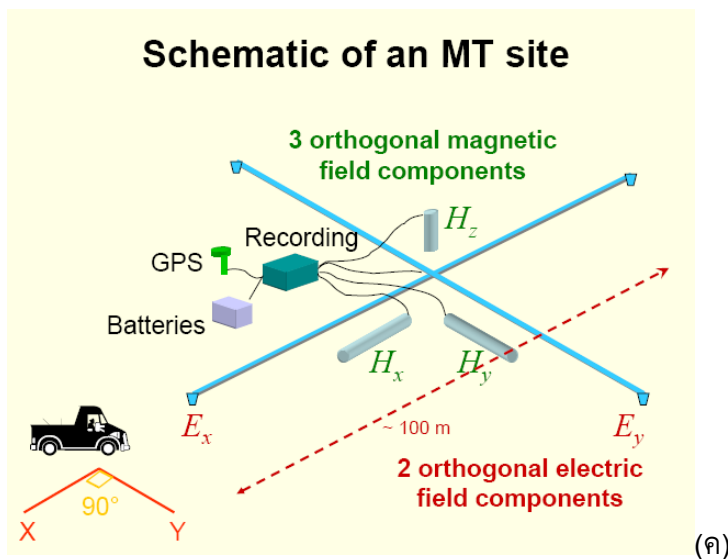
ข้อเสียของการสำรวจด้วยเทคนิค MT มีอยู่มากมาย คือ สัญญาณที่ได้อาจไม่ดี เพราะเป็นสัญญาณธรรมชาติ ถ้าอยากได้สัญญาณดี ต้องวางเครื่องมือทิ้งไว้นาน ทำให้การเก็บข้อมูลใช้เวลานาน เสียค่าใช้จ่ายมาก การฝังเครื่องมือ ต้องทำการขุดลึกพอสมควร ข้อมูลที่ได้มีความละเอียดในแนวนอนต่ำ เพราะไม่สามารถวางเครื่องมือใกล้ชิดกันมากได้ แต่ในขณะเดียวกัน ข้อดีเด่นเลย คือ สามารถทำการสำรวจลงได้ลึก เพราะข้อมูลขึ้นกับความถี่ (หรือคาบ) จึงเหมาะกับการสำรวจระดับปานกลางถึงลึก



(ก)



(ข)



(ค)

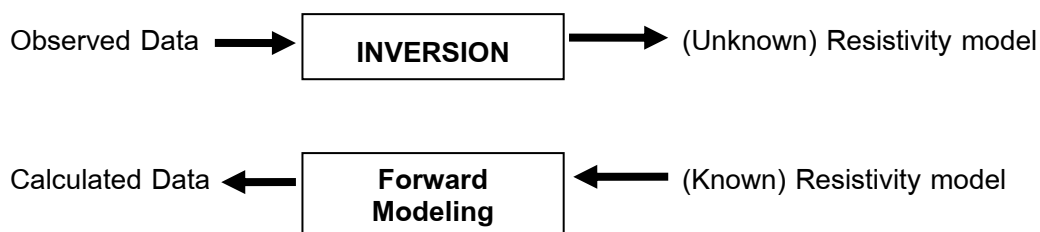
รูปที่ 2 (ก) เครื่องมือวัดสนามแม่เหล็ก (ข) หัววัดสนามไฟฟ้า (ค) รูปแบบการสำรวจ Magnetotelluric สำหรับ 1 สถานีวัด

จากทั้งสองเทคนิคจะเห็นได้ว่า ทั้ง DCR และ MT มีข้อดีคนละอย่าง เมื่อนำเอาข้อมูลทั้งสองเทคนิคมารวมกัน จะทำให้ช่วยกันหักล้างข้อเสียของแต่ละเทคนิคได้ เช่น ในเมื่อ DCR ไม่สามารถให้ข้อมูลระดับลึกได้ ข้อมูล MT จึงช่วยเสริมให้ข้อมูลระดับลึกได้ ในขณะเดียวกัน ข้อมูล MT มักไม่ได้รายละเอียดในแนวนอนมาก การมีข้อมูล DCR ก็จะช่วยเสริมในส่วนนี้ เป็นต้น นั่นจึงเป็นที่มาของโครงการวิจัยนี้ คือ การพัฒนาโปรแกรมร่วมแปลความข้อมูล DCR และ MT

หลังจากการออกภาคสนามเก็บข้อมูลของทั้งสองเทคนิคแล้ว ข้อมูลที่ได้จะเป็นข้อมูลดิบอยู่ ซึ่งต้องนำข้อมูลดิบนี้มาทำการประมวลผลหรือ data processing เสียก่อนเพื่อให้ข้อมูลที่สะอาดมากขึ้นคือปราศจากสัญญาณรบกวน และได้ข้อมูลที่มีความหมายมากกว่าข้อมูลดิบ หลังการประมวลผล เทคนิค

DCR จะให้ข้อมูลที่เรียกว่า apparent resistivity ที่เป็นฟังก์ชันของความห่างของขั้วไฟฟ้า (electrode spacing) ส่วนเทคนิค MT จะให้ apparent resistivity & phase (แต่ apparent resistivity มีนิยามคนละอย่างกัน) ที่เป็นฟังก์ชันของความถี่หรือคาบ เนื่องจากข้อมูลเหล่านี้ ไม่ได้ให้ข้อมูลที่ เป็นฟังก์ชันของความลึก ทำให้การแปลความหมายเป็นไปได้ยาก ความผิดพลาดอาจสูงได้ ดังนั้นก่อนจะถูกนำไปแปลความหมาย ข้อมูลทั้งหมดนี้จะถูกนำไปผ่านกระบวนการ inversion ซึ่งเป็นกระบวนการทางคณิตศาสตร์ขั้นสูง เพื่อแปลข้อมูลเหล่านี้ให้เป็นโครงสร้างสภาพความต้านทานไฟฟ้าที่เป็นฟังก์ชันของความลึก หรือเรียกง่าย ๆ ว่าแบบจำลองสภาพความต้านทานไฟฟ้า (resistivity model) ซึ่งง่ายต่อการเข้าใจและสามารถใช้บ่งบอกตำแหน่งของสิ่งผิดปกติได้อย่างชัดเจน

กระบวนการ inversion ต้องพึ่งพาอาศัยอีกกระบวนการหนึ่งที่สำคัญมาก โดยกระบวนการนี้จะทำการแก้สมการทางฟิสิกส์ (กฎของโอห์ม) ของเทคนิค DCR เพื่อจำลองค่า apparent resistivity จากแบบจำลองที่สร้างขึ้น และแก้สมการทางฟิสิกส์ (กฎของแมกซ์เวลล์) ของเทคนิค MT เพื่อจำลองค่า apparent resistivity and phase จากแบบจำลองที่สร้างขึ้น กระบวนการนี้เรียกว่า forward modeling ทั้งสองกระบวนการ (forward modeling and inversion) สรุปเป็นรูปคร่าว ๆ ได้ดังรูปที่ 3 จะเห็นได้ว่าทั้งสองกระบวนการที่ทำงานตรงกันข้ามอย่างชัดเจน



รูปที่ 3: แผนภาพเปรียบเทียบกระบวนการ inversion และกระบวนการ forward modeling

สำหรับข้อมูล DCR โปรแกรมที่ใช้ในการทำ inversion ได้ถูกพัฒนาขึ้นมามาก่อนหน้านี้แล้วโดยผู้วิจัยและทีมงาน ตั้งแต่ปี ค.ศ. 2008 (Boonchaisuk et al., 2008) และถูกพัฒนาเรื่อยมาหลายเวอร์ชันเพื่อให้ได้การทำงานที่ดีขึ้น (Vachiratienchai et al., 2010; Vachiratienchai and Siripunvaraporn, 2013) เช่นเดียวกัน สำหรับข้อมูล MT โปรแกรมที่ใช้ในการทำ inversion ก็ได้ถูกพัฒนาขึ้นมามาก่อนหน้านี้แล้วโดยผู้วิจัยและทีมงาน ตั้งแต่ปี ค.ศ. 2000 (Siripunvaraporn and Egbert, 2000) และได้ถูกพัฒนาขึ้นมากต่อเนื่องมาหลายเวอร์ชัน (Siripunvaraporn et al., 2004; Siripunvaraporn et al., 2005; Siripunvaraporn and Egbert, 2007; Siripunvaraporn and Egbert, 2009; Rung-Arunwan and Siripunvaraporn, 2010; Siripunvaraporn and Sarakorn, 2011; Siripunvaraporn, 2012) โปรแกรม inversion ที่พัฒนาขึ้นมากสำหรับทำงานกับข้อมูล DCR และข้อมูล MT อยู่บน หลักการทางคณิตศาสตร์

เดียวกัน ที่เรียกว่า data space Occam's inversion method ซึ่งเป็นเทคนิคที่ให้ผลดี มีเสถียรภาพสูง โดยเป้าหมายของเทคนิค คือ การคำนวณหาแบบจำลองที่เป็นแบบ minimum structure เพื่อให้แบบจำลองที่ได้มีความ smooth มากกว่าเทคนิคอื่นๆ

2. วัตถุประสงค์ของโครงการวิจัย และ outline ของรายวิจัย

ดังนั้นในงานวิจัยนี้ เป็นการพัฒนาโปรแกรมแปลความหมายข้อมูลทั้งสองข้อมูล (DCR & MT) พร้อมๆ กัน โดยผ่านกระบวนการ inversion โดยใช้เทคนิค data space Occam's inversion method เหมือนที่เคยทำมาก่อน จุดประสงค์ก็เพื่อสร้างโปรแกรมแปลความหมายร่วมนี้ ให้มีประสิทธิภาพ คือ รวดเร็ว ใช้หน่วยความจำไม่มาก และช่วยเพิ่มศักยภาพของข้อมูลแต่ละชนิดอีกด้วยเมื่อนำมาใช้แปลความหมายร่วม และที่สำคัญกระตุ้นให้ประชาคมธรณีฟิสิกส์ได้สนใจกับการแปลความร่วมของข้อมูลสองชนิดนี้ ซึ่งเมื่อก่อนก็มีการใช้งานกัน แต่ทว่าไม่ประสบความสำเร็จมากนักเพราะว่าตัวโปรแกรมก่อนหน้านี้ที่พัฒนาโดยนักวิจัยอื่นๆ มีข้อจำกัดเยอะ ทีมงานวิจัยนี้จึงหวังว่า โปรแกรมที่พัฒนาขึ้นมาจะช่วยแก้ไขข้อบกพร่องเหล่านั้น และดึงดูดให้นักวิจัยมาสนใจการแปลความหมายร่วมมากขึ้น

ในรายงานฉบับนี้ เราจะไม่อธิบายถึงเทคนิค data space Occam's inversion ในรายละเอียด เพราะสามารถหาอ่านได้ใน publications ก่อนหน้านี้ แต่จะเน้นถึงการพัฒนาโปรแกรมแปลความร่วมในส่วนที่เกี่ยวข้องเท่านั้น หลังจากนั้นจะเป็นการทดสอบโปรแกรมกับข้อมูลเทียม และสุดท้ายกับข้อมูลจริง

นอกจากนี้ ในโครงการวิจัยนี้ ยังได้นำเอาตัวโปรแกรมนี้ไปใช้งานจริง เพื่อช่วยในการสำรวจแหล่งพลังงานความร้อนใต้พิภพที่ แม่จัน จังหวัดเชียงราย และที่ น้ำพุร้อนฝาง จังหวัดเชียงใหม่ รวมทั้งใช้ในการศึกษาการเคลื่อนตัวของรอยเลื่อนแม่ลาว ที่ทำให้เกิดแผ่นดินไหวครั้งใหญ่ที่สุดในประเทศอีกด้วย โดยในส่วนของการทำงานในสามเรื่องหลัง จะกล่าวถึงแบบย่อๆ เท่านั้น ผู้สนใจสามารถติดตามอ่านได้จากใน publications ตัวจริง

3. การพัฒนาโปรแกรมแปลความหมายร่วมของข้อมูล DCR และ MT

เทคนิค data space Occam's inversion (Siripunvaraporn and Egbert, 2000; Siripunvaraporn et al., 2005; Siripunvaraporn, 2012) เริ่มต้นด้วยการ perturb แบบจำลอง \mathbf{m} พร้อม update แบบจำลองสำหรับ iteration $k+1$ (i.e. \mathbf{m}_{k+1}) ตามสมการที่ (1)

$$\mathbf{m}_{k+1} - \mathbf{m}_0 = \mathbf{C}_m \mathbf{J}_k^T \mathbf{C}_d^{-1/2} [\lambda \mathbf{I} + \mathbf{C}_d^{-1/2} \mathbf{J}_k \mathbf{C}_m \mathbf{J}_k^T \mathbf{C}_d^{-1/2}]^{-1} \mathbf{C}_d^{-1/2} \mathbf{d}_k. \quad (1)$$

แบบจำลองที่ update ตามสมการที่ (1) นี้ถูก guide โดยตัว data misfit $\mathbf{d}_k = \mathbf{d} - \mathbf{F}[\mathbf{m}_k] + \mathbf{J}_k(\mathbf{m}_k - \mathbf{m}_0)$ และที่ sensitivity matrix $\mathbf{J}_k = \partial \mathbf{F} / \partial \mathbf{m}_k$, โดย \mathbf{d} คือเวกเตอร์ข้อมูลจริง $\mathbf{F}[\mathbf{m}]$ คือ

response ที่คำนวณได้ (หรือข้อมูลคำนวณ) \mathbf{C}_d เป็น data covariance matrix, \mathbf{m}_0 เป็น prior model, \mathbf{C}_m เป็น model covariance matrix, \mathbf{I} เป็น identity matrix, λ^{-1} เป็น La Grange multiplier โดย inversion จะทำการ update แบบจำลองไปหลายๆ iteration ตามสมการที่ (1) จนกระทั่ง RMS misfit ที่นิยามว่า $([(\mathbf{d} - \mathbf{F}[\mathbf{m}])^T \mathbf{C}_d^{-1/2} (\mathbf{d} - \mathbf{F}[\mathbf{m}])]/N)^{1/2}$ กับ target misfit ตรงหรือใกล้เคียงกันก็จะหยุดทำงาน ซึ่งโดยปกติตั้ง target misfit ไว้ที่ 1 RMS (N คือจำนวนข้อมูลทั้งหมด)

สำหรับเวกเตอร์ข้อมูลจริง \mathbf{d} สำหรับ MT คือ apparent resistivity (ρ_a^{MT}) และ phase (ϕ^{MT}) ส่วนของข้อมูล DCR คือ apparent resistivity (ρ_a^{DCR}) ในการพัฒนาโปรแกรมร่วมแปลความหมาย (joint interpretation program) สิ่งแรกที่ต้องแก้ไข คือ ตัวเวกเตอร์ข้อมูลจริง ซึ่งในที่นี้ เวกเตอร์ข้อมูลจริงจะกลายเป็น $\mathbf{d}_{Joint}^T = [\mathbf{d}^{MT} \ \mathbf{d}^{DCR}]^T$, where $\mathbf{d}^{MT} = [\rho_a^{MT} \ \phi^{MT}]$ and $\mathbf{d}^{DCR} = [\rho_a^{DCR}]$, ตอนนี้จำนวนข้อมูลรวมก็จะเป็นจำนวนข้อมูลของทั้งสองชนิดข้อมูลรวมกัน $N = N^{MT} + N^{DCR}$ เช่นเดียวกับเวกเตอร์ข้อมูลจริง เวกเตอร์ตัวอื่นๆ ก็ต้องปรับให้รวมทั้งสองข้อมูลเข้าไว้ด้วยกัน ตามหลักการเดียวกัน เช่น $\mathbf{F}[\mathbf{m}]^T = [\mathbf{F}[\mathbf{m}]_{MT} \ \mathbf{F}[\mathbf{m}]_{DCR}]^T$, and $\mathbf{J}^T = [\mathbf{J}_{MT}; \mathbf{J}_{DCR}]^T$.

สิ่งที่ทั้งสองข้อมูล DCR และ MT มีเหมือนกัน คือ ให้แบบจำลองสภาพต้านทานไฟฟ้า \mathbf{m} อันเดียวกันถ้าทำการทดลองในพื้นที่เดียวกัน ดังนั้นในส่วนของแบบจำลองไม่ต้องแก้ไขใดๆ แต่ส่วนที่ต้องแก้ไขเพื่อให้เหมาะสมกับข้อมูลทั้งสองชนิด คือ grid discretization เนื่องจากข้อมูล MT มัก sense โครงสร้างในระดับลึก ส่วนข้อมูล DCR จะ sense โครงสร้างในระดับตื้น ยึดถือแบบอย่าง grid discretization ที่ได้จาก MT อย่างเดียว หรือจาก DCR อย่างเดียว จะทำให้แบบจำลองนี้ ให้ค่าข้อมูลคำนวณที่ไม่ถูกต้อง ดังนั้นจึงต้องออกแบบใหม่ให้มีค่าที่เหมาะสม จากการทดลองหลากหลายรูปแบบ ผู้วิจัยพบว่ารูปแบบที่เหมาะสมสำหรับ grid discretization ที่จะใช้กับทั้งสองข้อมูล คือการผสมกันจาก grids ทั้งสองชนิดในอัตราที่เหมาะสม ดังนี้ ใกล้เคียง กับ พื้นผิว grid discretization สำหรับ DCR นั้นเหมาะสมแล้ว นั่นคือ horizontal grid discretization นั้นยังยึดให้มีสอง vertical grids ระหว่างสองอิเล็กโทรด ส่วน vertical grid discretization นั้น ผสมของ MT เข้าไป คือ grid ในแนวตั้งเมื่อลึกขึ้นจะขยายใหญ่ขึ้นเรื่อยๆ ด้วยอัตรา 1.2 – 1.5 เท่าของความหนาของ grid ก่อนหน้านั้น การขยาย grid ด้วยอัตราเท่านี้ทำให้ได้ความถูกต้อง กับทั้งสองข้อมูล และยังทำให้ลงไปได้ลึกตามที่สัญญาณ MT สามารถลงไปได้อีกด้วย การออกแบบ grid ในลักษณะนี้จะทำให้จำนวน grid เพิ่มขึ้น มากกว่า grid เฉพาะของ MT อย่างเดียว หรือ grid เฉพาะของ DCR อย่างเดียว เมื่อ grid เพิ่ม ข้อเสียที่ตามมาคือ computational time ก็จะมากขึ้นด้วย ซึ่งในข้อนี้ทางคณะผู้วิจัยก็ได้ตระหนักแล้ว แต่เนื่องจากเทคนิคการทำ inversion ของคณะผู้วิจัยนั้น เวลาในการคำนวณขึ้นหลักๆ อยู่กับจำนวนข้อมูล ซึ่งเพิ่มขึ้นเช่นกัน แต่เมื่อเทียบกับจำนวนกริดที่เพิ่มขึ้นแล้ว เวลาในการคำนวณที่เพิ่มขึ้นเนื่องจากจำนวนข้อมูลที่เพิ่มขึ้นก็ยังน้อยกว่า

อีกส่วนหนึ่งที่ต้องแก้ไข และถือว่าเป็นส่วนสำคัญของงานวิจัยนี้ คือ การปรับ length scale ที่ใช้ใน model covariance \mathbf{C}_m ให้เหมาะสมที่สุด \mathbf{C}_m มีหน้าที่ควบคุมความ smooth ของแบบจำลองเทียบกับแบบจำลองอ้างอิง ซึ่งถ้าเราใช้ \mathbf{C}_m ของ MT โดยตรง ความ smooth ที่บริเวณใกล้พื้นผิวจะเสีย

ไป แต่ถ้าเราใช้ C_m ของ DCR ความ smooth ในบริเวณลึกจะหายไป ดังนั้นการปรับและทดลองเพื่อให้ได้ค่าที่เหมาะสมจึงเป็นสิ่งสำคัญที่สุด ในการออกแบบ C_m ที่ผ่านมาใช้การแก้ปัญหาค่า $diffusion$ equation เป็นหลัก โดย parameter ที่ควบคุมความ smooth จะฝังอยู่ในสมการ $diffusion$ ที่มีชื่อเรียกว่า $diffusion$ length scale โดยปกติใน MT ค่า $diffusion$ length scale จะมีค่า fix ที่มีขนาดใหญ่ตาม $grid$ discretization ของ MT ส่วนในของ DCR ค่า $diffusion$ length scale จะมีค่า fix เช่นกันแต่มีขนาดเล็กกว่าตาม $grid$ discretization ของมัน ดังนั้นในงานวิจัยนี้ เพื่อให้ $diffusion$ length scale เหมาะสมกับข้อมูลทั้งสองชนิด ดังนั้นการใช้ fix length scale จึงเป็นไปได้ หลังจากการทดลองกับหลากหลายค่าพบว่าการใช้ $varying$ length scale นั้นเหมาะสมที่สุด โดยค่า length scale สำหรับใกล้พื้นผิว จะเป็นค่าน้อยตามที่ข้อมูล DCR ต้องการ ส่วนในที่ลึกก็จะเป็นตามที่ข้อมูล MT ต้องการ แต่สำหรับช่วงรอยต่อจากตื้น ไปลึก ก็จะมี $vary$ โดยเพิ่มขึ้นตามสัดส่วนที่เหมาะสมของการสำรวจ การทำให้ค่า length scale นี้สามารถปรับตัวเองได้อย่างอัตโนมัติ ช่วยให้สามารถ deal กับ $resolving$ power ของแต่ละชนิดข้อมูลได้เป็นอย่างดี

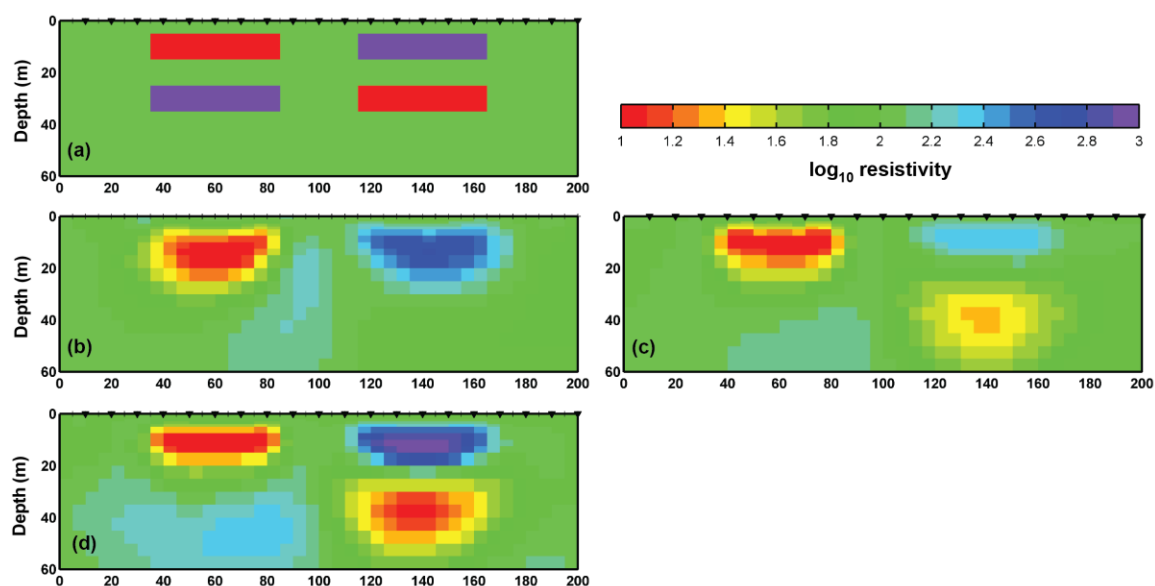
4. การทดสอบโปรแกรมแปลความหมายร่วมกับข้อมูลเทียม

เพื่อทดสอบว่าโปรแกรมแปลความหมายที่พัฒนาขึ้นมานั้นใช้ได้ถูกต้องและมีประสิทธิภาพ การทดลองแรกที่จะนำเสนอคือการทดสอบกับแบบจำลองเทียมที่สร้างขึ้นมา โดยแบบจำลองนี้แสดงให้เห็นในรูปที่ 4a) ประกอบไปด้วย โครงสร้าง resistive bodies & conductive bodies สลับกันไปมาภายใน homogeneous earth โดย anomalies เหล่านี้อยู่ที่ความลึกตั้งแต่ 10 m ถึง 50 m ซึ่งก็เป็นความลึกที่เหมาะสมสำหรับการสำรวจด้วยเทคนิค DCR และก็ด้วยเทคนิค MT แต่เฉพาะช่วง high frequencies เท่านั้น ข้อมูลเทียม DCR และ MT ก็สร้างขึ้นมาจากแบบจำลองเทียม 4a) นี้ ผ่านกระบวนการ forward modeling หลังจากนั้นเพื่อให้มีความสมจริงก็เพิ่ม noise เข้าไปในข้อมูล 2% แล้วก็นำข้อมูลเทียมทั้งสองชนิดนี้ไปทำ inversion เพื่อให้ได้ inverted model ออกมา โดยผลที่ได้แสดงในรูป 4b) – 4d)

รูปที่ 4b) เป็น inverted model ที่ได้จากการทำ inversion ของข้อมูล DCR ประเภท Schlumberger เพียงอย่างเดียว ซึ่งผลที่ได้แสดงให้เห็นว่า เราสามารถ recover resistive & conductive anomalies บริเวณตื้นๆ ได้เท่านั้น ข้อมูล DCR เพียงอย่างเดียวไม่เพียงพอต่อการ recover โครงสร้างระดับลึกเลย รูปที่ 4c) เป็น inverted model ที่ได้จากการทำ inversion ของข้อมูล MT เพียงอย่างเดียว ซึ่งผลที่ได้แสดงให้เห็นว่า ข้อมูล MT มีศักยภาพในการ recover anomalies ได้ทั้งระดับตื้นและลึก แต่ทว่า การ sense ถึง resistive bodies ของ MT นั้นต่ำ จึง recover ได้เฉพาะ conductive bodies ทั้งสองความลึก รูปที่ 4d) เป็น inverted model ที่ได้จากการทำ joint inversion หรือแปลความหมายร่วมของข้อมูล DCR กับข้อมูล MT โดยภาพที่ได้แสดงให้เห็นว่าเมื่อใช้ทั้งสองข้อมูลร่วมกันแล้ว inverted model ที่ได้มีความชัดเจนมากขึ้น กล่าวคือ สามารถ recover ส่วนตื้นๆ ได้เป็นอย่างดี ตามที่ข้อมูล DCR สามารถทำได้ และนอกจากนี้ยังสามารถ recover ส่วนลึกๆ เพิ่มขึ้นได้ ตามที่ข้อมูล MT สามารถทำได้อีกด้วย การทดลองนี้แสดงให้เห็นว่า การใช้ข้อมูลร่วมกันช่วยส่งเสริมซึ่งกันและกันได้เป็นอย่างดี

และโปรแกรมที่พัฒนาขึ้นมาก็มีศักยภาพมากด้วย แต่อย่างไรก็ตาม เนื่องจาก MT ไม่สามารถ recover resistive body ที่ลึกได้อยู่แล้ว การ recover จาก joint inversion จึงยังคงเป็น defect ต่อไป

ถ้าในการทดลองนี้ เราจำเป็นต้องอยากให้ DCR สามารถ recover ข้อมูลได้ทั้งระดับตื้นและระดับลึกด้วย ไม่ใช่เฉพาะระดับตื้นเหมือนในรูป 4b) เราจำเป็นต้องวางแนวสำรวจให้ยาวกว่านี้อีก 3-4 เท่า ณ ขณะนี้ความยาวของแนวสำรวจอยู่ที่ 200 เมตร ถ้าต้องการให้ recover deeper anomalies ต้องวางให้ยาวประมาณ 600 – 1000 เมตร ซึ่งถ้าเป็นการสำรวจจริง จะต้องใช้งบประมาณสำรวจและเวลาเพิ่มขึ้นอีกมาก ซึ่งอาจไม่คุ้มค่า ผลที่ได้จากการทดลอง (รูปที่ 4d) นี้บ่งบอกว่า แทนที่จะเพิ่มแนวสำรวจ DCR ให้ยาวขึ้น ให้ทำการสำรวจ MT แทนโดยสถานีของ MT ที่เพิ่มขึ้นอาจมีน้อยกว่าที่ใช้ในการทดลองนี้ก็ได้ ก็สามารถทำให้ recover deeper anomalies ได้เช่นกัน และการเพิ่มสถานี MT เข้าไป ถ้าไม่มากเกินไป ก็จะใช้เวลาในการสำรวจและงบประมาณน้อยกว่าการเพิ่มความยาวของแนวสำรวจ DCR

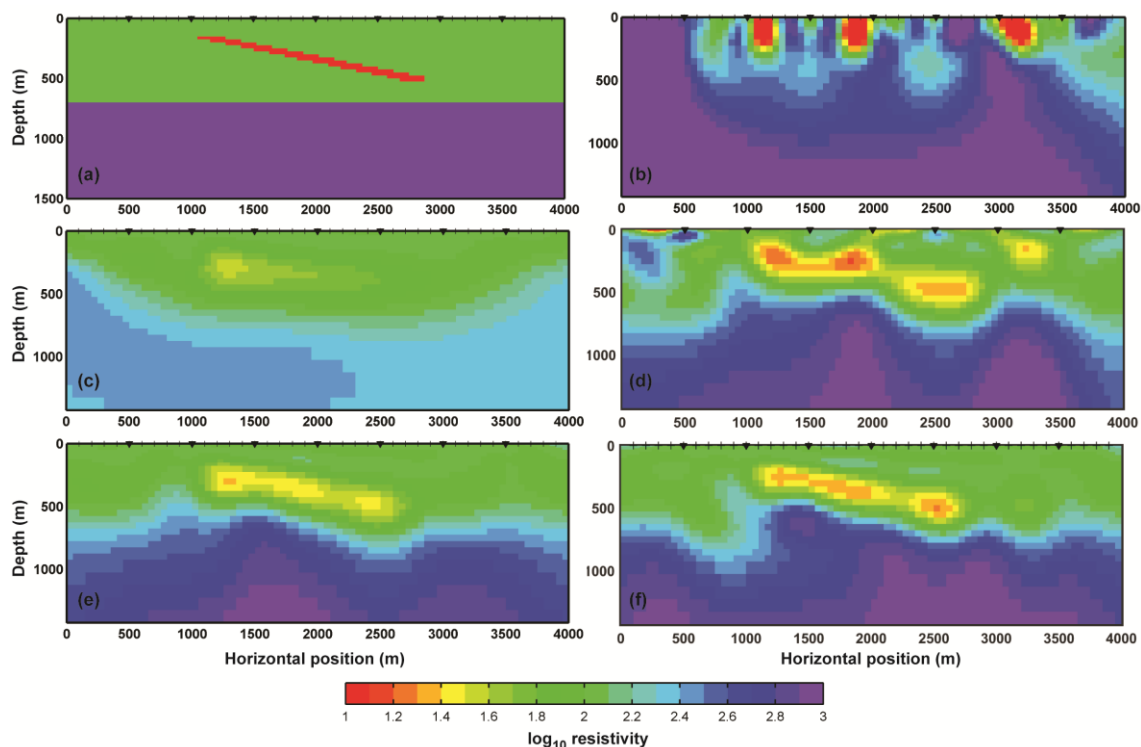


รูปที่ 4. (a) แบบจำลองเทียมที่สร้างขึ้นมา ประกอบด้วย resistive body (1000 ohm-m; สีม่วง) และ conductive bodies (10 ohm-m; สีแดง) อยู่ใน homogeneous earth ที่มีค่า resistivity 100 ohm-m (b) inverted model ที่ได้จากการทำ inversion ของข้อมูล DCR อย่างเดียว (c) inverted model ที่ได้จากการทำ inversion ของข้อมูล MT อย่างเดียว (d) inverted model ที่ได้จากการทำ inversion ร่วมของข้อมูล DCR และ MT

ในทางกลับกัน ถ้าต้องการให้ข้อมูล MT สามารถ recover shallow structures ได้ดีกว่าที่แสดงในรูป 4c) ก็สามารถทำได้ โดยเพิ่มจำนวนสถานี MT ให้ถี่ขึ้นเหมือนกับที่ทำใน DCR แต่การทำแบบนี้เป็นการเพิ่มงบประมาณและเวลาในการสำรวจมากขึ้นไปอีกหลายเท่าตัว และการทำสถานี MT ให้ถี่ขึ้น

ในทางปฏิบัติเป็นไปได้ยากกว่า ดังนั้นรูปที่ 4d) ก็บ่งบอกให้เห็นอีกว่า แทนที่จะทำให้สถานะ MT ถี่ขึ้น ก็เปลี่ยนเป็นสำรวจด้วยเทคนิค DCR ดีกว่าให้ผลที่ดีกว่า แล้วก็ใช้งบประมาณและเวลาน้อยกว่าอีกด้วย

การทดลองต่อมา เป็นการทดลองเพื่อแสดงให้เห็นว่าการใช้ข้อมูล DCR สามารถนำมาช่วยแก้ปัญหา static shift ของ MT ได้ ซึ่งเป็นปัญหาหลักของ MT เมื่อใดก็ตามที่ข้อมูล MT ถูก distort จนเกิด static shift ถ้านำเอาข้อมูล MT ไปใช้งานโดยตรง โดยไม่แก้ไข จะทำให้เกิดปัญหาการแปลความผิดพลาด แบบจำลองเทียมแสดงในรูปที่ 5a) แบบจำลองนี้ประกอบไปด้วย สอง resistivity layers ชั้นบน 100 ohm-m และชั้นล่าง 1000 ohm-m ในชั้นบน มี anomaly วางเรียงตัวเอียงทำมุมประมาณ 11 องศา มีค่า resistivity อยู่ที่ 10 ohm-m ข้อมูลเทียมของ DCR และ MT ถูกสร้างขึ้นมาจากแบบจำลองในรูป 5a) นี้ แต่ในการทดลองนี้ ข้อมูล MT ถูกนำมา distort ด้วยค่า random เพื่อจำลองว่าข้อมูล MT นี้มี static shift ในขณะที่ ข้อมูล DCR ไม่ได้ถูก distort ใดๆ



รูปที่ 5. (a) แบบจำลองเทียม (b) inverted model จากการทำ inversion ของ MT data ที่ถูก distort ให้มี static shift (c) inverted model จากการทำ inversion ของข้อมูล DCR (d) inverted model จากการทำ inversion ของข้อมูล MT แต่เฉพาะส่วน phase (e) inverted model จากการทำ inversion ร่วมของข้อมูล MT (ที่มีการ distort) และ DCR (f) inverted model จากการทำ inversion ร่วมของข้อมูล MT (ที่มีการ distort แต่ถูกแก้ไขแล้ว) และ DCR

การทดลองแรกเป็นการนำเอาข้อมูล MT ที่ถูก distort ไปทำ inversion โดยตรง ผลที่ได้แสดงในรูปที่ 5b) ซึ่งจะเห็นได้ว่า ไม่มีความใกล้เคียงกับแบบจำลองเทียม รูปที่ 5a) เลย ซึ่งถ้าผู้วิจัยไม่เคยทราบต้นฉบับมาก่อนแล้วเชื่อในผลที่ได้ ก็อาจทำให้นำไปแปลความหมายผิดพลาด การทดลองต่อมาเป็นการทำ inversion กับข้อมูล DCR โดยตรง ผลที่ได้แสดงในรูป 5c) ซึ่งแสดงให้เห็นว่า แบบจำลองรูปที่ 5c) มีความใกล้เคียงกับแบบจำลอง 5a) ในบริเวณต้น แต่ในตามความลึกก็ยังเป็นปัญหาอยู่ ทำให้ไม่สามารถ recover thin conductive body ที่วางเอียงตัวทำมุม 11 องศาได้ โดยปกติข้อมูล MT มีสองส่วนคือ apparent resistivity และ phase เมื่อมี distortion ส่วนของข้อมูลที่ได้รับผลกระทบโดยตรงคือ apparent resistivity แต่ส่วนที่ไม่ได้รับผลกระทบเลย หรือน้อยมาก คือส่วนที่เป็น phase ดังนั้น วิธีหนึ่งที่นักวิจัยชอบทำกัน เพื่อเป็นการลดปัญหาจากการที่ MT มี distortion คือการทำ inversion เฉพาะส่วนที่เป็น phase เป็นอย่างเดียว ในการทดลองนี้ เราก็ทำแบบนี้เช่นกัน ผลของการทำ inversion เฉพาะ phase แสดงในรูปที่ 5d) ซึ่งก็ให้ผลที่ดีระดับหนึ่ง กล่าวคือ บ่งบอกได้ถึงสอง layers และยังมี thin conductive body ผังอยู่ในชั้นแรก แต่มุมการวางตัวก็ยังไม่ชัดเจน ทั้งนี้ความกำกวมอาจเนื่องมาจากจำนวนข้อมูลที่ใช้ลดลงไปครึ่งหนึ่ง

ในการทดลองต่อไป เรานำเอาข้อมูล MT (ทั้ง apparent resistivity & phase) มาทำ inversion ร่วมกับข้อมูล DCR ผลที่ได้แสดงให้เห็นในรูปที่ 5e) โปรแกรมสามารถ recover ได้ทั้ง 2 resistive layers (แต่ boundary อาจไม่ชัดเจน) รวมทั้ง thin conductive body ที่แสดงให้เห็นว่าวางตัวเอียงตัวทำมุมได้อย่างชัดเจน แสดงให้เห็นว่า เมื่อใช้ข้อมูลรวมกันมีการส่งเสริมกันอย่างเห็นได้ชัด จากที่ข้อมูล DCR อย่างเดียวไม่สามารถแสดง thin conductive layer ที่วางตัวเอียง รวมทั้งชั้น resistive ที่ลึกได้ เมื่อมีข้อมูล MT มาเสริม ก็สามารถช่วยแก้ไขในส่วนนี้ ในทางตรงกันข้าม ข้อมูล MT ที่ถูก distort เมื่อนำไปทำ inversion ได้ผลที่ไม่สามารถแปลความหมายได้ แต่เมื่อมีข้อมูล DCR มาช่วยแก้ไขค่า background resistivity ให้ ผลที่ได้จึงสมเหตุสมผล และยังได้ค่า static shift correction ที่เมื่อนำไป correct ข้อมูล MT แล้วยังช่วยให้ผลที่ได้จากการทำ inversion ได้ถูกต้องมากขึ้น ดังแสดงในรูปที่ 5f) ซึ่งเป็นการทำ inversion ของข้อมูลรวม DCR กับ MT ที่ถูกแก้ไขแล้ว

จากทั้งสองการทดลอง (และอีกหลายๆ การทดลองที่ไม่ได้แสดงในรายงานนี้) แสดงให้เห็นว่า โปรแกรมที่พัฒนาขึ้นมานั้น มีศักยภาพที่สูง สามารถนำไปใช้เพื่อ recover โครงสร้างต่างๆ ได้อย่างถูกต้องและแม่นยำมากขึ้น

รายละเอียดเพิ่มเติม ทั้งหลักการทำงาน การทดสอบกับข้อมูลเทียม และ ข้อมูลจริง (ของประเทศแคนาดา) สามารถอ่านได้ใน

- Puwis Amatyakul, Chatchai Vachiratienchai and **Weerachai Siripunvaraporn**, 2017, WSJointInv2D-MT-DCR: An efficient joint two-dimensional magnetotelluric and direct current resistivity inversion, Computers & Geosciences, 102, 100-108. (IF 2015 = 2.474)

5. การนำไปใช้กับข้อมูลสำรวจจริง

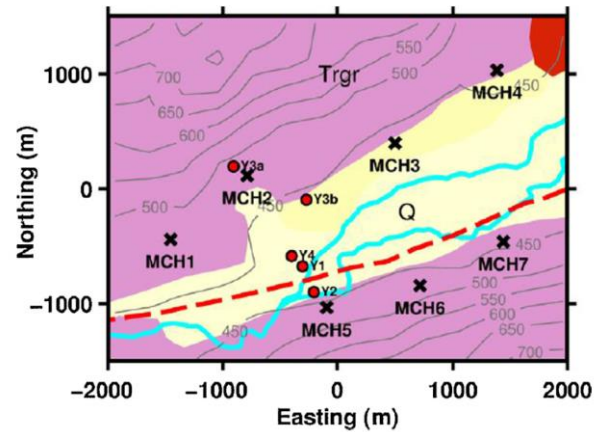
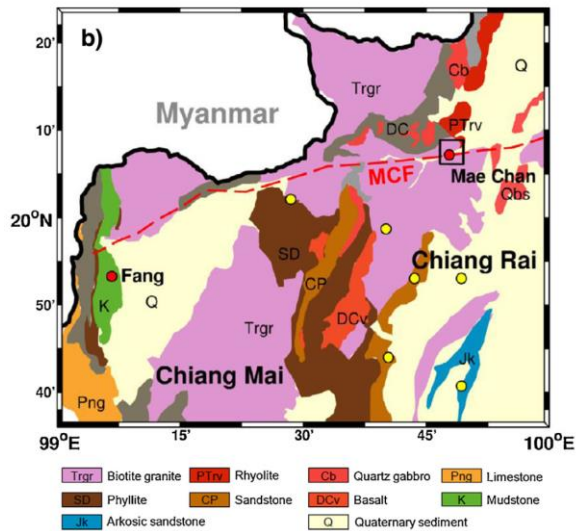
ในส่วนนี้ เป็นการนำโปรแกรมไปใช้งานกับงานสำรวจจริง โดยเฉพาะเพื่อแก้ไขข้อมูล MT ก่อนที่จะนำเอาข้อมูล MT ไปทำ inversion เพื่อสร้างภาพสภาพต้านทานไฟฟ้าแบบสามมิติออกมา ในรายงานฉบับนี้ ผู้วิจัยขอสงวนที่จะกล่าวถึงรายละเอียดของการสำรวจ และอื่นๆ รวมทั้งการแปลความหมายอย่างเดียว แต่จะนำเสนออย่างสรุป เพื่อให้สั้นและกระชับ โดยผู้ที่สนใจสามารถติดตามได้ในรายละเอียด ซึ่งจะอยู่ภาคผนวกของรายงานฉบับนี้

5.1. การสำรวจแหล่งพลังงานความร้อนใต้พิภพ น้ำพุร้อนป่าติ่ง แม่จัน จ.เชียงราย

แหล่งพลังงานความร้อนใต้พิภพมีความสำคัญต่อการพัฒนาประเทศชาติเป็นอย่างมาก ในหลายๆ ประเทศ ใช้พลังงานความร้อนใต้พิภพในการผลิตกระแสไฟฟ้า ซึ่งนั่นคือเป้าหมายของการสำรวจในอนาคต เพื่อประเมินศักยภาพของแหล่งน้ำพุร้อนป่าติ่ง แม่จัน จ.เชียงราย เพื่อการนำไปสู่การสร้างโรงไฟฟ้าพลังงานความร้อนใต้พิภพ เนื่องจากการสำรวจแมกนีโตเทลลูริกซ์เพื่อประเมินศักยภาพของแหล่งพลังงานความร้อนใต้พิภพในประเทศไทย ยังไม่เคยมีการทำมาก่อนเลย การสำรวจในครั้งนี้จึงเป็นเพียงการนำร่อง (pilot) ของการสำรวจ เพื่อนำไปสู่การสำรวจในครั้งต่อไป ในพื้นที่อื่นๆ ด้วย

พื้นที่ของการสำรวจอยู่ในพื้นที่น้ำพุร้อนป่าติ่ง จ.เชียงราย ดังแสดงให้เห็นในรูปที่ 6ก) รูป 6ข) แสดงตำแหน่งสถานีสำรวจ MT ซึ่งในกรณีนี้มีเพียง 7 สถานีติดตั้งรอบๆ บริเวณพื้นที่น้ำพุร้อน ซึ่งส่วนใหญ่ประกอบไปด้วยชั้นหินแกรนิต โดยมีชั้นหินตะกอนทับถมอยู่ด้านบน สถานีวัด MCH1 – MCH7 วางเรียงกระจายครอบคลุมพื้นที่ประมาณ 3 km x 4 km และล้อมรอบน้ำพุร้อนป่าติ่ง ข้อมูลที่ได้ถูกนำไปประมวลผล และแก้ไขค่า static shift ด้วยข้อมูล DCR ที่เก็บรวม และทำ 3-D inversion โดยโปรแกรมที่พัฒนาขึ้นมาก่อนหน้านี้ ผลการสำรวจแสดงให้เห็นในรูปที่ 7ก) และ 7ข)

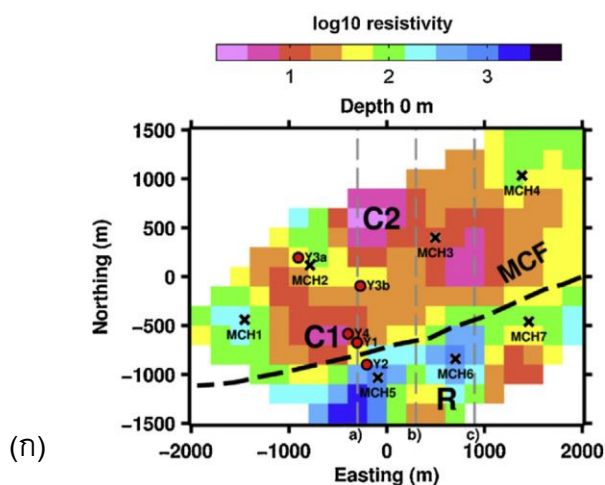
รูปที่ 7ก) แสดงให้เห็นถึงสภาพต้านทานไฟฟ้าของพื้นที่โดยรอบน้ำพุร้อนป่าติ่ง ซึ่งจะเห็นได้ว่าสามารถแบ่งออกได้เป็น สาม ลักษณะ ใหญ่ๆ ด้วยกันคือ (1) บริเวณ conductive bodies C1 & C2 (2) บริเวณ resistive body R และ (3) แนวรอยต่อระหว่าง conductive zone ในตอนเหนือ กับแนว resistive zone ในตอนใต้ รูปที่ 7ข) บ่งบอกว่าพื้นที่ C1 & C2 นั้นมีระดับตื้นๆ ไม่กี่ร้อยเมตร โดย C1 น่าจะลึกไม่เกิน 200 เมตร ในขณะที่ C2 อาจลึกได้มากถึง 500 เมตร ส่วน พื้นที่ R นั้นมีขนาดที่ใหญ่ และลึกลงไปใต้ดิน ส่วนแนวรอยต่อระหว่างค่าสภาพต้านทานไฟฟ้าที่ต่างกันก็ยาวต่อเนื่องลงไปได้ พื้นดินเช่นกัน



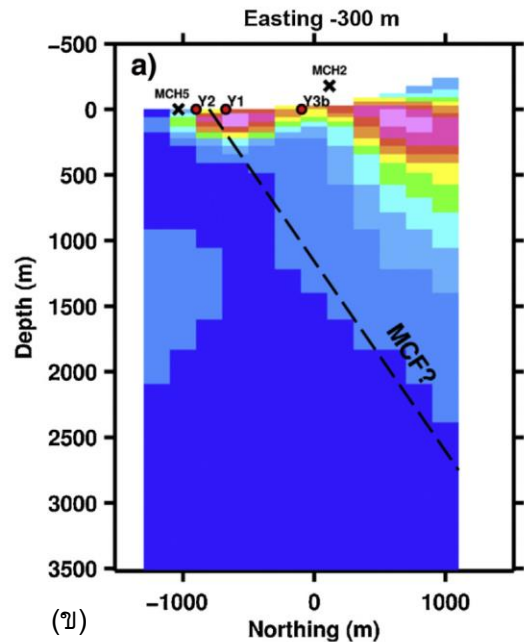
(ก)

(ข)

รูปที่ 6. (ก) แผนที่ธรณีวิทยาแสดงพื้นที่น้ำพุร้อนป่าตึง จ.เชียงราย และภาคเหนือตอนบนของประเทศไทย พื้นที่ที่กรอบสี่เหลี่ยมขยายให้เห็นในรูป (ข) Y1, Y2, Y3 และ Y4 (วงกลมสีแดง) แสดงให้เห็นถึงบริเวณที่มีน้ำร้อนพุขึ้นมาจากพื้นผิว ทั้งแบบธรรมชาติและโดยการขุดเจาะ ตำแหน่งสถานีแสดงด้วยเครื่องหมายกากบาทและเขียนกำกับด้วยชื่อ MCH1 – MCH7



(ก)



(ข)

รูปที่ 7. แบบจำลองสภาพต้านทานไฟฟ้าแบบสามมิติ (ก) top view ที่ความลึก 0 เมตร (พื้นผิว) ขนาดเท่ากับพื้นที่ในรูป 6ข) และ (ข) ภาคตัดขวาง ตามแนว a) ในรูป ก)

เมื่อนำสภาพด้านทานไฟฟ้าที่ได้ในรูปที่ 7 ไปพิจารณากับความเป็นจริงทางธรณีวิทยา ทำให้ผู้วิจัยสามารถสรุปออกมาได้ในลักษณะดังนี้ พื้นที่ C1 & C2 สอดคล้องกับบริเวณที่พบน้ำพุร้อนที่พื้นผิว ดังนั้นจึงแปลความว่า อาจเป็น geothermal reservoir ระดับตื้น คือ เป็นพื้นที่ที่มีน้ำร้อนจากที่ลึกขึ้นมา กักเก็บตามรูปทรงของหินในบริเวณใกล้กับพื้นดิน และคอยป้อนน้ำร้อนให้กับน้ำพุร้อนที่พื้นผิวอย่างต่อเนื่อง ส่วนพื้นที่ R นั้นสอดคล้องกับหินแกรนิตในแผนที่ธรณีวิทยา (รูปที่ 6ก) และค่าสภาพด้านทานไฟฟ้าก็สอดคล้องกัน นอกจากนี้ การที่พื้นที่ R มีขนาดที่ลึกลงไปใต้พื้นดินและมีขนาดใหญ่ (รูปที่ 6ข) ก็ยิ่งสนับสนุนความสอดคล้องของพื้นที่ R กับหินแกรนิต ดังนั้นในการแปลความหมายของข้อมูลในครั้ง จึงสรุปว่า พื้นที่ R น่าจะบ่งบอกถึงหินแกรนิตในพื้นที่ ในขณะที่เดียวกัน แนวรอยต่อของทั้ง conductive bodies C1 & C2 และ resistive body R (รูปที่ 7ก) ก็สอดคล้องกับแนวรอยเลื่อนแม่จันตามแผนที่ธรณีวิทยา (รูปที่ 6) แม้ว่าเมื่อลงไปในระดับลึกแล้ว แนวรอยเลื่อนยังไม่ชัดเจนว่าจะอยู่ในแนวตั้ง ตามที่สภาพธรณีวิทยาบ่งชี้ หรือว่าเอียงตัว ซึ่งการจะกำหนดให้ได้มากขึ้น คงต้องวางสถานีสำรวจให้มากกว่านี้

จากข้อมูล MT ที่ได้จากการสำรวจนาร่อง จนได้ภาพสภาพด้านทานไฟฟ้าแบบสามมิติ บ่งชี้ให้เห็นว่า ธรณีวิทยาและโครงสร้างของน้ำพุร้อนป่าตึง เป็นดังต่อไปนี้ คือ น้ำพุร้อนป่าตึงได้รับน้ำร้อนจากแหล่งกักเก็บ (geothermal reservoir) ระดับตื้นที่อยู่บริเวณใกล้กับบริเวณที่น้ำพุขึ้นที่พื้นผิว แม้ว่าข้อมูลนี้จะไม่สามารถบ่งบอกถึงอุณหภูมิของหินแกรนิตได้ แต่การที่มีหินแกรนิตอยู่ภายใต้บริเวณน้ำพุร้อนนี้ บ่งบอกว่า หินแกรนิตเป็นแหล่งกำเนิดความร้อนให้กับน้ำร้อนใต้ดิน คล้ายคลึงกับแหล่งกำเนิดน้ำร้อนในแหล่งอื่นๆ ทั่วโลก เมื่อน้ำใต้ดินร้อนขึ้นก็จะแทรกตัวลอยขึ้นไปตามแนวรอยเลื่อนแม่จัน เพื่อขึ้นมาที่พื้นผิว แต่เนื่องจากพื้นที่ที่ยอมให้น้ำร้อนพุขึ้นที่พื้นผิวมีไม่กี่แห่ง เมื่อเทียบกับปริมาณน้ำที่มี น้ำที่ร้อนจึงรวมตัวกันกลายเป็นแหล่งกักเก็บน้ำร้อนระดับตื้น

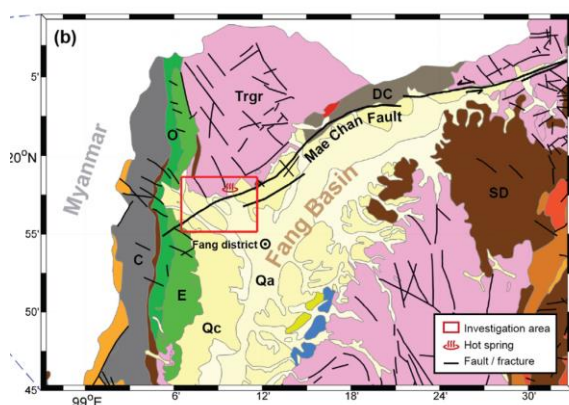
สำหรับรายละเอียดอื่นๆ ทั้งทางด้านเทคนิค และการแปลความ ผู้สนใจสามารถดูได้เพิ่มเติมได้ใน

- Puwis Amatyakul, Tawat Rung-Arunwan, and **Weerachai Siripunvaraporn**, 2015, A pilot magnetotelluric survey for geothermal exploration in Mae Chan region, northern Thailand, Geothermics, 55, 31 – 38. (IF2015 = 2.323)

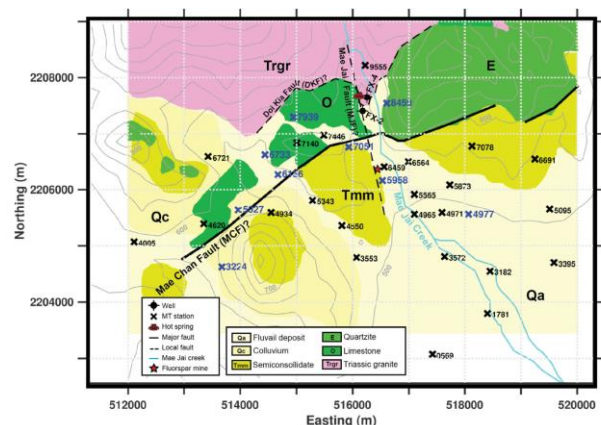
5.2. การสำรวจแหล่งพลังงานความร้อนใต้พิภพ น้ำพุร้อนฝาง จ.เชียงใหม่

พื้นที่น้ำพุร้อนฝางเป็นพื้นที่ที่สำคัญ เพราะว่าพื้นที่แห่งนี้เป็นพื้นที่เดียวในประเทศไทย ที่มีโรงไฟฟ้าพลังงานความร้อนใต้พิภพอยู่ เพียงแต่ว่าเป็นโรงงานขนาดเล็ก (สำหรับ demonstration) สร้างขึ้นมากว่า 20 ปีแล้ว จุดประสงค์เพื่อเป็นต้นแบบให้มีการพัฒนาต่อไป แม้ว่าจะผ่านไปกว่า 20 ปี การพัฒนายังไม่เกิดขึ้น ทั้งนี้เพราะว่าไม่สามารถประเมินศักยภาพของแหล่งกักเก็บน้ำร้อนได้อย่างมีประสิทธิภาพ เพราะเนื่องจากในอดีตการสำรวจในระดับลึกในหลักหลายร้อยเมตรถึงกิโลเมตร ยังเป็นไปได้อย่างยากหลังจากที่ได้มีการทำสำรวจ MT นำร่องในพื้นที่แห่งนี้มาแล้ว ทำให้เกิดโครงการต่อเนื่อง คือ การสำรวจน้ำพุร้อนฝาง โดยในขั้นตอนนี้ เพื่อดูภาพรวมของระบบน้ำพุร้อนของฝาง ก่อนที่ขั้นต่อไปจะ pin point ลงในพื้นที่ที่สำคัญ เพื่อประเมินศักยภาพอีกครั้ง

การสำรวจ MT ในครั้งนี้ กระทำขึ้นในพื้นที่น้ำพุร้อนฝาง จ.เชียงใหม่ (รูปที่ 8ก) โดยมีสถานี MT มากถึง 31 สถานี กินพื้นที่ประมาณ 6 km x 8 km (รูปที่ 8ข) โดยมีน้ำพุร้อนฝางอยู่ในทางเหนือของพื้นที่สำรวจ ซึ่งเป็นที่น่าเสียดายที่ไม่สามารถเข้าไปทำการสำรวจทางตอนเหนือของพื้นที่น้ำพุร้อนได้ เพราะว่าเป็นอุทยานแห่งชาติ การสำรวจเกือบทั้งหมดจึงเป็นพื้นที่ทางตอนล่างของน้ำพุร้อน (รูปที่ 8ข) จุดประสงค์หลักๆ ของการสำรวจครั้งนี้ ก็เพื่อพิสูจน์ว่าระบบแหล่งพลังงานความร้อนใต้พิภพของฝางนั้น คล้ายคลึงกับที่ถูกนำเสนอมาก่อนหน้านี้ แสดงในรูปที่ 9 ซึ่งประกอบไปด้วย แหล่งกักเก็บระดับตื้น หินร้อนที่ให้ความร้อนกับน้ำร้อน และรอยเลื่อนที่ทำให้น้ำร้อนไหลขึ้นมาที่พื้นผิว และยังช่วยในการระบุด้วยว่า แหล่งกักเก็บที่เห็นนั้นมีขนาดเท่าไร ลึกประมาณเท่าไร ข้อมูลเหล่านี้สำคัญต่อการประเมินศักยภาพของพื้นที่ต่อการสร้างโรงไฟฟ้าพลังงานความร้อนใต้พิภพในอนาคต ที่มีขนาดใหญ่กว่าโรงไฟฟ้าที่มีอยู่ในปัจจุบัน

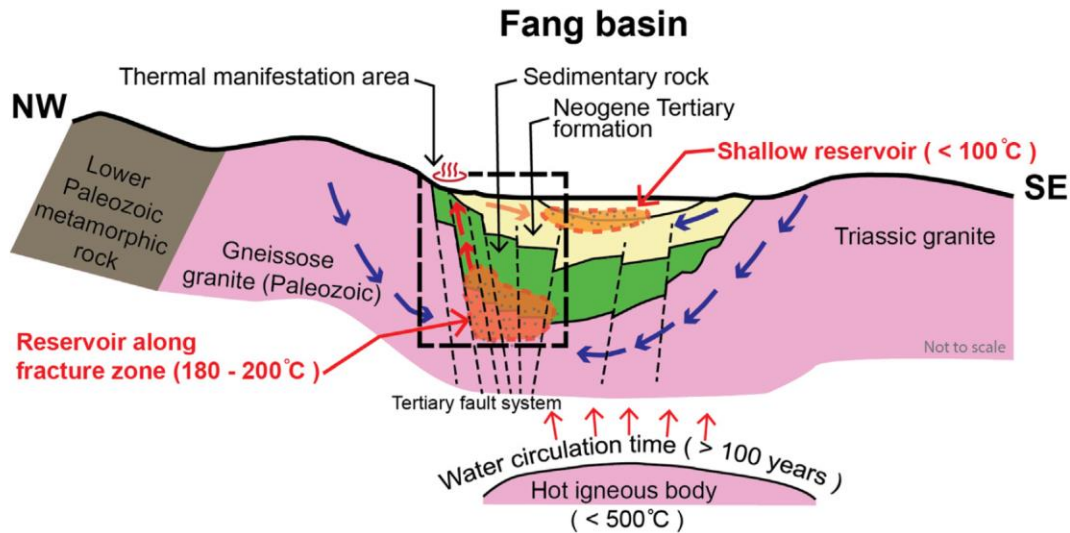


(ก)



(ข)

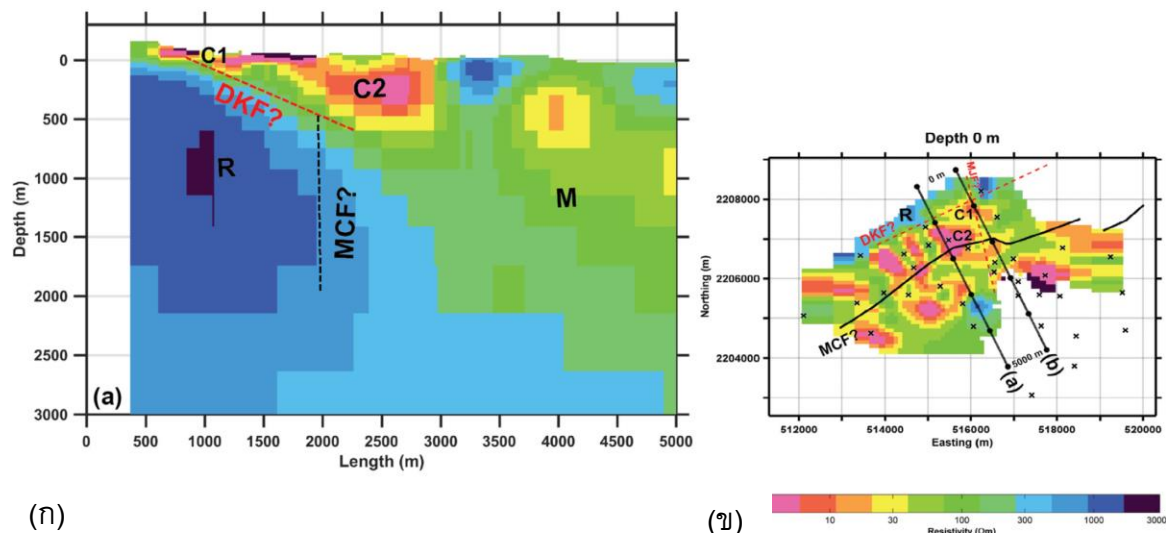
รูปที่ 8. (ก) แผนที่ธรณีวิทยาแสดงพื้นที่น้ำพุร้อนฝาง จ.เชียงใหม่ และภาคเหนือตอนบนของประเทศไทย พื้นที่กรอบสี่เหลี่ยมขยายให้เห็นในรูป (ข) Fx-2 & Fx-4 (แสดงด้วยรูปน้ำพุร้อน) และ ดาวสีแดง แสดงให้เห็นถึงบริเวณที่มีน้ำร้อนพุ่งขึ้นมาที่พื้นผิว ทั้งแบบธรรมชาติและโดยการขุดเจาะ ตำแหน่งสถานีแสดงด้วยเครื่องหมาย และเขียนกำกับด้วยตัวเลข



รูปที่ 9. แบบจำลองธรณีวิทยาของระบบการเกิดน้ำพุร้อนฝาง เสนอโดย Takashima and Kawada (1981) และ Takashima and Jarach (1987) บริเวณกรอบสี่เหลี่ยมคือบริเวณที่ทีมงานผู้วิจัยทำการวิจัย

หลังการสำรวจ ข้อมูลที่ได้ถูกนำไปประมวลผล และแก้ไขค่า static shift ด้วยข้อมูล DCR ที่เก็บร่วม และทำ 3-D inversion โดยโปรแกรมที่พัฒนาขึ้นมาก่อนหน้านี้ ผลการสำรวจแสดงให้เห็นด้วยแผนที่สภาพต้านทานไฟฟ้า แบบสามมิติ (รูปที่ 10) โครงสร้างหลักๆ ที่สามารถสังเกตเห็นได้ ได้แก่ โครงสร้าง conductive anomalies C1 & C2 โครงสร้าง resistive body R และ แนวรอยต่อระหว่างโครงสร้าง conductive & resistive คล้ายคลึงกับในกรณีของน้ำพุร้อนป่าตึง ดังนั้นการแปลความหมายในกรณีของพื้นที่ฝาง ก็มีความคล้ายคลึงเช่นเดียวกัน

พื้นที่ C1 เป็นพื้นที่ที่อยู่ใต้บริเวณที่มีน้ำพุร้อนที่พื้นผิวจำนวนมาก จึงไม่ใช่เรื่องยากที่จะแปลความว่าเป็นแหล่งกักเก็บน้ำร้อนบริเวณพื้นผิว ส่วน C2 เกิดในตำแหน่งห่างจาก C1 ประมาณ 1 กิโลเมตร ก่อนหน้านี้ ประมาณปีค.ศ. 1984 มีรายงานว่าพบน้ำร้อนผุดขึ้นที่พื้นผิวบริเวณนี้ ในระหว่างการขุดทำเหมืองฟลูออไรด์ จากข้อมูลดังกล่าว จึงทำให้ผู้วิจัยแปลความหมายว่า C2 น่าจะเป็นพื้นที่ที่มีการกักเก็บน้ำร้อน คล้ายคลึงกับพื้นที่ C1 แต่ทว่าอยู่ลึกกว่าและมีขนาดใหญ่กว่า พื้นที่ C2 เป็นพื้นที่ที่ยังไม่เคยมีการสำรวจมาก่อน ดังนั้นถ้า C2 เป็นแหล่งกักเก็บจริง จะเป็นแหล่งสำคัญต่อการพัฒนาเพื่อให้ได้โรงไฟฟ้าพลังงานความร้อนใต้พิภพขนาดใหญ่มากกว่าเดิม พื้นที่ R ก็สอดคล้องชัดเจนกับบริเวณที่เป็นหินแกรนิต เมื่อดูในแนวลึก ก็จะได้เห็นว่ามีความหนาที่ใหญ่มาก ดังนั้นพื้นที่ R จึงถูกแปลความว่าเป็นหินแกรนิตมวลไพศาล ส่วนแนวรอยต่อระหว่าง resistive R กับ conductive zones ที่ปรากฏให้เห็นในระดับตื้น ในกรณีนี้สอดคล้องกับรอยเลื่อนดอยเกียบ (DKF) ส่วนรอยเลื่อนแม่จันในกรณีตัดผ่านพื้นที่บริเวณ C2 และ conductive zones อื่นๆ พอดี จึงทำให้ไม่เกิดเป็น resistivity contrast เหมือนในกรณีของรอยเลื่อน DKF



รูปที่ 10. แบบจำลองสภาพต้านทานไฟฟ้าแบบสามมิติ (ก) ภาคตัดขวาง ตามแนว (a) ในรูป ข) (ข) top view ที่ความลึก 0 เมตร (พื้นผิว) ขนาดเท่ากับพื้นที่ในรูป 8ข)

จากผลการสำรวจในครั้งนี้ พบว่าระบบพลังงานความร้อนใต้พิภพสำหรับพื้นที่น้ำพุร้อนผางนั้น เป็นไปตามหลักการทางธรณีวิทยาที่เคยเผยแพร่มาแล้ว ดังแสดงในรูปที่ 9 แต่จากการสำรวจในครั้งนี้ บ่งชี้เพิ่มเติมถึงขนาดและลักษณะของพื้นที่กักเก็บระดับตื้น (C2) ว่ามีขนาดเท่าไร และอยู่ห่างออกไป จากพื้นที่น้ำพุร้อนมากถึง 1 กิโลเมตร จึงเป็นองค์ความรู้ที่จะต้องทำการพิสูจน์ต่อไปในอนาคต ด้วยการสำรวจเพิ่มเติมและขุดเจาะ ก่อนที่จะประเมินศักยภาพครั้งสุดท้ายก่อนจะนำมาสู่โรงไฟฟ้าพลังงานความร้อนใต้พิภพ

สำหรับรายละเอียดอื่นๆ ทั้งทางด้านเทคนิค และการแปลความ ผู้สนใจสามารถดูได้เพิ่มเติมได้ใน

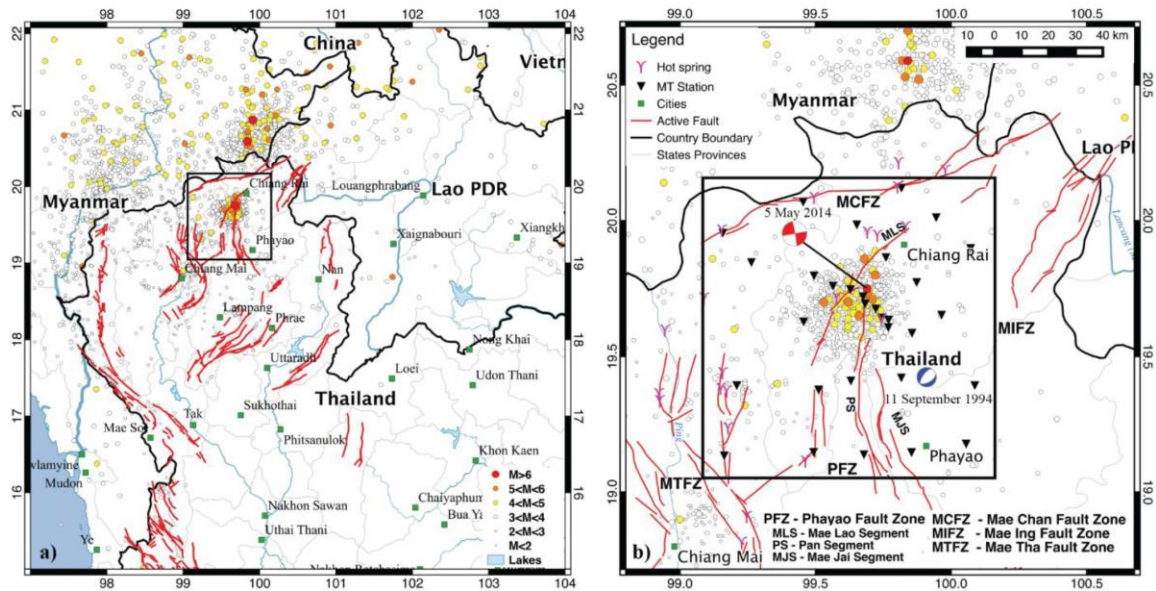
- Puwis Amatyakul, Songkhun Boonchaisuk, Tawat Rung-Arunwan, Chatchai Vachirastienchai, Spencer H. Wood, Kriangsak Pirarai, Aranya Fuangswasdi, and **Weerachai Siripunvaraporn**, 2016, Exploring the shallow geothermal fluid reservoir of Fang geothermal system, Thailand via a 3-D magnetotelluric survey, Geothermics, 64, 516 – 526. (IF2015 = 2.323)

5.3. การสำรวจรอยเลื่อนแม่ลาว ที่ก่อให้เกิดแผ่นดินไหวครั้งใหญ่ที่สุดในประเทศไทย

วันที่ 5 พ.ค. 2557 เป็นวันหนึ่งในประวัติศาสตร์ของประเทศไทย เป็นวันที่มีแผ่นดินไหวที่มีขนาดใหญ่ที่สุดในประเทศ (ตั้งแต่มีการติดตั้งเครื่องวัดแผ่นดินไหวในปี 2512) เกิดขึ้นในบริเวณกลุ่มรอยเลื่อนพะเยา (รูปที่ 11ก) ทางตอนเหนือของประเทศไทย โดยมีขนาดวัดได้ในขณะนั้น $ML = 6.2$ และยังมี aftershocks เกิดตามมาอีกหลายพันครั้ง หลังจากการทำการศึกษาใหม่ Noisagool et al. (2016) พบว่าขนาดของแผ่นดินไหว M_w มีขนาดเท่ากับ 6.5 แม้ว่าจะยังมีขนาดปานกลาง (ตามมาตรฐานสากล) แต่ก็เป็นที่ยืนยันว่ามีขนาดใหญ่ที่สุดในประเทศไทย แม้ว่าความเสียหายจะไม่มากนัก เนื่องจากจุดกำเนิดยังห่างไกลจากตัวเมืองเชียงราย แต่ก็ป็นสัญญาณเตือนภัยอย่างหนึ่งว่าแผ่นดินไหวในประเทศไทย ไม่ใช่เรื่องไกลตัวอีกต่อไป มีโอกาสเกิดขึ้นได้เช่นกัน

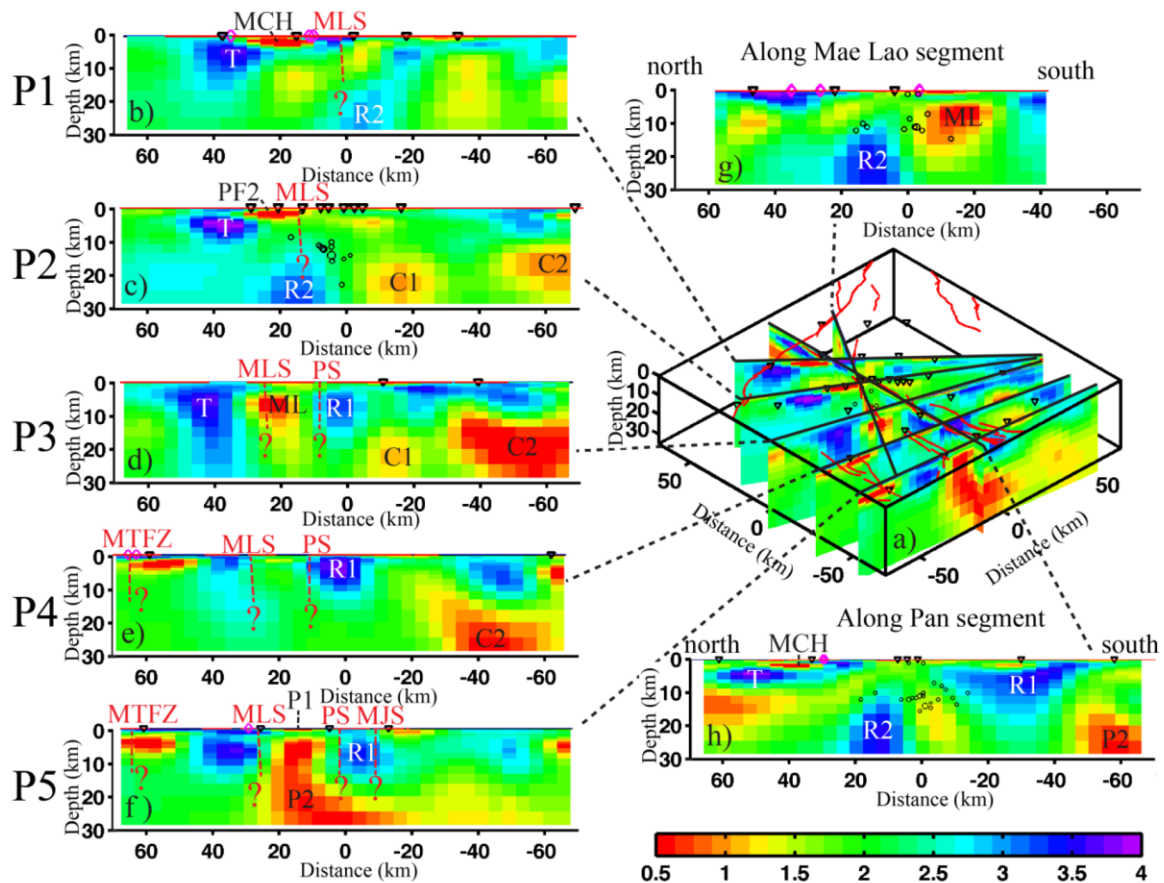
จากการศึกษาของ Noisagool et al. (2016) พบว่ารอยเลื่อนแม่ลาว (รูปที่ 11ข) ซึ่งเป็นหนึ่งในสามของระบบรอยเลื่อนพะเยา น่าจะเป็นตัวที่เคลื่อนไหวก่อน เมื่อเกิดการเคลื่อนไหว ก็จะส่งพลังงานต่อไปให้รอยเลื่อนพาน ซึ่งก็เป็นหนึ่งในสามของรอยเลื่อนพะเยา เกิดการเคลื่อนตัวตาม ทำให้เกิดการ aftershocks ตามมาเป็นจำนวนมากเพื่อปรับสภาพสมดุลของรอยเลื่อนทั้งระบบ หลังการเกิดแผ่นดินไหว ก็มีคำถามมากมายว่าทำไมกลุ่มรอยเลื่อนพะเยาถึงเกิดแผ่นดินไหวขึ้นได้และมีขนาดที่ใหญ่ เกิดความคาดหมาย ที่เป็นเช่นนี้ก็เพราะนักวิทยาศาสตร์ส่วนใหญ่ มุ่งเน้นไปว่ารอยเลื่อนที่น่าจะเกิดแผ่นดินไหวครั้งใหญ่ในประเทศไทย น่าจะเป็นรอยเลื่อนแม่จันที่อยู่ทางตอนเหนือของรอยเลื่อนพะเยา (รูปที่ 11ก) เพราะทั้งกลุ่มรอยเลื่อนแม่จัน และกลุ่มรอยเลื่อนพะเยาก็รับแรงผลักดันที่มาจากทางตอนเหนือของประเทศไทยอยู่ตลอดเวลาเช่นเดียวกัน

ดังนั้นจุดประสงค์ของการสำรวจในครั้งนี้ ก็เพื่อหาเหตุผลว่าทำไมกลุ่มรอยเลื่อนพะเยาถึงสามารถยับยั้งเขยื้อนได้เมื่อเปรียบเทียบกับรอยเลื่อนอื่นๆ ที่อยู่ใกล้เคียงโดยเฉพาะรอยเลื่อนแม่จัน สำหรับการสำรวจในครั้งนี้จะเน้นเฉพาะการศึกษาเกี่ยวกับรอยเลื่อนพะเยาเท่านั้น สถานีสำรวจ MT ถูกติดตั้งทั้งสิ้น 31 สถานี ดังแสดงในรูป 11ข) รอบๆ บริเวณกลุ่มรอยเลื่อนพะเยา

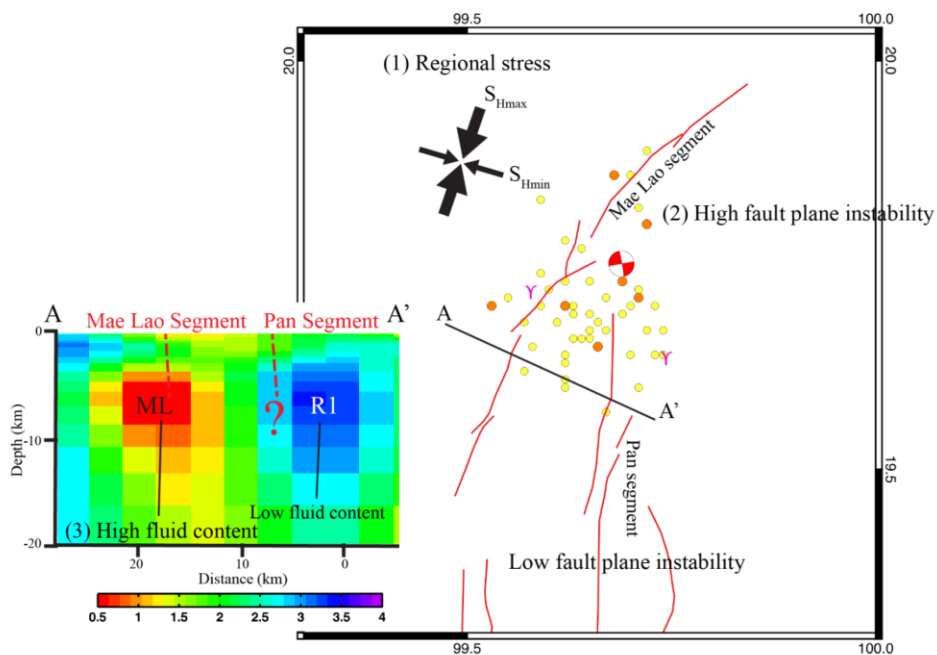


รูปที่ 11. (ก) แผนที่ประเทศไทยตอนเหนือ แสดงกลุ่มรอยเลื่อนต่างๆ และตำแหน่งที่เกิดแผ่นดินไหว เมื่อวันที่ 5 พ.ค. 2547 (ข) กลุ่มรอยเลื่อนพะเยา (PFZ) แบ่งได้ออกเป็นสามรอยเลื่อน ได้แก่ รอยเลื่อนแม่ลาว (MLS) รอยเลื่อนพาน (PS) และรอยเลื่อนแม่ใจ (MJS) ตำแหน่งการเกิดแผ่นดินไหว และ focal mechanism ของการเกิดแสดงในรูปตัววงกลม โดยขนาดเป็นตามสีที่แสดงในรูปที่ 11ก)

หลังการสำรวจ ข้อมูลที่ได้ถูกนำไปประมวลผล และแก้ไขค่า static shift ด้วยข้อมูล DCR ที่เก็บร่วม และทำ 3-D inversion โดยโปรแกรมที่พัฒนาขึ้นมาก่อนหน้านี้ ผลการสำรวจแสดงให้เห็นด้วยแผนที่สภาพต้านทานไฟฟ้า แบบสามมิติ (รูปที่ 12) โครงสร้างหลักๆ ที่สามารถสังเกตเห็นได้มีอยู่มากมาย ผู้สนใจสามารถติดตามได้ใน publication ในรายงานนี้จะนำเสนอเฉพาะ conductive ML ตามรูปที่ 12 ใน Profile P3 โดย ML นี้วางตัวอยู่ใต้รอยเลื่อนแม่ลาวที่ระดับความลึกประมาณ 3 – 10 km ซึ่งเป็นบริเวณที่อยู่ใกล้กับบริเวณที่เกิดแผ่นดินไหวเมื่อวันที่ 5 พ.ค. 2557 ในบริเวณใกล้เคียง กับ ML anomaly ยังมี R1 anomaly ซึ่งเป็นพื้นที่ resistive สูง โดย R1 นี้อยู่ใต้รอยเลื่อนพาน ทั้ง ML และ R anomalies มีผลต่อการแปลความหมายของงานวิจัยนี้มาก สำหรับกลไกการเกิดแผ่นดินไหวในครั้งนี้ สรุปได้เป็นแผนภาพแสดงในรูปที่ 13



รูปที่ 12. แผนที่แสดงสภาพต้านทานไฟฟ้าแบบสามมิติ โดย profile P1 – P5 แสดง cross-section ของพื้นที่สำรวจ



รูปที่ 13. แผนภาพแสดงบทสรุปกลไกของการเกิดแผ่นดินไหวที่ใหญ่ที่สุดในประเทศ

จากการศึกษาในครั้งนี้ ทำให้ทีมวิจัยสามารถสรุปกลไกการเกิดแผ่นดินไหวในครั้งนี้ได้ดังต่อไปนี้ (รูปที่ 13) (1) ภาคเหนือของประเทศไทยได้รับ stress สะสมมาโดยตลอดจากทางเหนือของประเทศ โดยทิศทางของ stress สอดคล้องกับทิศทางการวางตัวของรอยเลื่อนแม่ลาว (2) ด้วยทิศทางที่สอดคล้องกัน ผลที่ตามมาคือทำให้รอยเลื่อนแม่ลาว มี high instability (Noisagool et al., 2016) ในขณะที่รอยเลื่อนพานนั้นมี lower instability เพราะทิศของ stress กับการวางตัวของรอยเลื่อนพานไม่สอดคล้องกัน ดังนั้น ในกรณีนี้จึงหมายความว่า รอยเลื่อนแม่ลาวจึงมีแนวโน้มที่จะขยับเขยื้อนได้สูงกว่าเมื่อได้รับ stress มาอย่างต่อเนื่อง ข้อ (1) และ (2) เป็นผลมาจากการศึกษาก่อนหน้านี้ของ Noisagool et al. (2016) ในการสำรวจด้วยคลื่นแม่เหล็กไฟฟ้าในครั้งนี้ ยังพบอีกว่า (3) รอยเลื่อนแม่ลาวนั้นมี conductive zone ML อยู่ภายใต้ ซึ่งทีมงานแปลความหมายว่าน่าจะบ่งบอกถึงการมี fluid อยู่ในรอยเลื่อนสูง เมื่อรอยเลื่อนแม่ลาวมี fluid อยู่มาก ก็ยิ่งเพิ่มศักยภาพของการขยับเคลื่อนตัวได้สูงมากขึ้น เมื่อได้รับแรงกระทำอย่างต่อเนื่องในระดับเดียวกัน ในทางตรงกันข้าม ใกล้เคียง กับรอยเลื่อนพานกับพบว่าไม่มีบริเวณที่เป็น resistive zone มากกว่า บ่งบอกว่าได้รอยเลื่อนพานไม่ได้มี fluid เป็นองค์ประกอบ ดังนั้นการขยับเคลื่อนตัว ยังเป็นไปตามเงื่อนไขที่ (1) และ (2) เท่านั้น

สำหรับรายละเอียดอื่นๆ ทั้งทางด้านเทคนิค และการแปลความ ผู้สนใจสามารถดูได้เพิ่มเติมได้ใน

- Songkhun Boonchaisuk, Sutthipong Noisagool, Puwis Amatyakul, Tawat Rung-arunwan, Chatchai Vachiratienchai, and **Weerachai Siripunvaraporn**, 2017, 3-D magnetotelluric imaging of the Phayao Fault Zone, northern Thailand: evidence for saline fluid in the source region of the 2014 Chiang Rai earthquake, *moderate revision* for Journal of Asian Earth Sciences. (IF2015 = 2.647)

6. สรุปผล

ในโครงการนี้ ผู้วิจัยได้พัฒนาโปรแกรมแปลความหมายร่วมระหว่างข้อมูล DCR (Direct Current Resistivity) และเทคนิค MT (Magnetotelluric) โดยโปรแกรมแปลความหมายร่วมนี้ มีหลักการทำงานภายใต้เทคนิค data space Occam's inversion แต่การที่เอาข้อมูลที่มีความแตกต่างกันมารวมกัน ผลที่ได้คือสามารถกำจัดข้อด้อยของแต่ละเทคนิคออกไปได้ กล่าวคือ โดยปกติ เทคนิค DCR ใช้ได้เฉพาะการสำรวจในระดับตื้น และให้รายละเอียดสูงในแนวราบ ในขณะที่ข้อมูล MT จะให้ข้อมูลในระดับลึกมากกว่า ดังนั้นการเอาข้อมูลทั้งสองมารวมกันแปลความหมาย จะส่งผลให้การวิเคราะห์สามารถทำได้ทั้งในระดับตื้นและลึก นอกจากนี้ ข้อดีของการแปลความหมายร่วม คือ การเอาข้อมูล DCR มาช่วยในการแก้ไขปัญหา static shift ของข้อมูล MT ซึ่งเป็นปัญหาหลัก เมื่อ MT ถูกแก้ไขแล้ว ก็จะทำให้การแปลความหมายถูกต้องมากขึ้น

นอกจากนี้ ทางทีมผู้วิจัยยังได้นำเอาโปรแกรมที่พัฒนาขึ้นมาไปใช้ในการสำรวจแหล่งพลังงานความร้อนใต้พิภพสองพื้นที่ ได้แก่ พื้นที่น้ำพุร้อนป่าตึง จ.เชียงราย พื้นที่น้ำพุร้อนฝาง จ.เชียงใหม่ รวมทั้งการนำเอาไปใช้ในการสำรวจเพื่อดูกลไกการเกิดแผ่นดินไหว ของรอยเลื่อนแม่ลาวอีกด้วย

หนังสืออ้างอิง

- Amatyakul, P., Boonchaisuk, S., Rung-Arunwan, T., Vachiratienchai, C., Wood, S., Pirarai, K., Fuangswasdi, A., and Siripunvaraporn, W., 2016, Exploring the shallow geothermal fluid reservoir of Fang geothermal system, Thailand via a 3-D magnetotelluric survey, *Geothermics*, 64, 516 – 526.
- Amatyakul, P., Rung-Arunwan, T., and Siripunvaraporn, W., 2015, A pilot magnetotelluric survey for geothermal exploration in Mae Chan region, northern Thailand, *Geothermics*, 55, 31 – 38.
- Benson, A.K., Payne, K.L., Stubben, M.A., 1997, Mapping groundwater contamination using dc resistivity and VLF geophysical methods – A case study, *Geophysics*, 62, 80-86.
- Boonchaisuk, S., Vachiratienchai, C., Siripunvaraporn, W., 2008, Two-dimensional direct current (DC) resistivity inversion: Data space Occam's approach, *Physics of the Earth and Planetary Interiors* **168** (3-4), pp. 204-211
- Boonchaisuk, S., Siripunvaraporn, W., Ogawa, Y., 2013, Evidence for middle Triassic to Miocene dual subduction zones beneath the Shan-Thai terrane, western Thailand from magnetotelluric data, *Gondwana Research*, 23, 1607-1616.
- Boonchaisuk, S., Noisagool, S., Amatyakul, P., Rung-arunwan, T., Vachiratienchai, C., and Siripunvaraporn, W., 2017, 3-D magnetotelluric imaging of the Phayao Fault Zone, northern Thailand: evidence for saline fluid in the source region of the 2014 Chiang Rai earthquake, *moderate revision for Journal of Asian Earth Sciences*.
- Buselli, G., Lu, K., 2001. Groundwater contamination monitoring with multichannel electrical and electromagnetic methods. *J. Appl. Geophys.* 48, 11–23.
- Chen, C., Liu, J., Xia, J., and Li, Z., 2006, Integrated geophysical techniques in detecting hidden dangers in river embankments, *Jour. Envr. Engr. Geophys.*, 11, 83-94.
- Chen, L., Booker, J. R., Jones, A. G., Wu, N., Unsworth, M., Wei, W., and Tan, H., 1996, Electrically conductive crust in southern Tibet from INDEPTH magnetotelluric surveying: *Sciences*, **274**, 1694-1696.
- Constable, C. S., Parker, R. L., and Constable, C. G., 1987, Occam's inversion: A practical algorithm for generating smooth models from electromagnetic sounding data: *Geophysics*, **52**, 289–300.
- Constable S. and C. Weiss, 2006, Mapping thin resistors and hydrocarbons with marine EM methods: Insights from 1D modeling, *GEOPHYSICS* 71 (2): G43-G51.
- Goldie, M., 2007, A comparison between conventional and distributed acquisition induced polarization surveys for gold exploration in Nevada, *Leading Edges*, 26, 180-183.
- Harinarayana, T., Naganjaneyulu, K. and Patro, B.P.K., 2006, Detection of a collision zone in south Indian shield region from magnetotelluric studies, *Gondwana Res.*, 10, 48-56.
- Heise, W., Caldwell, T., Bibby, H., & Bannister, S., 2008. Three-dimensional modelling of magnetotelluric data from the rotokawa geothermal field, taupo volcanic zone, new zealand, *Geophysical Journal International*, 173(2), 740–750.
- Holz, S., Polag, D., Becken, M., Fiedler-Volmer, R., Zhang, H.C., Hartmann, K., and Burkhardt, H., 2007, Electromagnetic and geoelectric investigation of the Gurinai Structure, Inner Mongolia, NW China, *Tectonophysics*, 445, 26-48.
- Jones, A. G., 1992, Electrical conductivity of the continental lower crust, *in* Fountain, D. M., Arculus, R. J., and Kay, R. W., Eds., *Continental Lower Crust*: Elsevier Science Publ. Co., Inc., 81-143.
- Legault, J.M., Carriere, D. and Petrie, L., 2007, Synthetic model testing and distributed acquisition dc resistivity results over an unconformity uranium target from the Athabasca Basin, northern Saskatchewan, *Leading Edge*, 27, 46-51.
- Lenkey, L., Hamori, Z., Mihalfy, P., 2005, Investigating the hydrogeology of a water-supply area using direct-current vertical electrical sounding, *Geophysics*, 70, H11-H19.
- Meju, M.A., Fontes, S.L., Oliveira, M.F.B., Lima, J.P.R., Ulugergerli, E.U., and Carrasquilla, A.A., 1999. Regional aquifer mapping using combined VES-TEM- AMT/EMAP methods in the semi-arid eastern margin of Parnaiba Basin, Brazil. *Geophysics*, 64, 337-356.
- Monteiro Santos, F., Sultan, S.B., 2008. On the 3-D inversion of vertical electrical soundings: application to the south Ismailia area Cairo desert road, Cairo, Egypt. *J. Appl. Geophys.* 65, 97–110.
- Newman, G., Gasperikova, E., Hoversten, G., & Wannamaker, P., 2008. Three-dimensional magnetotelluric characterization of the coso geothermal field, *Geothermics*, 37(4), 369–399.
- Noisagool, S., Boonchaisuk, S., Pronopin, P. Siripunvaraporn, W., 2016. The regional moment tensor of the 5 May 2014 Chiang Rai earthquake (Mw = 6.5), Northern Thailand, with its aftershocks and its implication to the stress and the instability of the Phayao Fault Zone. *Journal of Asian Earth Sciences* 127, 231-246. <http://dx.doi.org/10.1016/j.jseaes.2016.06.008>
- Orange, A. S., 1989, Magnetotelluric Exploration for Hydrocarbons: *Proc. IEEE*, **77**, 287-317.

- Pedersen LB, Bastani M, Dynesius L, 2005, Groundwater exploration using combined controlled-source and radiomagnetotelluric techniques, *GEOPHYSICS* 70 (1): G8-G15
- Satitpittakul, A., Vachiratiengchai, C., and Siripunvaraporn, W., 2013, Factors influencing cavity detection in Karst terrain on two-dimensional (2-D) Direct Current (DC) resistivity survey: A case study from western part of Thailand, *Engineering Geology*, 152, 162-171.
- Shemang, E.M., and Molwalefhe, L.N., 2009, DC resistivity and seismic refraction survey across the SE margin of Lake Ngami, NW Botswana, *Acta Geophysica*, 57, 728-742.
- Siripunvaraporn, W., 2012, Three-Dimensional Magnetotelluric Inversion: An Introductory Guide for Developers and Users, *Surveys in Geophysics*, 33, 5 – 27.
- Siripunvaraporn W. and Egbert, G. D., 2000, An Efficient Data-Subspace Inversion for Two-Dimensional Magnetotelluric Data, *Geophysics*, **65**, 791-803.
- Siripunvaraporn, W., Egbert, G., and Lenbury, Y., 2002, Numerical accuracy of magnetotelluric modeling: A comparison of finite difference approximations, *Earth Planets Space*, **54**: 721-725.
- Siripunvaraporn W., Egbert, G., Lenbury, Y. and Uyeshima, M., 2005, Three-dimensional Magnetotelluric Inversion: Data Space Method, *Physics of the Earth and Interior*, **150**, 3-14.
- Siripunvaraporn W., G. Egbert and M. Uyeshima, 2005, Interpretation of 2-D Magnetotelluric Profile Data with 3-D Inversion: Synthetic Examples, *Geophys. Jour. Inter.* , **160**, 804-814.
- Siripunvaraporn W. and G. Egbert, 2007, Data space conjugate gradient inversion for 2-D Magnetotelluric data, *Geophys. Jour. Inter.*, 170, 986-994.
- Siripunvaraporn W. and G. Egbert, 2009, WSINV3DMT: Vertical Magnetic Field Transfer Function Inversion and Parallel Implementation, *Physics of the Earth and Planetary Interiors* **173** (3-4), pp. 317-329
- Siripunvaraporn, W. & Sarakorn, W., 2011. An efficient data space conjugate gradient occam's method for three dimensional magnetotelluric inversion, *Geophys. J. Int.*, 186(2), 567–579.
- Tuncer, V., M. J. Unsworth, W. Siripunvaraporn, and J.A. Craven, 2006, Exploration for unconformity-type uranium deposits with audiomagnetotelluric data: A case study from the McArthur River mine, Saskatchewan, Canada, *Geophysics*, 71, B201-B209.
- Unsworth M., Bedrosian, P., Eisel, M., Egbert, G. and Siripunvaraporn, W., 2000, Along strike variations in the electrical structure of the San Andreas Faults at Parkfield, California, *Geophys. Res. Lett.*, **27**, 3021-3024.
- Vachiratiengchai, C., and Siripunvaraporn, W., 2013, An efficient inversion for two-dimensional direct current resistivity surveys based on the hybrid finite difference – finite element method, *Physics of the Earth and Planetary Interiors*, 215, 1-11.
- Vachiratiengchai C, Boonchaisuk S, Siripunvaraporn W, 2010, A hybrid finite difference-finite element method to incorporate topography for 2D direct current (DC) resistivity modeling. *Phys Earth Planet*, 183(3-4):426-34
- Vozoff, K., 1972, The Magnetotelluric Method in the Exploration of Sedimentary Basins: *Geophysics*, **37**, 98-141.
- Wilson, S., Ingham, M., McConchie, J., 2006. The applicability of earth resistivity methods for saline interface definition. *J. Hydrol.* 316, 301–312.

Output ที่ได้จากโครงการ

ผลงานตีพิมพ์ในวารสารวิชาการนานาชาติ (published)

- Puwis Amatyakul, Chatchai Vachiratienchai and **Weerachai Siripunvaraporn**, 2017, WSJointInv2D-MT-DCR: An efficient joint two-dimensional magnetotelluric and direct current resistivity inversion, Computers & Geosciences, 102, 100-108. (IF 2015 = 2.474)
- Puwis Amatyakul, Songkhun Boonchaisuk, Tawat Rung-Arunwan, Chatchai Vachiratienchai, Spencer H. Wood, Kriangsak Pirarai, Aranya Fuangswasdi, and **Weerachai Siripunvaraporn**, 2016, Exploring the shallow geothermal fluid reservoir of Fang geothermal system, Thailand via a 3-D magnetotelluric survey, Geothermics, 64, 516 – 526. (IF2015 = 2.323)
- Puwis Amatyakul, Tawat Rung-Arunwan, and **Weerachai Siripunvaraporn**, 2015, A pilot magnetotelluric survey for geothermal exploration in Mae Chan region, northern Thailand, Geothermics, 55, 31 – 38. (IF2015 = 2.323)

ผลงานตีพิมพ์ในวารสารวิชาการนานาชาติ (moderate revision)

- Songkhun Boonchaisuk, Sutthipong Noisagool, Puwis Amatyakul, Tawat Rung-arunwan, Chatchai Vachiratienchai, and **Weerachai Siripunvaraporn**, 2017, 3-D magnetotelluric imaging of the Phayao Fault Zone, northern Thailand: evidence for saline fluid in the source region of the 2014 Chiang Rai earthquake, *moderate revision* for Journal of Asian Earth Sciences. (IF2015 = 2.647)

การเสนอผลงานในที่ประชุมวิชาการนานาชาติบางส่วน

- Weerachai Siripunvaraporn, 2017, Three-dimensional Magnetotelluric Inversion, The 1st Geo Electromagnetic Workshop 2017, Bandung, Indonesia, 20 – 24 Feb.
- Puwis Amatyakul, Songkhun Boonchaisuk, Tawat Rung-Arunwan, Chatchai Vachiratienchai, Spencer H. Wood, Kriangsak Pirarai, Aranya Fuangswasdi, Weerachai Siripunvaraporn, 2016, Imaging the Fang geothermal system with a 3-D magnetotelluric technique, the 11th Asian Geothermal Symposium, 18- 20 November, Chiang Mai, Thailand

- Keiichi ishizu, Chatchai Vachiratienchai, **Weerachai Siripunvaraporn**, Tada-nori Goto, 2016, Development of Two-Dimensional Inversion of Marine DC resistivity survey, Japan Geoscience Union Meeting 2016, May 22 – 26, Makuhari Messe, Japan.
- Tawat Rung-Arunwan, **Weerachai Siripunvaraporn**, Hisashi Utada, 2016, Detecting galvanic distortion, the 23rd Electromagnetic Induction Workshop, 2016, Aug 14 – 20, Chiang Mai, Thailand.
- Keiichi Ishizu, Chatchai Vachiratienchai, **Weerachai Siripunvaraporn**, Tada-nori Goto, 2016, Development of two dimensional inversion of marine DC resistivity survey, the 23rd Electromagnetic Induction Workshop, 2016, Aug 14 – 20, Chiang Mai, Thailand.
- Chatchai Vachiratienchai, Weerachai Siripunvaraporn, 2016, 3D Data-Space Occam's Inversion on the Application of Direct Current Resistivity Survey, the 23rd Electromagnetic Induction Workshop, 2016, Aug 14 – 20, Chiang Mai, Thailand.
- Sarunya Chomchaiya, **Weerachai Siripunvaraporn**, Chatchai Vachiratienchai, 2016, Using the direct current resistivity method on leakage detection: a Tha Thung Na dam case study, the 23rd Electromagnetic Induction Workshop, 2016, Aug 14 – 20, Chiang Mai, Thailand.
- Songkhun Boonchaisuk, Benjawut Piromfong, Tawat Rung-Arunwan, Puwis Amatyakul, **Weerachai Siripunvaraporn**, 2016, Three-dimensional resistivity structure beneath Payao Fault zone, northern Thailand: preliminary result, the 23rd Electromagnetic Induction Workshop, 2016, Aug 14 – 20, Chiang Mai, Thailand.
- Sarunya Chomchaiya, Chatchai Vachiratienchai, **Weerachai Siripunvaraporn**, 2016, Leakage detection with the direct current resistivity method: A study of Tha Thung Na dam case, Siam Physics Congress 2016, June 8 – 10, Ubonrachatani, Thailand

การนำผลงานวิจัยไปใช้ประโยชน์

☒ ด้านชุมชนและพื้นที่ โดยใคร กรมทรัพยากรน้ำบาดาล

มีการนำไปใช้อย่างไร

จากผลงานวิจัยที่ได้ นำ รวมทั้งข้อมูลอื่นๆ ทำให้กรมทรัพยากรน้ำบาดาลได้ลงพื้นที่ และทำการขุดเจาะ (อยู่ในขั้นตอนของการขุดเจาะ) ที่ อ.แม่จัน จ.เชียงราย โดยถ้าผลการขุดเจาะออกมาตามที่คาดการณ์ไว้ น้ำร้อนที่ขุดเจาะออกมา ก็จะนำไปทำประโยชน์มากมาย มากกว่าในตอนนี้ที่เน้นใช้ทำเฉพาะท่องเที่ยว เช่นสปา และอุตสาหกรรมเกษตรเล็ก เช่นใช้ในการอบผลไม้ แต่เป้าหมายในตอนนี้จะเป็นโรงไฟฟ้า เมื่อสร้างสำเร็จรวมทั้งการเพิ่มขยายขนาดอุตสาหกรรมเกษตรและท่องเที่ยว ให้ใหญ่ขึ้น ก็จะทำให้ชุมชน และพื้นที่มีรายรับต่อครัวเรือนมากขึ้น

☒ ด้านวิชาการ โดยใคร ภาควิชาฟิสิกส์ คณะวิทยาศาสตร์ มหาวิทยาลัยมหิดล

มีการนำไปใช้อย่างไร (กรุณาให้ข้อมูลเจาะจง)

จากผลการดำเนินงานของโครงการวิจัยนี้ สามารถสร้างองค์ความรู้ใหม่ (journal paper) ได้ถึงสี่เปเปอร์ สามารถผลิตตัวโปรแกรมคอมพิวเตอร์แปลความหมายร่วมได้ และผลิตบุคลากรทางด้านธรณีฟิสิกส์ ของประเทศได้อีกด้วย

ภาคผนวก

ภาคผนวก ก. Reprint

- Puwis Amatyakul, Chatchai Vachiratienchai and **Weerachai Siripunvaraporn**, 2017, WSJointInv2D-MT-DCR: An efficient joint two-dimensional magnetotelluric and direct current resistivity inversion, Computers & Geosciences, 102, 100-108. (IF 2015 = 2.474)

ภาคผนวก ข. Reprint

- Puwis Amatyakul, Songkhun Boonchaisuk, Tawat Rung-Arunwan, Chatchai Vachiratienchai, Spencer H. Wood, Kriangsak Pirarai, Aranya Fuangswasdi, and **Weerachai Siripunvaraporn**, 2016, Exploring the shallow geothermal fluid reservoir of Fang geothermal system, Thailand via a 3-D magnetotelluric survey, Geothermics, 64, 516 – 526. (IF2015 = 2.323)

ภาคผนวก ค. Reprint

- Puwis Amatyakul, Tawat Rung-Arunwan, and **Weerachai Siripunvaraporn**, 2015, A pilot magnetotelluric survey for geothermal exploration in Mae Chan region, northern Thailand, Geothermics, 55, 31 – 38. (IF2015 = 2.323)

ภาคผนวก ง. Reprint of the revised version

- Songkhun Boonchaisuk, Sutthipong Noisagool, Puwis Amatyakul, Tawat Rung-arunwan, Chatchai Vachiratienchai, and **Weerachai Siripunvaraporn**, 2017, 3-D magnetotelluric imaging of the Phayao Fault Zone, northern Thailand: evidence for saline fluid in the source region of the 2014 Chiang Rai earthquake, *moderate revision* for Journal of Asian Earth Sciences. (IF2015 = 2.647)

ภาคผนวก ก. Reprint

- Puwis Amatyakul, Chatchai Vachiratiengchai and **Weerachai Siripunvaraporn**, 2017, WSJointInv2D-MT-DCR: An efficient joint two-dimensional magnetotelluric and direct current resistivity inversion, Computers & Geosciences, 102, 100-108. (IF 2015 = 2.474)



Case study

WSJointInv2D-MT-DCR: An efficient joint two-dimensional magnetotelluric and direct current resistivity inversion

Puwis Amatyakul^a, Chatchai Vachiratiengchai^b, Weerachai Siripunvaraporn^{a,*}^a Department of Physics, Faculty of Science, Mahidol University, 272 Rama 6 Rd., Rachatawee, Bangkok 10400, Thailand^b Curl-E Geophysics Co. Ltd., 85/87 M. Nantawan Utthayan-Aksa Rd., Salaya, Phutthamonthon, Nakornpathom 73170, Thailand

ARTICLE INFO

Keywords:

Direct current resistivity
Magnetotelluric
Joint inversion
Data space Occam method

ABSTRACT

An efficient joint two-dimensional direct current resistivity (DCR) and magnetotelluric (MT) inversion, referred to as WSJointInv2D-MT-DCR, was developed with FORTRAN 95 based on the data space Occam's inversion algorithm. Our joint inversion software can be used to invert just the MT data or the DCR data, or invert both data sets simultaneously to get the electrical resistivity structures. Since both MT and DCR surveys yield the same resistivity structures, the two data types enhance each other leading to a better interpretation. Two synthetic and a real field survey are used here to demonstrate that the joint DCR and MT surveys can help constrain each other to reduce the ambiguities occurring when inverting the DCR or MT alone. The DCR data increases the lateral resolution of the near surface structures while the MT data reveals the deeper structures. When the MT apparent resistivity suffers from the static shift, the DCR apparent resistivity can serve as a replacement for the estimation of the static shift factor using the joint inversion. In addition, we also used these examples to show the efficiency of our joint inversion code. With the availability of our new joint inversion software, we expect the number of joint DCR and MT surveys to increase in the future.

1. Introduction

The direct current resistivity (DCR) and all types of the magnetotelluric (MT) surveys yield cross-sections of resistivity from which the physical structure may be determined. They are used worldwide for many different purposes. The DCR method is mostly used for near surface surveys (e.g., Buselli and Lu, 2001; Satitpittakul et al., 2013; Wilson et al., 2006) and surveys to depths of up to a few hundred meters (e.g., Meju et al., 1999; Monteiro Santos and Sultan, 2008) due to its source power limitation. In contrast to DCR surveys which use man-made sources, an audio-magnetotelluric (AMT) and MT surveys use natural electromagnetic signals for sensing from shallow exploration to mid-crust (e.g., Tuncer et al., 2006; Amatyakul et al., 2015; Amatyakul et al., 2016) and to deeper Earth (e.g., Boonchaisuk et al., 2013; Farquharson and Craven, 2009; Sinharay et al., 2010; Wang et al., 2014). For very shallow surveys, remote radio transmitters operating in the VLF and LF replaced the natural EM signals of the Earth for the radio-magnetotelluric (RMT) method (e.g., Linde and Pedersen, 2004; Tezkan et al., 2005; Tezkan and Saraev, 2008; Tullen et al., 2006).

As the two methods use a different technique to probe the resistivity of the Earth, they are often used together to constrain the interpreta-

tion. There are two ways of the methods to restrict the explanation. First, the data were inverted separately to produce two resistivity structures at different scales. The results are then “manually” combined to produce a compatible interpretation (e.g., Diaferia et al., 2008; Shan et al., 2014). In the case where the joint inversion software is available, the data from both techniques are inverted together to constrain the interpretation (e.g., Bastani et al., 2012; Candansayar and Tezkan, 2008; Monteiro Santos et al., 1997, 2007; Sasaki, 1989; Seher and Tezkan, 2007; Tezkan et al., 1996; Yogeshwar et al., 2012; Kalscheuer et al., 2013; Shan et al., 2014). Since an advantage of one technique can help mitigate a drawback of the other technique, for example, as mentioned in Kalscheuer et al. (2010), the DC resistivity data is sensitive to both resistive and conductive structures, while the MT data senses the conductive structure better, the joint inversion often yields better results than individual inversion.

Although the joint interpretation from the DC Resistivity and MT data yields better results, the joint survey is still not conducted regularly. One main reason is the availability of the codes is still limited. When joint interpretation software is not available, few perform joint surveys which lead to insufficient examples for other researchers to follow. In this paper, we introduce an efficient joint inversion program for 2-D DCR and MT data based on

* Corresponding author.

E-mail address: wsiripun@gmail.com (W. Siripunvaraporn).

the popular Occam's data space technique (Siripunvaraporn, 2012; Siripunvaraporn and Egbert, 2000, 2009; Siripunvaraporn et al., 2005), referred to as WSJointInv2D-MT-DCR. We provide synthetic and real examples to show the benefits of the joint surveys and demonstrate the efficiency of our codes. With the availability of our new joint inversion software, we expect the number of joint DCR and MT surveys to increase significantly in the future.

2. The development of a joint DC resistivity and magnetotelluric methods based on the data space Occam's inversion

The inverted model based on Occam's method looks “geologically” reasonable and is preferred by many scientists (see Siripunvaraporn and Egbert (2000) and Siripunvaraporn et al. (2005)). The Occam's method also provides high stability, robustness and more rapid convergence to the solution (Constable et al., 1987; Siripunvaraporn, 2012; Siripunvaraporn and Egbert, 2000). The Occam's inversion can be divided into the classical and original model space method (Constable et al., 1987; deGroot-Hedlin and Constable, 1990) and the data space method (Siripunvaraporn, 2012; Siripunvaraporn and Egbert, 2000, 2009; Siripunvaraporn et al., 2005) which requires significantly less computational time and memory than the classical method. With these advantages, to make it readily use, the joint inversion of DCR and MT methods based on the data space Occam's technique was developed using Fortran 95. Note that this work is new, not the extension of the existing MT codes written with Fortran 77 (Siripunvaraporn and Egbert, 2000) nor the existing DCR code written with MATLAB (Vachiriatienchai and Siripunvaraporn, 2013). Since the method was well documented in our earlier publications (for the data space Occam's inversion technique, readers please see Boonchaisuk et al. (2008), Siripunvaraporn and Sarakorn (2011), Siripunvaraporn and Egbert (2000), Siripunvaraporn and Egbert (2009), Siripunvaraporn et al. (2005), Vachiriatienchai and Siripunvaraporn (2013), and Siripunvaraporn (2012); for the 2-D forward modeling and sensitivity calculation of the DCR data, please see Boonchaisuk et al. (2008) and Vachiriatienchai et al. (2010); Vachiriatienchai and Siripunvaraporn, 2013; for the 2-D forward modeling and sensitivity calculation of the MT data, please see Siripunvaraporn and Egbert (2000)), to avoid the detail redundancy we therefore only make a brief description of the technique for which the development of the joint inversion is required.

The data space Occam's inversion starts by perturbing the model \mathbf{m} and then updating the $(k+1)$ th iteration of the model, \mathbf{m}_{k+1} , through

$$\mathbf{m}_{k+1} - \mathbf{m}_0 = \mathbf{C}_m \mathbf{J}_k^T \mathbf{C}_d^{-1/2} [\mathbf{I} + \mathbf{C}_d^{-1/2} \mathbf{J}_k \mathbf{C}_m \mathbf{J}_k^T \mathbf{C}_d^{-1/2}]^{-1} \mathbf{C}_d^{-1/2} \mathbf{d}_k. \quad (1)$$

The updated model in Eq. (1) is guided by the data misfit $\mathbf{d}_k = \mathbf{d} - \mathbf{F}[\mathbf{m}_k] + \mathbf{J}_k(\mathbf{m}_k - \mathbf{m}_0)$ and the sensitivity (or Jacobian) matrix $\mathbf{J}_k = \partial \mathbf{F} / \partial \mathbf{m}_k$, where \mathbf{d} is the data, $\mathbf{F}[\mathbf{m}]$ is the calculated response, \mathbf{C}_d is the associated data covariance matrix, \mathbf{m}_0 is the prior model, \mathbf{C}_m is the model covariance matrix, \mathbf{I} is the identity matrix and λ^{-1} is the La Grange multiplier. The inversion keeps updating the model through Eq. (1) until the RMS misfit defined as $([(\mathbf{d} - \mathbf{F}[\mathbf{m}])^T \mathbf{C}_d^{-1/2} (\mathbf{d} - \mathbf{F}[\mathbf{m}])] / N)^{1/2}$ reaches the target misfit which is normally set at 1 RMS, where N is the total number of data.

The data vector \mathbf{d} for the 2-D MT inversion is the observed apparent resistivity (ρ_a^{MT}) and phase (ϕ^{MT}) of the transverse magnetic (TM) and transverse electric (TE) modes, while \mathbf{d} for the 2-D DCR inversion is only the observed apparent resistivity (ρ_a^{DCR}). Similar to Candansayar and Tezkan (2008) and Kalscheuer et al. (2010), to implement for the joint inversion, both data types must be combined, i.e., the data vector for the joint inversion $\mathbf{d}^{\text{T, Joint}} = [\mathbf{d}^{\text{MT}} \ \mathbf{d}^{\text{DCR}}]^T$, where $\mathbf{d}^{\text{MT}} = [\rho_a^{\text{MT}} \ \phi^{\text{MT}}]$ and $\mathbf{d}^{\text{DCR}} = [\rho_a^{\text{DCR}}]$, and similarly for the data covariance matrix. The number of the data N for the joint inversion is therefore the sum of the number of both data types, $N = N^{\text{MT}} + N^{\text{DCR}}$.

Similarly, for the data errors specified as diagonal elements of \mathbf{C}_d matrix, the number of elements is the same as the number of both data types. The influence of the data on the inversion results can be manipulated by the error bars. The data type that has smaller error bars has more control on the inverted model than the data type with larger error bars. Thus, to avoid the bias from one type of data, error bars of both data types should be adjusted to about the same level. Other ways to account for weighting the data can be seen in Kalscheuer et al. (2013), Kalscheuer et al. (2010) and Candansayar and Tezkan (2008).

Similarly, for the other vectors, $\mathbf{F}[\mathbf{m}]^T = [\mathbf{F}[\mathbf{m}]_{\text{MT}} \ \mathbf{F}[\mathbf{m}]_{\text{DCR}}]^T$, and $\mathbf{J}^T = [\mathbf{J}_{\text{MT}}; \ \mathbf{J}_{\text{DCR}}]^T$. The calculated response $\mathbf{F}[\mathbf{m}]_{\text{MT}}$ is calculated by solving the 2nd order Maxwell's equations using the finite-difference method (see Siripunvaraporn and Egbert, 2000). $\mathbf{F}[\mathbf{m}]_{\text{DCR}}$ is obtained by solving the continuity equation of the current density using a hybrid finite difference – finite element method (Vachiriatienchai et al., 2010; Vachiriatienchai and Siripunvaraporn, 2013). \mathbf{J}_{MT} and \mathbf{J}_{DCR} are calculated using the same system of equations as for $\mathbf{F}[\mathbf{m}]_{\text{MT}}$ and $\mathbf{F}[\mathbf{m}]_{\text{DCR}}$, respectively, along with the reciprocity technique (see Rodi, 1976; Siripunvaraporn, 2012; Siripunvaraporn and Egbert, 2000; and Vachiriatienchai and Siripunvaraporn, 2013).

Since both data types yield the same resistivity structure, the same model vector \mathbf{m} for the joint inversion can be used for both. The techniques sense structures at different depths (with DCR for shallow and MT for greater depths), the grid discretization for the same model must be designed to accommodate both techniques, and to guarantee the accuracy of the solutions from solving the forward problems. To obtain high accuracy for the forward problem of the DCR method, the grid discretization is designed based on the DCR configuration for the near surface part. Generally, two vertical grids are placed between the electrodes. For vertical discretization, the first vertical layer beneath the surface is fixed at around one-fourth of the electrode spacing. The thickness of the subsequent layers is then increased at a rate 1.2 – 1.5 times that of the previous one. Since MT can probe to greater depths, the grid discretization used for DCR is vertically extended to greater depths and is horizontally extended on both sides using larger grid spacing. This is to provide a high accuracy for the MT forward problem.

This grid discretization design for the joint inversion has led to a significantly larger number of model parameters M (the number of grids) than that of the individual inversions. The increase in M will lead to a longer computational time (CPU time) for solving the forward problems for both types of data. However, it will not have much effect on solving Eq. (1) as it was originally designed to depend on the number of data parameter N , rather than on M (see Siripunvaraporn (2012), Siripunvaraporn and Egbert (2000), Vachiriatienchai and Siripunvaraporn (2013)). Since N for the joint inversion is about twice as large as for the individual inversion, the CPU time and memory requirement for the joint inversion can be expected to be increased, but not as much as when solving the inverse problem based on the model space method.

Another matrix which is shared for both data types and very important for the joint inversion code to work properly is the model covariance matrix \mathbf{C}_m . It controls the smoothness size of the resistivity structure relative to the base model. Typically, for the model space method, \mathbf{C}_m^{-1} is required and is assigned as the first derivative roughness penalty (deGroot-Hedlin and Constable, 1990). As the inverse of the roughness operator is not possible for \mathbf{C}_m used in the data space method (Siripunvaraporn and Egbert, 2000), $\mathbf{C}_m \mathbf{J}^T$ in Eq. (1) is constructed via solving the 1-D diffusion equations as in Boonchaisuk et al. (2008), Siripunvaraporn and Egbert (2000), Siripunvaraporn et al. (2005) and Vachiriatienchai and Siripunvaraporn (2013), i.e. $\mathbf{C}_m \mathbf{J}^T \approx \mathbf{D}_H^T \mathbf{D}_V^T \mathbf{D}_V \mathbf{D}_H \mathbf{J}^T$, where \mathbf{D}_H and \mathbf{D}_V are the diffusion operators in horizontal and vertical directions, respectively. This provides two advantages. As \mathbf{C}_m is not necessary formed, no large memory is required to store \mathbf{C}_m . Since solving 1-D diffusion equations is fast, the calculation time for this process become insignificant comparing to other parts.

One important parameter of the diffusion equation is the diffusion length scale acting here as a controller for the smoothness of the resistive variation (for more detail see Appendix A of Siripunvaraporn and Egbert, 2000). Large diffusion length scale implies smooth gradient model but might result in higher misfit inversion, while small length scale reflects sharper gradient model which might result in overfit the data. Proper length scale is therefore necessary. Since both MT and DC Resistivity data has different resolving power, using fixed length scale as in the individual inversions would result in improper smoothness parameter for the joint inversion, and, consequently, might not converge to the target misfit. For individual inversion, the length scale is often fixed to be about the size of the electrode spacing for the DC Resistivity inversion (Vachiriatienchai and Siripunvaraporn, 2013), and about the length between stations for the MT inversion (Siripunvaraporn and Egbert, 2000). For the joint inversion, for the shallow structure which is influenced more by the DCR data, the diffusion length scale in the horizontal direction is designed to be about the size of the electrode spacing while the vertical length scale slightly increases with depth similar to the vertical grid discretization. At a depth approximately one-third of the DC resistivity profile length, the horizontal length scale is set to be about the distance between MT stations, while the vertical length scale still increases with depth according to the vertical grid discretization. This automatically adjusting length scale allows the joint inversion to cope with the divergent resolving power of the two data types.

3. Examples of joint inversions: synthetic and real examples and discussion

In this section, we use synthetic and real examples to show the efficiency of the code in terms of calculation, and also in terms of enhancing the interpretation of both MT and DCR data.

3.1. Joint RMT and DCR surveys help to enhance the interpretation

First, we check that our developed joint inversion code works effectively using a synthetic data set generated from the RMT and DCR surveys since both sense structures at about the same investigation depth. The synthetic model consists of two conductive anomalies (10 Ω m) and two resistive anomalies (1000 Ω m) buried in a 100 Ω m half-space at a depth of 5–35 m in a checkerboard pattern (Fig. 1a). This model was modified from the tested model presented in Kalscheuer et al. (2010). The model was discretized to generate the synthetic data for both types of data using a 148 \times 50 grids to ensure the accuracy of the synthetic data responses. However, for the inversion, the grid was reduced to 108 \times 40 to decrease the calculation time while ensuring that there was sufficient accuracy for the forward problems. The total number of model parameters is therefore $M = 4320$.

For the DCR data, we placed 41 electrodes with a spacing of 5 m to acquire up to the maximum pseudo-depth level for Wenner, Schlumberger, dipole-dipole and pole-pole configurations covering a profile distance of 200 m. This gives 343 for the total number of data of a Wenner array, 496 for a Schlumberger array, 787 for a Dipole – Dipole array, and 896 for a Pole – Pole array. For the RMT data, we set up 21 stations covering the same 200 m profile with both TM and TE modes and 13 very high frequencies (10^5 –100 Hz). The total number of RMT data is then 1092, about twice that of the DCR data. Two percent random noise was added to both data. The error bars for DCR and MT were then set at 2% of the absolute values of the responses.

We first inverted the DCR data individually. The starting model is obtained from averaging the apparent resistivity of both data sets resulting in the 90 Ω m half-space model. This required 4 or 5 iterations to fully converge to a misfit of 1 RMS. The inverted model from inverting the Schlumberger data is shown in Fig. 1b. The results from the other configurations look similar. The inverted model (Fig. 1b) shows that the two near surface anomalies can be recovered

very well but the two deeper anomalies cannot. This is expected since the maximum investigation depth of a DCR survey of any configurations with a profile length of 200 m is roughly 30 m, enough to recover the two near surface anomalies but not for the deeper anomalies. We next inverted the RMT data using both TM and TE modes from the same initial model. The inversion spent just 4 iterations to converge to 1 RMS. The inverted model is shown in Fig. 1c. In contrast to the DCR results (Fig. 1b), all four anomalies seem to have been recovered, particularly for the conductive anomalies but not clearly for the resistive structures. This can cause a misinterpretation if this data set was from a field survey. The same DCR and MT data sets were also inverted using other available software, i.e., RES2DINV (Loke and Barker, 1996), Boonchaisuk et al. (2008) and Vachiriatienchai and Siripunvaraporn (2013) for DCR inversion, and REBOCC (Siripunvaraporn and Egbert, 2000), NLCG (Rodi and Mackie, 2001), Siripunvaraporn and Egbert (2007) for RMT. Similar results were obtained as shown in Fig. 1b and c.

Next, the joint inversions were performed for the Schlumberger and RMT data (Fig. 1d), the Wenner and RMT data (Fig. 1e), the Dipole-Dipole and RMT data (Fig. 1f) and the Pole-Pole and RMT data (Fig. 1g). All joint inversions converge to 1 RMS in 4 or 5 iterations from the 90 Ω m half-space model. Results from joint inversions (Fig. 1d–g) show that all four anomalies are better recovered than those from the individual inversion. The DCR data obtained using any of the configuration helps to constrain the anomaly structures of the shallow parts while the MT data image the conductive structures and the deeper anomalies. Different initial models were also tested. We found that if the initial models are closed to the 90 Ω m half-space model used here, the inversion can converge within a similar number of iterations producing the inverted model similar to those in Fig. 1d–g. However, if the resistivity value used in the initial model is too “extreme”, the inversion can fail to converge to the target misfit leading to not acceptable inverted solutions.

It is not easy to recover the four anomalies with just the RMT inversion alone or the DCR inversion alone. In theory, to improve the recovery of the deeper anomalies for the DCR data, one needs to extend the electrode profile. In this example, after extending the length of the profile to 1000 m (5 times the original length), the inverted results are not very much different from Fig. 1d–g. For RMT data, adding more sites would theoretically help to improve the resolution of the resistive structure. However, in our example, doubling the number of sites would not help much in recovering the resistive structure. If it were a real field survey, extending the profile length of the DCR survey or increasing the number of MT sites would require extra work loads and higher operation cost that needs to be balanced out with the gain in information. Often, adding more sites or electrodes may be prohibited due to the difficult terrain or limitations of the equipment.

Rather than increasing the number of RMT sites or DCR electrodes, it is better to substitute them by another geophysical survey in order to gain more information, as demonstrated in Fig. 1d–g. In fact, to reduce the operation cost, it might not be necessary to conduct the full survey of DCR or RMT as in our example. A DCR survey over an ambiguous shallow resistive structure would help to boost the interpretation. Similarly, 5–10 RMT sites over an interesting area would be enough to help with enhancing the deeper anomalies beneath the shallow structures.

Since the number of data parameter N of the joint inversions increase to 1435, 1588, 1879 and 1988 for joint Wenner and RMT, Schlumberger and RMT, Dipole – Dipole and RMT, and Pole – Pole and RMT, respectively, it is expected that the calculation time and memory will increase by a factor of 1.5 – 2 compared with either of the individual inversions. This seems to be a price worth paying for the improvement in the quality of the results.

3.2. Joint AMT and MT with DCR data for correcting MT static shift

In this example, the model consists of two layers (Fig. 2a). The

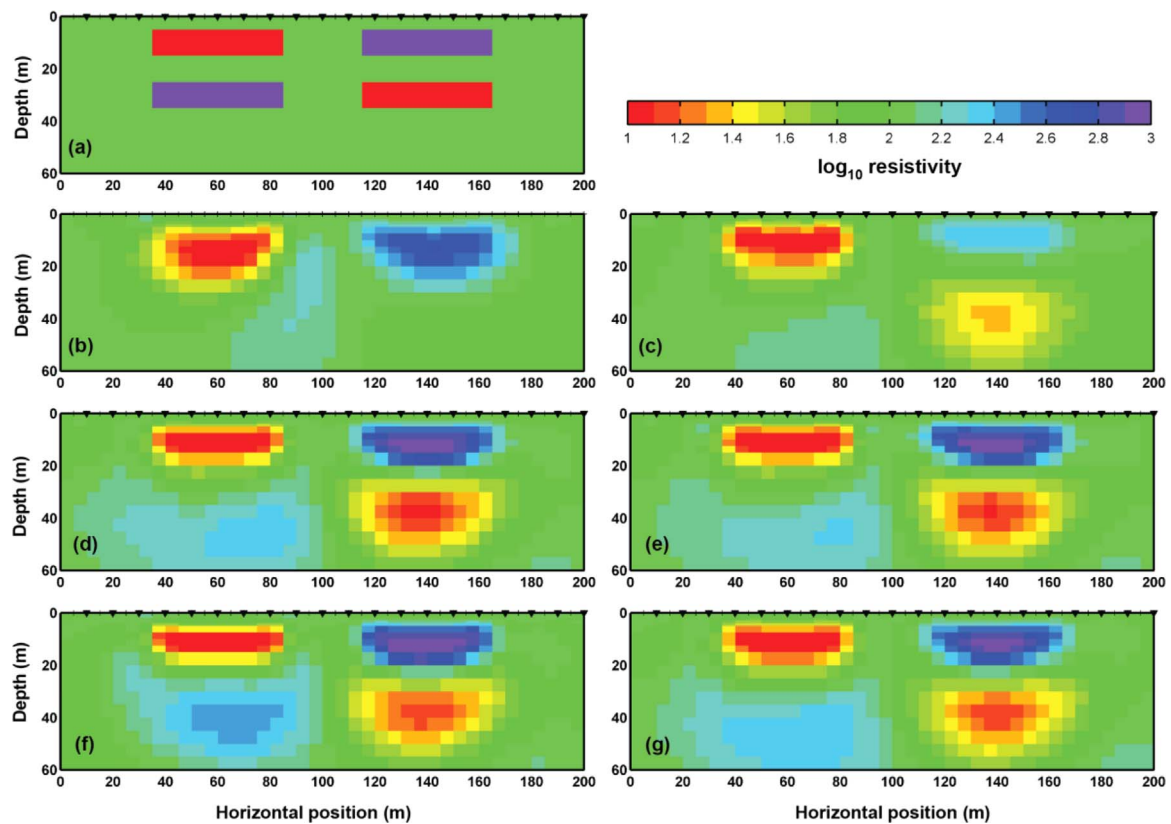


Fig. 1. (a) The synthetic model used to validate our developed code (after Kalscheuer et al. (2010)). Two resistive and conductive blocks are placed alternately inside the 100 Ω m half space. Black triangles are MT sites; thin vertical lines are electrode locations. Inverted models from inverting (b) Schlumberger data, (c) TM and TE of RMT data, (d) Schlumberger and RMT data, (e) Wenner and RMT data, (f) Dipole-Dipole and RMT data, and (g) Pole-Pole and RMT data.

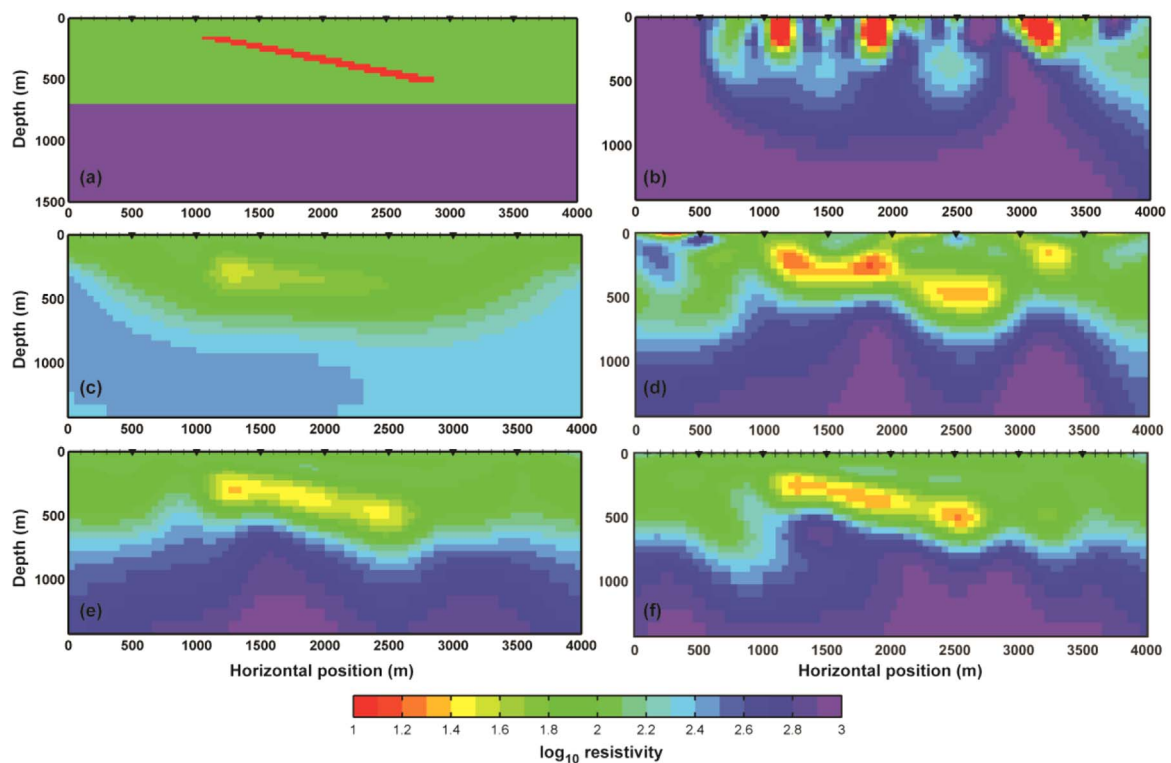


Fig. 2. (a) The synthetic model. Inverted models (a) from inverting the TM + TE data, (c) from inverting the Schlumberger data, (d) from inverting the TM + TE data with the error bars of TE apparent resistivity setting at 1000%, (e) from the joint inversion of the TM + TE phases and Schlumberger data where the error bars of TM and TE apparent resistivities setting at 1000%, and (f) from the joint inversion of corrected TM and TE data and Schlumberger data.

Table 1
The actual and recovered static shift factors used in numerical example.

x (km)		Actual static shift values	Recovered static shift values from the joint inversion of TE + TM + Schlumberger
0.5	TM	0.69	0.70
	TE	0.49	0.49
1	TM	−0.24	−0.25
	TE	0.35	0.34
1.5	TM	0.13	0.12
	TE	−0.27	−0.29
2	TM	−0.41	−0.42
	TE	0.68	0.66
2.5	TM	0.38	0.37
	TE	−0.70	−0.71
3	TM	−0.37	−0.37
	TE	−0.09	−0.09
3.5	TM	0.01	0.02
	TE	−0.18	−0.17

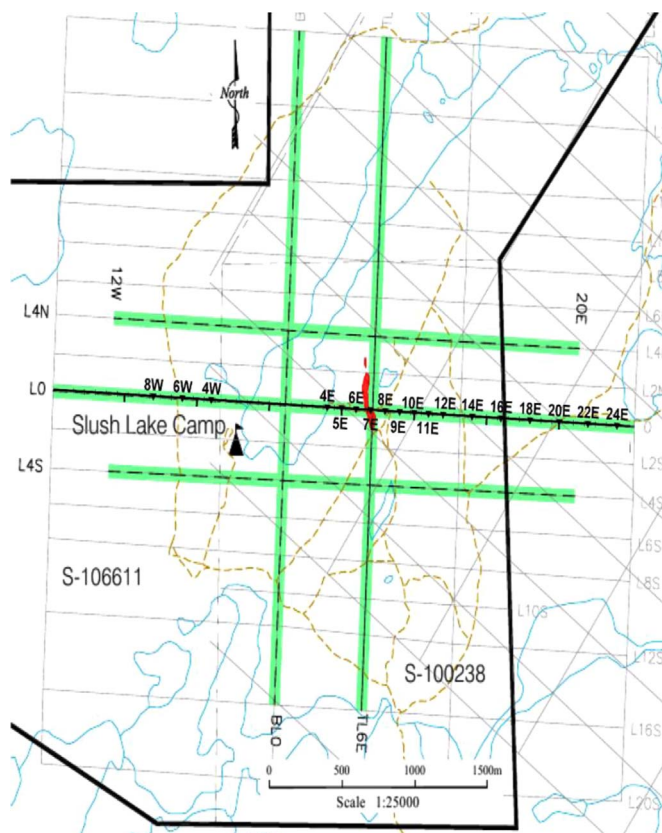


Fig. 3. The exploration plan at the CreeX Extension (CreeX) project (after Cameco Corporation). The established survey grid is used in both AMT and Pole – Pole surveys. We are authorized to access the data of the profile L0 which passes through the ore mining site. The dashed brown lines are the local road. The green lines highlight the survey profiles. Solid black lines delineate the vicinity of the Cree Extension (CreeX) project. (For interpretation of the references to color in this figure legend, the reader is referred to the web version of this article.)

100 Ω m surface layer is 700 m thick and lies above a resistive 1000 Ω m region. A 10 Ω m thin conductor with an average thickness of 50 m is buried in the first layer at an angle of 11° to the horizontal from a distance of 1000–3000 m and from a depth of 150–550 m (Fig. 2a).

The Schlumberger data is constructed based on 39 electrodes with multi-spacing surveys of 100 m, 200 m and 500 m to cover a profile distance of 3900 m with a maximum pseudo-depth level of $n = 27$ leading to 432 data points in total. The MT data consists of just 7 stations with a spacing of 500 m covering the same distance. For all sites, frequencies from 10^4 to 0.01 Hz (3 frequencies per decade) were used. For both TM and TE modes, the total number of MT data points is 560. To make the MT data more realistic, we randomly shifted $\log_{10}(\rho_a)$ of both TE and TM data with a number in the range of −1.5 to 1.5 (Table 1) to mimic the static normally occurring on the MT apparent resistivities. Static shifts can affect both the MT and DCR data. However, the causes for the static shifts for both data types can be different. For example, the nearby topography can cause the static shift for MT but not for DCR. Here, one necessary assumption we made is that the static shifts occurs on MT do not affect the DCR data.

We started by directly inverting the shifted MT data from the TM and TE modes. In all runs, the initial model is 150 Ω m half – space obtaining from the average of the apparent resistivity of both data sets. As expected, if the shifts of the apparent resistivities are not corrected, the inversion has difficulty converging to the solution. The inverted model (Fig. 2b) produces a RMS misfit of 54, i.e., does not fit the observed data well. Inverting the MT data with a static shift therefore fails in this case. In contrast, as the DCR method is not affected by the static shift, inversion of just the Schlumberger data can converge to 1 RMS and can recover the shallow structures (Fig. 2c) better than the MT inversion (Fig. 2b) but still cannot clearly image the tilted structure.

To avoid the MT static shift problem, one technique is to set the error bars for the TE apparent resistivities at high levels (e.g., 1000%) while keeping TM apparent resistivities and phases at the normal level, and then performing the inversion. The inverted model at the 11th iteration with 4.4 RMS is shown in Fig. 2d. With this technique, the inverted model looks much better than that of Fig. 2b. Since the shift is still affecting the TM apparent resistivities, it is difficult for the inversion to converge to the desired misfit of 1 RMS. Another way is to invert just the phase data (e.g., Ogawa, 2002; Padilha et al., 2002; Parker and Booker, 1996; Wu et al., 1993) and then estimated the shift values either manually or using a statistical approach provided in the 2-D MT inversion codes (e.g., REBOCC of Siripunvaraporn and Egbert (2000), NLCC of Rodi and Mackie (2001)). The data is then corrected and re-invert again. This technique often works well, but when the data is noisy, there is considerable uncertainty in the shift factors obtained (e.g., Spitzer, 2001; Tripaldi et al., 2010).

Since the MT apparent resistivities are affected by the distortion and noise, the DCR apparent resistivities which are less affected by noise can be used as a replacement for the MT apparent resistivities when performing a joint inversion. To estimate the static shift factor with the joint inversion, we first set the error bars of the MT apparent resistivity at a very high level (e.g., 1000%) in order to eliminate its influence to the inversion. The error bars of the MT phase and DCR apparent resistivity are still at the original level which is 1% in this example. The joint inversion spent 4 iterations to converge to 1 RMS to produce the inverted model shown in Fig. 2e. The estimated static shift factor of each station is derived based on the difference between the calculated and observed MT apparent resistivities plotted in a \log_{10} scale and is listed in Table 1. The joint inversion can recover the tilted conductor better than any of the individual inversion. In addition, the static shift factors for the TM and TE apparent resistivities match remarkably well with the actual factors (Table 1). The obtained shift factors can be used to correct the MT apparent resistivities, and then re-invert with just MT inversion or joint inversion. Here, the joint MT and DCR inversion to the corrected MT and DCR data requires about 8 iterations to converge to 1 RMS to produce an inverted model shown in Fig. 2f that is much closer to the original model (Fig. 2a). Note that in the case that the distortion from the same source occurs on both data types, the results obtained from the joint inversion will differ from our example.

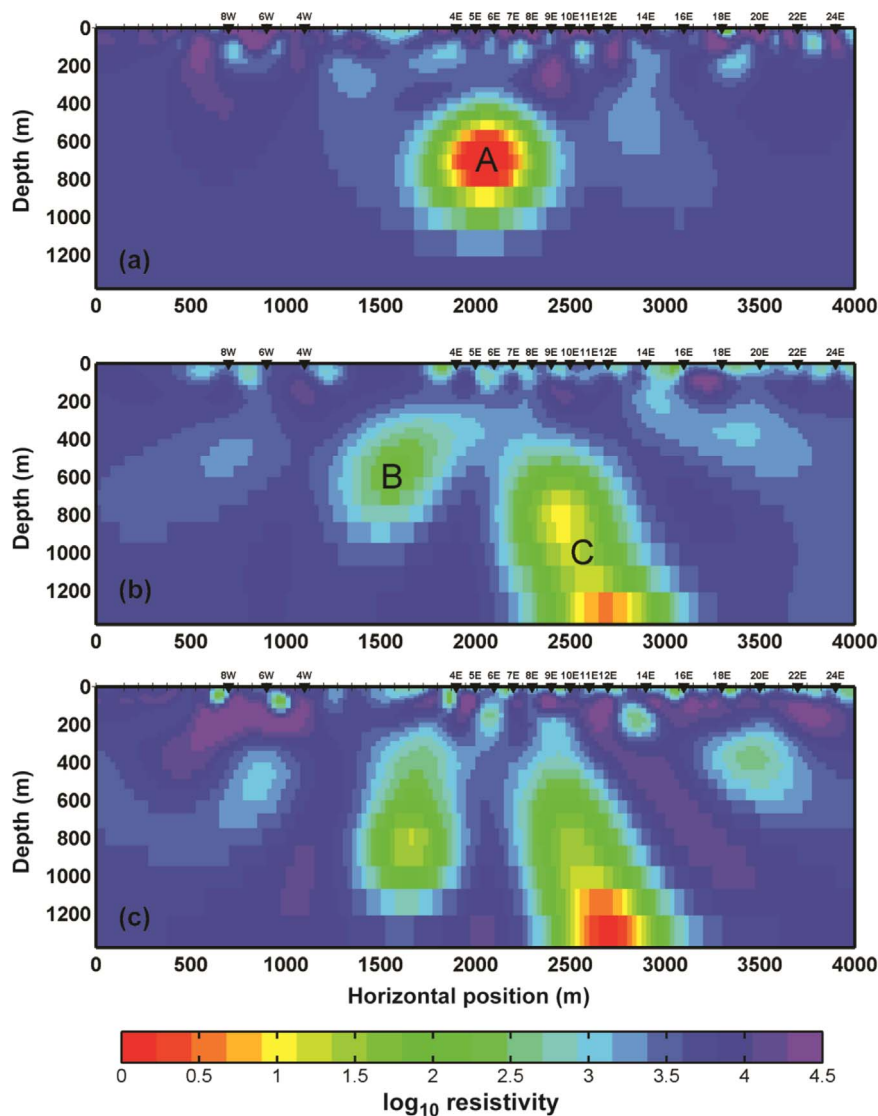


Fig. 4. Inverted models from (a) Pole – Pole inversion, (b) TM + TE inversion with static correction and (c) Pole – Pole + TM + TE with static correction.

3.3. Field example: CreeX project

The CreeX project was conducted in the southeastern portion of the Athabasca Basin, Saskatchewan, Canada which holds the world's largest uranium deposits. Many geophysical investigations, including the electric and electromagnetic surveys, have been performed in this area. The goal of the surveys in this project was to map the low resistivity zone of graphite which indicates the unconformity-type uranium deposits. In this section, we use the AMT and pole-pole DCR data acquired in this area to test our joint inversion.

The AMT data were recorded in 2001–2002 using GEOTRAN-MT equipment designed and constructed by EMPulse Geophysics Ltd. There are 18 AMT stations located along the L0 profile at the established grid points labeled as 8W, 6W, 4W, 4E, 5E, 6E, 7E, 8E, 9E, 10E, 11E, 12E, 14E, 16E, 18E, 20E, 22E and 24E (Fig. 3) covering a distance of 3200 m with a station spacing of 100–200 m. The denser spacing from station 4E to 12E is because they are in the locations associated with the buried target. A large gap between stations 4W to 4E is due to Slush Lake which is inaccessible during the summer data acquisition. The data is from 55 frequencies in the range 8 Hz–32 kHz. However, here we only selected 28 frequencies to use for our inversions leading to 2016 MT data points. Since phases of the MT sites at 10E and 11E and 20E and 22E are the same but $\log_{10}(\rho_a)$ of these stations

differ by constant values, this demonstrates that they are affected by the static distortion. For the DCR data, the Pole – Pole configuration is selected because of its greater investigation depth than other DCR arrays. The electrodes are set along the L0 profile from 15W to 24E with 75 m spacing giving a total profile length of 3900 m. The data was acquired up to 12 pseudo-depth levels as beyond this level the data quality is mostly bad. The extreme and bad data points were eliminated before applying the inversions leading to a total of 714 DCR data points. The observed data of (a) TE, (b) TM and (c) Pole – Pole are shown in Fig. 5, respectively, along with their calculated responses from the joint inversion case only.

To perform the joint and individual inversions, a 6000 Ω m homogeneous half-space was derived from prior geological information and the MT and DCR apparent resistivities, and was discretized with an 180×48 mesh. We use this as both the starting and reference model. The number of the model parameters, M , is 8640 which is much larger than the number of data points from both data sets.

We started with the DCR inversion alone by setting the minimum error bars for the Pole – Pole data at 5%. The inversion needs around 5 iterations to converge from around 20 RMS to 3.33 RMS indicating that the relative difference between the calculated responses and the observed data is within 15%. The large error for this case is due to the poor quality of the data at some points and also the complex geology of

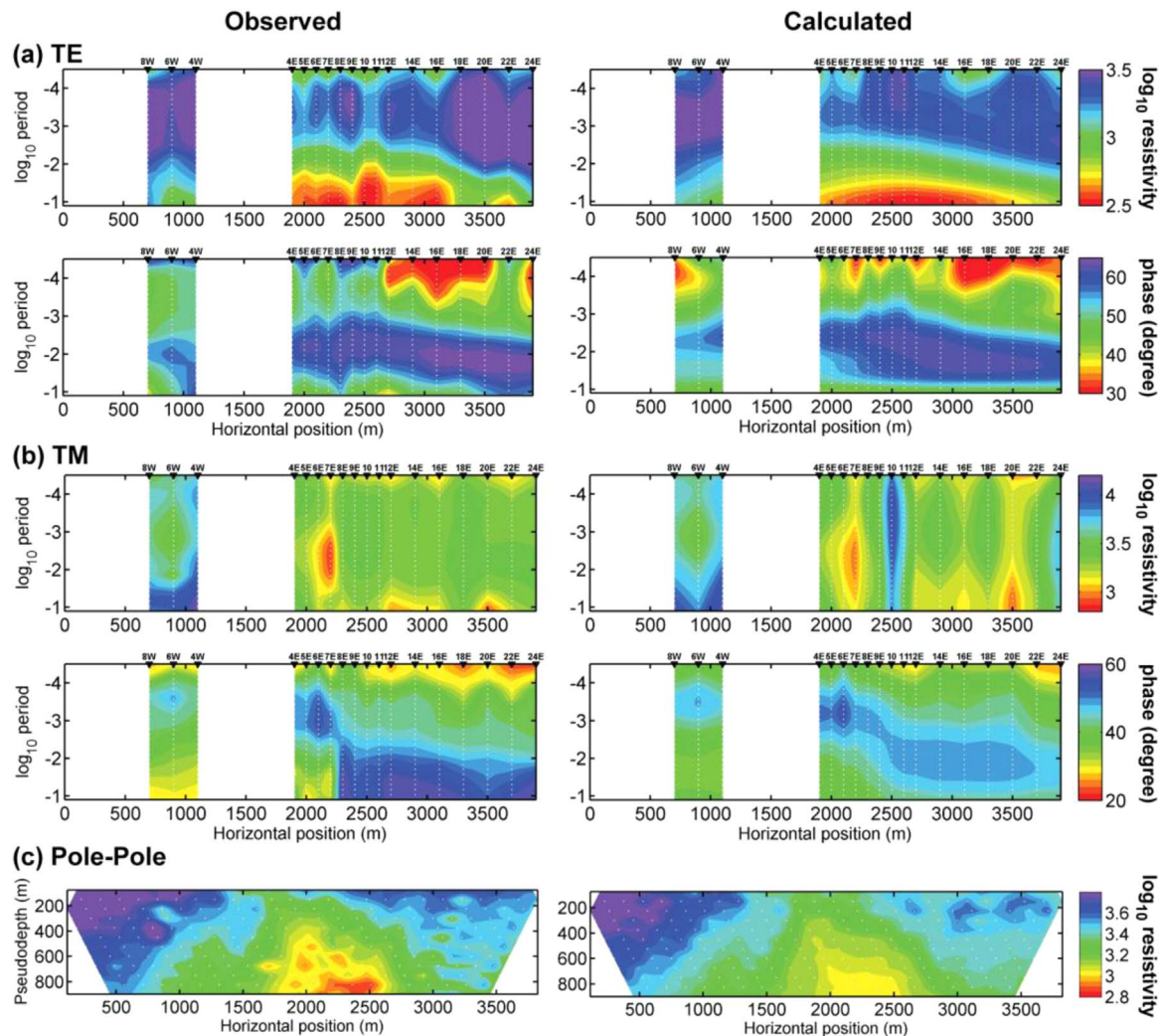


Fig. 5. Observed data and their calculated responses from the joint inversion case (Fig. 4c). (a) Observed and calculated apparent resistivities (top) and phases (bottom) for TE mode, and (b) for TM mode. (c) Observe and calculated apparent resistivities for Pole – Pole survey.

the area. The inverted resistivity model (Fig. 4a) moderately recovers the top of the graphitic faults (marked as A in Fig. 4a) at around $x=1800-2300$ m (beneath 4E–8E) and the lower resistivity sandstone alteration layer on top of the resistive basement.

Next we performed the joint TM and TE inversion by setting the minimum error bars for both apparent resistivities and phases at 5% except at some selected sites (at 10E, 11E, 20E and 22E) where the minimum error bars for the apparent resistivities were set at 1000% to account for the static shifts. The inversion needs 7 iterations to converge to around the minimum of 3.8 RMS. The calculated responses of TM, TE and Pole – Pole can be seen in Fig. 5. The inverted model shows two conductive zones marked as B and C in Fig. 4b. A lower resistivity anomaly (B anomaly) is detected near the surface around $x=1300-1800$ m covering the zone of no MT station coverage which is west of 4E and east of 4W. The second zone is the highly conductive target (C anomaly) from $x=2300-3000$ m (beneath station 7E – 14E) and extends to greater depth. The inverted result from MT (Fig. 4b) with two conductors seems to be in contradiction with the inverted result from the Pole – Pole data (Fig. 4a) showing just one conductor. Interpreting the results from an individual inversion might lead to different conclusions. For example, if there is no MT profile to constrain the interpretation from the DCR profile (Fig. 4a), one might interpret the conductor A as located in the middle of conductor B and C. Not only conductor A is located at different place, its conductivity might be too high for the graphite and could lead to different interpretation. Similarly, if there is no DCR profile to constrain the MT data (Fig. 4b), one might interpret

the conductor B as an artifact from the inversion as there are no MT stations above it. These ambiguities from the individual survey can be overcome with the joint survey.

The joint inversion of Pole – Pole and MT data were then performed next in order to constrain the inversion results from the individual survey and resolve their uncertainties. As with the MT inversion, the minimum error bars of the apparent resistivities for the four sites are set at 1000% to cope with static shift, while others are kept at 5%. The joint inversion needs 8 iterations to reduce the RMS from around 17 to 3.4 to produce the inverted model (Fig. 4c). The joint inversion confirms the existence of the two conductors, as with the results from the MT inversion, but their positions and depths are slightly different. In fact, our joint inversion result (Fig. 4c) shows that the results from the DCR inversion (Fig. 4a) and from the MT inversion (Fig. 4b) support each other. The inverted result of the Pole – Pole data has just one conductor at the center (Fig. 4a) because the two conductors are too deep. The responses from the two conductors are then superimposed so that the inversion cannot distinguish them. For the MT result (Fig. 4b), the uncertainty about the existence of conductor B is clear with the joint inversion (Fig. 4c). This example demonstrates that the joint inversion can eliminate the ambiguities arising from both data sets.

To confirm the results of the DCR inversion, the inverted model of Fig. 4c is simplified to give a synthetic model (Fig. 6a) with just two conductors, similar to the B and C conductors in Fig. 4c, in a $6000 \Omega \text{ m}$

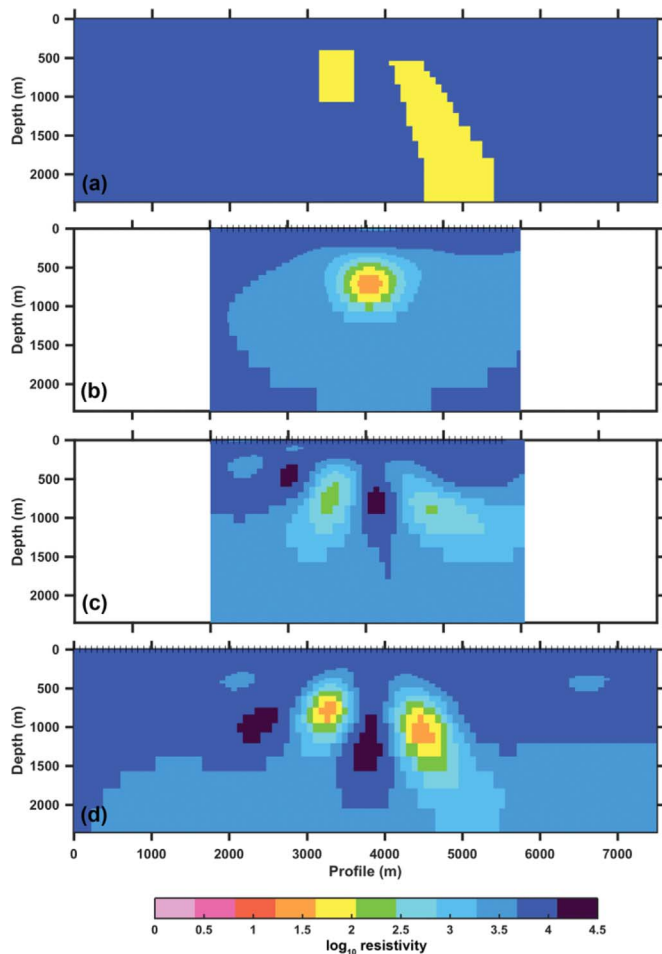


Fig. 6. (a) Synthetic model, a simplified version from the inverted model in Fig. 4c, used for the DCR inversion to validate the results from the field data. (b) The inverted model obtained from the DCR data generated from (a) with just 12 pseudo-depth level from a 4 km profile (2000–6000 m). (c) Similar to (b) but with the maximum pseudo-depth of 51 levels. (d) The inverted model obtained from the DCR data generated from (a) with 100 pseudo-depth level from a 8 km profile.

half-space. The DCR data was generated with the Pole – Pole configuration, similar to that used in real experiment, with just 12 pseudo-depth levels (the same number of levels as in the field data) and the maximum pseudo-depth levels of 51. The DCR inversion alone with just the 12 pseudo-depths produced an inverted model showing just one conductor (Fig. 6b), confirming the result of Fig. 4a. When inverting using all of the data up to 51 pseudo-depths, the two conductors are recovered separately (Fig. 6c), but not as clearly as those of Fig. 4b and c. To better distinguish the two conductors with just the DCR survey, our synthetic tests demonstrated that we need to extend the profile to at least 8 km in length to increase the number of pseudo-depth levels to 100 levels. Fig. 6d shows that the two conductors are clearly differentiated from each other with better resolution than the inverted result shown in Fig. 6c. Although the synthetic experiment showed that it is possible to recover both conductors by using a longer profile, extending the profile length in real field experiments may be complicated. As it will result in higher costs and survey time and may or may not obtain good data. It is therefore better to do a joint survey with MT in order to obtain information about the deeper structures.

4. WSJointInv2D-MT-DCR code and how to

Our joint 2-D inversion program (WSJointInv2D-MT-DCR) for MT and DCR can be freely accessed for academic (non-profit) uses (for

commercial uses, please contact the authors) at <http://geophysics.sc.mahidol.ac.th/software/WSJointInv2D-MT-DCR> website. The code is written with Fortran 95. Besides the source codes, there is a comprehensive User Manual within the zip file. Since we have provided the source code, the program should work on most systems (Unix, Linux, Mac, Window) with Fortran compilers. Updates and bug fixed will be announced in our website.

To run the code, the startup and input files are necessary. Startup is the main file to direct the code to acquire the DCR and MT data from provided directories, to receive the location for printing out the output files, and to operate the inversion according to the instructions provided by the users whether just running the forward modeling routine to produce the responses from the synthetic model, or just invert the MT data alone, or just invert the DCR data alone, or conduct a joint inversion. The input and output file formats are clearly written in the provided User Manual. However, users who have familiar with our earlier released codes of REBOCC (Siripunvaraporn and Egbert, 2000) and WSINV3DMT (Siripunvaraporn et al., 2005; Siripunvaraporn and Egbert, 2009) will quickly understand as we used similar formats.

5. Conclusions

We have developed an efficient joint inversion program (WSJointInv2D-MT-DCR) with Fortran 95 for the MT and DC resistivity methods based on the data space Occam's inversion. Our joint inversion program has flexibility. It can be used to invert just the MT data or the DC Resistivity data, or invert both data sets simultaneously. Our experiments based on the synthetic and real data show that there are many benefits of performing the joint inversion over the individual MT or DCR inversions. Performing the DC resistivity survey alone may be better in probing the very near surface structures, but going deeper would be difficult. Adding some MT stations along the DCR profile would help increase the depth of investigation of the survey. In the opposite, performing the MT survey alone may be better in recovering structures at great depth, but lateral resolution between sites is limited. This can be overcome by adding the DCR survey between MT stations to increase the shallow lateral resolutions between MT sites. Often, MT data can be contaminated with static shifts and noise. By performing the joint inversion using the DCR apparent resistivity and MT phases, the static shift factors can be correctly estimated under the condition that both data types do not suffer the same source of data distortion. The joint inversion can then be conducted again using the corrected MT data and DCR data yielding better results. In addition, our real field data demonstrated that the joint inversion can help eliminate the ambiguity arising from the individual inversions due to the inadequate coverage or the loss of resolving power. With the availability of our joint inversion software, we hope that number of joint DCR and MT surveys will increase in the future.

Acknowledgements

This research has been supported by the Thailand Research Fund (TRF: RSA5780010) and Mahidol University. The author would like to thank the development and promotion of science and technology talents project (DPST) for the research funds awarded to Puwis Amatyakul. We thank David Goldax and Cameco Corporation and their Joint Venture partners on the Cree Extension project, Areva Canada Resources and JCU Canada Ltd., for the right to publish the results derived from the geophysical datasets. We also thank to Dr. Michael Allen for correcting the English.

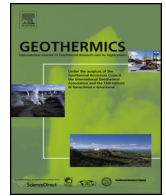
References

- Amatyakul, P., Rung-Arunwan, T., Siripunvaraporn, W., 2015. A pilot magnetotelluric survey for geothermal exploration in Mae Chan region, northern Thailand.

- Geothermics 55, 31–38.
- Amatyakul, P., Boonchaisuk, S., Rung-Arunwan, T., Vachiriatienchai, C., Wood, S.H., Pirarai, K., Fuangswasdi, A., Siripunvaraporn, W., 2016. Exploring the shallow geothermal fluid reservoir of Fang geothermal system, Thailand via a 3-D magnetotelluric survey. *Geothermics* 64, 516–526.
- Bastani, M.F., Hubert, J., Kalscheuer, T., Pedersen, L., Godio, A., Bernard, J., 2012. 2D joint inversion of RMT and ERT data versus individual 3D inversion of full tensor RMT data: an example from Trecate site in Italy. *Geophysics* 77, WB233–WB243.
- Boonchaisuk, S., Siripunvaraporn, W., Ogawa, Y., 2013. Evidence for middle Triassic to Miocene dual subduction zones beneath the Shan–Thai terrane, western Thailand from magnetotelluric data. *Gondwana Res.* 23, 1607–1616.
- Boonchaisuk, S., Vachiriatienchai, C., Siripunvaraporn, W., 2008. Two-dimensional direct current (DC) resistivity inversion: data space Occam's approach. *Phys. Earth Planet. Inter.* 168, 204–211.
- Buselli, G., Lu, K., 2001. Groundwater contamination monitoring with multichannel electrical and electromagnetic methods. *J. Appl. Geophys.* 48, 11–23.
- Candansayar, M., Tezkan, B., 2008. Two-dimensional joint inversion of radiomagnetotelluric and direct current resistivity data. *Geophys. Prospect.* 56, 737–749.
- Constable, S., Parker, R., Constable, C., 1987. Occam's inversion: a practical algorithm for generating smooth models from electromagnetic sounding data. *Geophysics* 52, 289–300.
- deGroot-Hedlin, C., Constable, S., 1990. Occam's inversion to generate smooth, two-dimensional models from magnetotelluric data. *Geophysics* 55, 1613–1624.
- Diaferia, I., Lodo, M., Schiavone, D., Siniscalchi, A., 2008. Shallow to intermediate resistivity features of the Colfiorito Fault System inferred by DC and MT survey. *Ann. Geophys.* 51, 443–450.
- Farquharson, C.G., Craven, A.J., 2009. Three-dimensional inversion of magnetotelluric data for mineral exploration: an example from the McArthur River uranium deposit, Saskatchewan, Canada. *J. Appl. Geophys.* 68, 450–458.
- Kalscheuer, T., Juanatey, M., Meqbel, N., Pedersen, L., 2010. Non-linear model error and resolution properties from two-dimensional single and joint inversions of direct current resistivity and radiomagnetotelluric data. *Geophys. J. Int.* 182, 1174–1188.
- Kalscheuer, T., Bastani, M., Donohue, S., Persson, A., Aspmo, A., Reiser, F., Wen, Z., 2013. Delineation of a quick clay zone at Smørggrav, Norway, with electromagnetic methods under geotechnical constraints. *J. Appl. Geophys.* 92, 121–136.
- Linde, N., Pedersen, L., 2004. Characterization of a fractured granite using radio magnetotelluric (RMT) data. *Geophysics* 69, 1155–1165.
- Loke, M.H., Barker, R., 1996. Rapid least-squares inversion of apparent resistivity pseudosections by a quasi-Newton method. *Geophys. Prospect.* 44, 131–152.
- Meju, M., Fontes, S., Oliveira, M., Lima, J., Ulugergerli, E., Carrasquilla, A., 1999. Regional aquifer mapping using combined VES-TEM-AMT/EMAP methods in the semiarid eastern margin of Parnaíba basin, Brazil. *Geophysics* 64, 337–356.
- Monteiro Santos, F., Andrade Afonso, A., Dupis, A., 2007. 2D joint inversion of DC and scalar audio- magnetotelluric data in the evaluation of low enthalpy geothermal fields. *J. Geophys. Eng.* 4, 53–62.
- Monteiro Santos, F., Dupis, A., Andrade Afonso, A., Mendes Victor, L., 1997. 1D joint inversion of AMT and resistivity data acquired over a graben. *J. Appl. Geophys.* 38, 115–129.
- Monteiro Santos, F., Sultan, S.B., 2008. On the 3-D inversion of vertical electrical soundings: application to the south Ismailia area Cairo desert road, Cairo, Egypt. *J. Appl. Geophys.* 65, 97–110.
- Ogawa, Y., 2002. On two-dimensional modeling of magnetotelluric field data. *Surv. Geophys.* 23, 251–272.
- Padilha, A., Vitorello, I., Brito, P., 2002. Magnetotelluric soundings across the Taubate basin, southeast Brazil. *Earth Planets Space* 54, 617–627.
- Parker, R.L., Booker, J.R., 1996. Optimal one-dimensional inversion and bounding of magnetotelluric apparent resistivity and phase measurements. *Phys. Earth Planet. Inter.* 98, 269–282.
- Rodi, W.L., 1976. A technique for improving the accuracy of finite element solutions for magnetotelluric data. *Geophys. J. R. Astr. Soc.* 44, 483–506.
- Rodi, W., Mackie, R.L., 2001. Nonlinear conjugate gradients algorithm for 2-D magnetotelluric inversion. *Geophysics* 66, 174–187.
- Sasaki, Y., 1989. Two-dimensional joint inversion of magnetotelluric and dipole-dipole resistivity data. *Geophysics* 54, 254–262.
- Satitpittakul, A., Vachiriatienchai, C., Siripunvaraporn, W., 2013. Factors influencing cavity detection in Karst terrain on two-dimensional (2-D) direct current (DC) resistivity survey: a case study from the western part of Thailand. *Eng. Geol.* 152, 162–171.
- Seher, T., Tezkan, B., 2007. Radiomagnetotelluric and direct current resistivity measurements for the characterization of conducting soils. *J. Appl. Geophys.* 63, 35–45.
- Shan, C., Bastani, M., Malehmir, A., Persson, L., Engdahl, M., 2014. Integrated 2D modeling and interpretation of geophysical and geotechnical data to delineate quick clays at a landslide site in southwest Sweden. *Geophysics* 79, EN61–EN75.
- Sinharay, R., Srivastava, S., Bhattacharya, B., 2010. Audiomagnetotelluric studies to trace the hydrological system of thermal fluid flow of Bakreswar hot spring, eastern India: a case history. *Geophysics* 75, 187–195.
- Siripunvaraporn, W., 2012. Three-dimensional magnetotelluric inversion: an introductory guide for developers and users. *Surv. Geophys.* 33, 5–27.
- Siripunvaraporn, W., Egbert, G., 2000. An efficient data-subspace inversion method for 2-D magnetotelluric data. *Geophysics* 65, 791–803.
- Siripunvaraporn, W., Egbert, G., 2007. Data space conjugate gradient inversion for 2-D magnetotelluric data. *Geophys. J. Int.* 170, 986–994.
- Siripunvaraporn, W., Egbert, G., 2009. WSINV3DMT: vertical magnetic field transfer function inversion and parallel implementation. *Phys. Earth Planet. Inter.* 173, 317–329.
- Siripunvaraporn, W., Egbert, G., Uyeshima, M., 2005. Interpretation of two-dimensional magnetotelluric profile data with three-dimensional inversion: synthetic examples. *Geophys. J. Int.* 160, 804–814.
- Siripunvaraporn, W., Sarakorn, W., 2011. An efficient data space conjugate gradient Occam's method for three-dimensional magnetotelluric inversion. *Geophys. J. Int.* 186, 567–579.
- Spitzer, K., 2001. Magnetotelluric static shift and direct current sensitivity. *Geophys. J. Int.* 144, 289–299.
- Tezkan, B., Georgescu, P., Fauzi, U., 2005. A radiomagnetotelluric survey on an oil-contaminated area near the Brazi refinery, Romania. *Geophys. Prospect.* 53, 311–323.
- Tezkan, B., Goldman, M., Greinwald, S., Hrdt, A., Mller, I., Neubauer, F., Zacher, G., 1996. A joint application of radiomagnetotellurics and transient electromagnetics to the investigation of a waste deposit in Cologne (Germany). *J. Appl. Geophys.* 34, 199–212.
- Tezkan, B., Saraev, A., 2008. A new broadband radiomagnetotelluric instrument: applications to near surface investigations. *Surv. Geophys.* 6, 245–252.
- Tripaldi, S., Siniscalchi, A., Spitzer, K., 2010. A method to determine the magnetotelluric static shift from dc resistivity measurements in practice. *Geophysics* 75, F23–F32.
- Tullen, P.B., Turberg, P., Parriaux, A., 2006. Radiomagnetotelluric mapping, groundwater numerical modelling and 18-oxygen isotopic data as combined tools to determine the hydrogeological system of a landslide prone area. *Eng. Geol.* 87, 195–204.
- Tuncer, V., Unsworth, M.J., Siripunvaraporn, W., Craven, J.A., 2006. Exploration for unconformity-type uranium deposits with audiomagnetotelluric data: a case study from the McArthur River mine, Saskatchewan, Canada. *Geophysics* 71, B201–B209.
- Vachiriatienchai, C., Boonchaisuk, S., Siripunvaraporn, W., 2010. A hybrid finite difference–finite element method to incorporate topography for 2D direct current (DC) resistivity modeling. *Phys. Earth Planet. Inter.* 183, 426–434.
- Vachiriatienchai, C., Siripunvaraporn, W., 2013. An efficient inversion for two-dimensional direct current resistivity surveys based on the hybrid finite difference - finite element method. *Phys. Earth Planet. Inter.* 215, 1–11.
- Wang, L., Hitchman, A., Ogawa, Y., Siripunvaraporn, W., Ichiki, M., Fuji-ta, K., 2014. A 3-D conductivity model of the Australian continent using observatory and magnetometer array data. *Geophys. J. Int.* 198, 1143–1158.
- Wilson, S., Ingham, M., McConchie, J., 2006. The applicability of earth resistivity methods for saline interface definition. *J. Hydrol.* 316, 301–312.
- Wu, N., Booker, J.R., Smith, J.T., 1993. Rapid two-dimensional inversion of COPROD2 data. *J. Geomag. Geoelectr.* 45, 1073–1087.
- Yogeshwar, P., Tezkan, B., Israil, M., Candansayar, M., 2012. Groundwater contamination in the Roorkee area, India: 2D joint inversion of radiomagnetotelluric and direct current resistivity data. *J. Appl. Geophys.* 76, 127–135.

ภาคผนวก ข. Reprint

- Puwis Amatyakul, Songkhun Boonchaisuk, Tawat Rung-Arunwan, Chatchai Vachiratienchai, Spencer H. Wood, Kriangsak Pirarai, Aranya Fuangswasdi, and **Weerachai Siripunvaraporn**, 2016, Exploring the shallow geothermal fluid reservoir of Fang geothermal system, Thailand via a 3-D magnetotelluric survey, Geothermics, 64, 516 – 526. (IF2015 = 2.323)



Exploring the shallow geothermal fluid reservoir of Fang geothermal system, Thailand via a 3-D magnetotelluric survey

Puwis Amatyakul^a, Songkhun Boonchaisuk^b, Tawat Rung-Arunwan^c,
Chatchai Vachirastienchai^c, Spencer H. Wood^d, Kriangsak Pirarai^e, Aranya Fuangswasdi^e,
Weerachai Siripunvaraporn^{a,f,*}

^a Department of Physics, Faculty of Science, Mahidol University, 272 Rama 6 Road, Rachatawee, Bangkok, 10400, Thailand

^b Geoscience Program, Mahidol University, Kanchanaburi Campus, Saiyok, Kanchanaburi, Thailand

^c Curl-E Geophysics Co., Ltd., 85/87 Nantawan Village, Uttayan-Aksa Road, Salaya, Phutthamonthon, Nakornpathom, 73170, Thailand

^d Department of Geosciences, Boise State University, Boise, ID, 83701, USA

^e Department of Groundwater Resources, Ministry of Natural Resources and Environment, 26/83 Soi Ngamwongwan 54, Ngamwongwan Road, Ladyao, Chatuchak, Bangkok, 10900, Thailand

^f ThEP Center, Commission on Higher Education, 328, Si Ayutthaya Road, Rachatawee, Bangkok, Thailand

ARTICLE INFO

Article history:

Received 23 December 2015

Received in revised form 7 July 2016

Accepted 4 August 2016

Keywords:

Thailand

Fang hot spring

Magnetotelluric

Geothermal

ABSTRACT

After early exploration during the 1980s and 1990s, the 0.3 MW Fang geothermal power plant was built as a demonstration to supply electricity to the local community. The shallow well (100 m) drilling program produced about 22 l/s of 125 °C water, and two wells to 500 m produced about 10 l/s. Due to the lack of detailed information on the geothermal system, the plan to expand to a larger power plant was halted to avoid the drilling missing the hot fluid. The plan was resumed in the last ten years starting with the magnetotelluric (MT) survey. Thirty three MT sites were deployed on the southern part of the Fang geothermal area. A remote site was installed about 600 km south of the study area for better data quality. After data processing, the data was inverted with WSINV3DMT to produce the 3-D resistivity model which clearly matches the near-surface geology and is also in agreement with the conceptual geology of the Fang geothermal system. The high resistivity zone is interpreted as the crystalline granitic rock, while the intermediate resistivity zone is associated with the Fang sedimentary basin. The resistivity contrast between the higher and lower resistivities helps reveal the orientations of the major Mae Chan Fault (MCF) and the two local faults of the area. The two main conductors of interests, C1 and C2, are directly linked to the hot fluid found at the surface. C1 is shallow (<50 m), and found only beneath the Fang hot spring, and so it is interpreted as the fracture reservoir. C2, which was not discovered in previous studies, extends from near the surface to a depth of 500 m, and at a depth of 200 m, it is about 1 km wide. It is about 1 km south of the Fang hot spring where the warm water was found to have seeped to the surface through the MCF. Two possible interpretations are proposed for the C2 conductor. The first is that there is an impermeable clay zone trapping a relatively high resistivity geothermal fluid reservoir beneath, like the caprock of a magmatic geothermal play type. This would require a deeper well to extract the hot fluid. As with the C1 conductor, the other interpretation is that the C2 conductor is a fracture geothermal reservoir where hot fluid from the deep resides within the pores of the sedimentary rock and fractures of the altered granite. This would require a shallower well. Both interpretations suggest that the C2 anomaly is of value. Since it has never been explored, a drilling over the C2 anomaly is recommended to probe its characteristic and also to extract more hot fluid for the future expansion of the geothermal power plant.

© 2016 Elsevier Ltd. All rights reserved.

1. Introduction

The Fang geothermal area is about 140 km north of Chiang Mai city (Fig. 1). Evaluation of the area began in 1977 when detailed geological and resistivity surveys were conducted in the Fang hot springs area (rectangle in Fig. 1 and red dot in Fig. 2)

* Corresponding author at: Department of Physics, Faculty of Science, Mahidol University, 272 Rama 6 Road, Rachatawee, Bangkok, 10400, Thailand.

E-mail addresses: wsiripun@gmail.com, weerachai.sir@mahidol.ac.th (W. Siripunvaraporn).

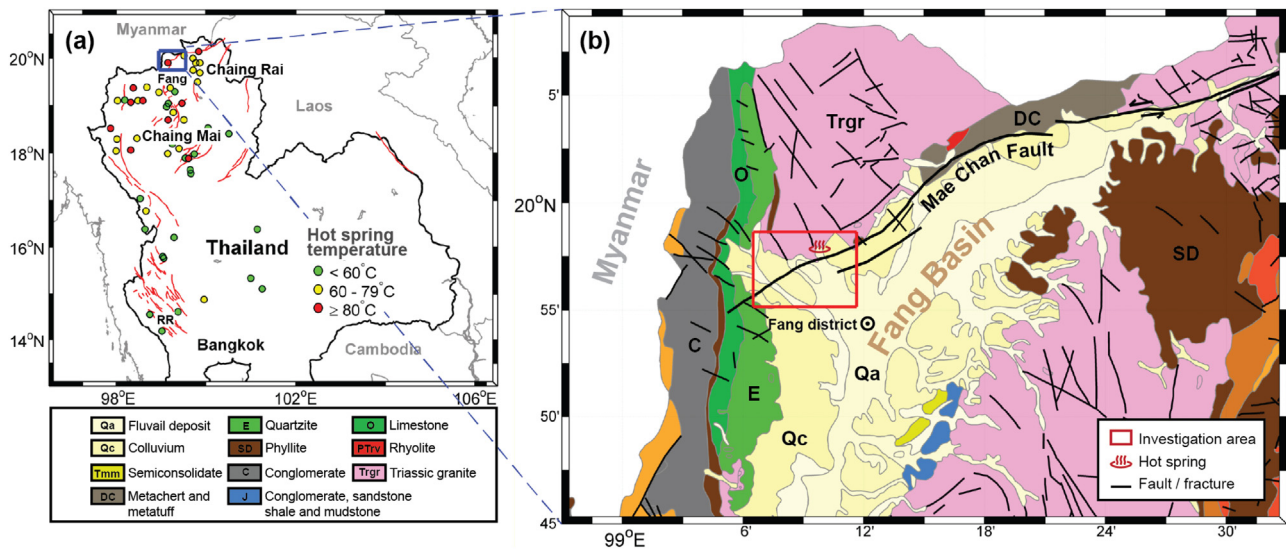


Fig. 1. (a) Hot springs in northern and western Thailand are marked as circles with different colors for different temperature ranges. The regional geology of the blue rectangle is shown in (b) in which the survey and study area of this paper is marked with a red rectangle. (For interpretation of the references to colour in this figure legend, the reader is referred to the web version of this article.)

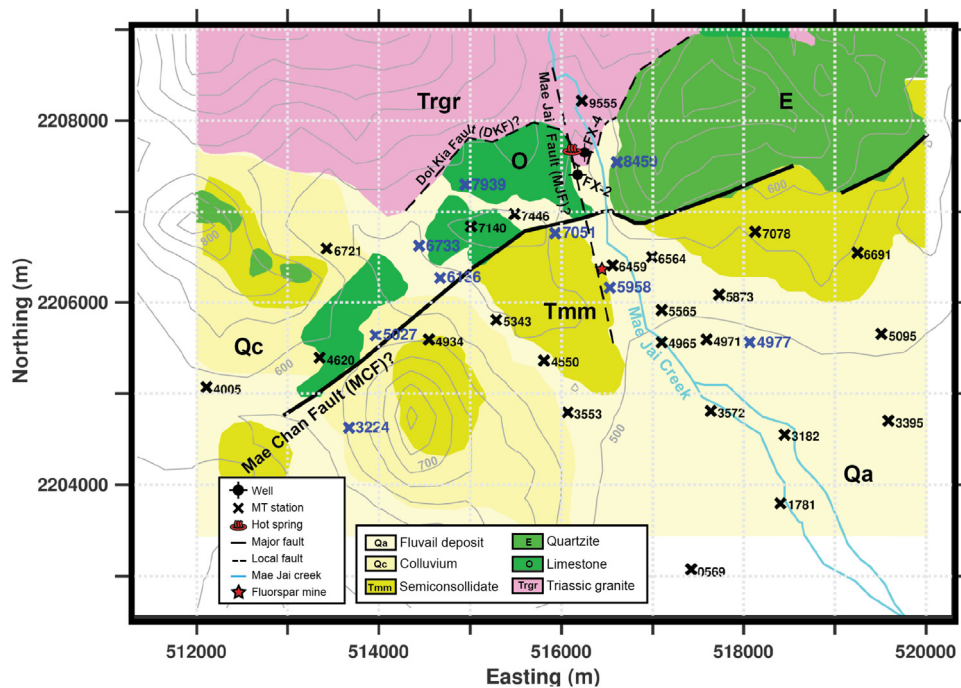


Fig. 2. Detailed geological rock units with major and local faults and topography of the Fang hot spring study area. The crosses indicate the MT sites. The observed data at the blue stations are shown in Figs. 4 and 5. DKF is the Doi Kia Fault; MJF is the Mae Jai Fault; MCF is the Mae Chan Fault drawn according to a recent survey by Wood (personal communication, 2015). FX-2 and FX-4 are the intermediate 500 m depth wells. (For interpretation of the references to colour in this figure legend, the reader is referred to the web version of this article.)

(Wanakasem and Takabut, 1986). Following the low resistivity zones (Coothongkul and Chinapongsanond, 1985), the shallow well (<100 m) drilling program around the hot spring yielded a flow of 22 l/s of 125 °C water (Ramingwong et al., 2000; Thienprasert et al., 1987). This flow rate was high enough to construct the 0.3 MW Fang demonstration geothermal power plant that has operated since 1988. It is currently the only geothermal power plant in Thailand.

Encouraged by the high temperature of the shallow wells, deep exploration was then continued in the 1990s in order to locate deeper reservoirs. In addition to the geological, electrical and geochemical surveys, four intermediate depth wells were drilled into

the crystalline basement to a depth of 500 m. Two wells (Fx-2 and Fx-4 in Fig. 2) were successful in producing hot water at a temperature of 125–130 °C from the granite fractures at depths of around 270, 337 and 417 m (Korjedee, 2002; Ramingwong et al., 2000), while the other two were non-productive. The extracted hot water from these wells is currently used to generate electricity. All of the drilled holes were less than 200 m from the hot springs (Fig. 2). At the end of the feasibility studies, previous investigators have concluded that the deep drilling exploration has a very high risk of missing the target if a conventional vertical drilling technique is used (Korjedee, 2002; Ramingwong et al., 2000). It was concluded

that the hot geothermal fluid mostly resides within the narrow fractures of the steeply dipping faults. The geothermal project started in the 1980s was therefore not continued until recently.

The geothermal project at Fang was resumed in the 2010s. Studies by Owens (2012) again suggested that the electrical power plant of the Fang geothermal system could be upgraded from 0.3 MW to 2.8 MW. The idea is that the flow rate could be increased by putting pump installations in the existing wells and drilling new wells. To reduce the risk of deep drilling, a geophysical technique such as controlled source audio-magnetotelluric (CSAMT) method was recommended to help define the narrow fracture zones within the granite rocks (Singharajwarapan et al., 2012) and to image the geothermal system of the area for the first time. However, the CSAMT method requires an extra source to produce an electromagnetic wave making it more expensive than the traditional magnetotelluric (MT) method, and its investigation depths are typically less than 500 m which is less than our target depth. Funded by the Department of Groundwater Resource (DGR), Ministry of Natural Resources and Environment of Thailand, the audio-magnetotelluric (AMT) and magnetotelluric (MT) methods which are standard methods for geothermal exploration were therefore recommended for the investigation of the Fang geothermal system prior to further drilling and well-field design.

Geothermal systems have been classified into many types according to the geologic controls of the area (Moeck, 2014). Many MT experiments have been conducted over very high temperature geothermal systems which were mostly of the magmatic play type according to the classification of Moeck (2014). They found that the resistivity structure consists of a thin, conductive layer corresponding to clay-rich rocks acting as low-permeability caprock on top of a relatively higher resistivity geothermal reservoir where the hot fluids reside (e.g., Gasperikova et al., 2015; Heise et al., 2008; Pritchett, 2004; Pellerin et al., 1996; Rosenkjaer et al., 2015; Uchida and Sasaki, 2006).

The Fang geothermal system is a relatively low temperature system. It was classified in the IFC-IGA report (IFC-IGA, 2014) as being of an extinct magmatic play type controlled by batholiths without associated volcanism or a plutonic play type if using the catalog of Moeck (2014). The Fang conceptual model by Takashima and Kawada (1981), Takashima and Jarach (1987), *Geotermica Italiana SRI* (1984), Praserdvigai (1986) and Raksakulwong (2008) shown in Fig. 3 proposed that a deep hot igneous body heats the trapped groundwater at greater depths to form a high temperature, deep geothermal reservoir. The hot fluid then rises up along the fractures of the fault zones to mix with the colder groundwater coming from above producing the geochemical equilibrium mixture of hot fluid with a temperature up to 160 °C. At shallower depths, the hot fluid is then stored along the fractures of the faults or within the weathered and altered granite rocks and the permeable sediments to form a shallower and lower temperature geothermal reservoir. Some of the hot fluid then continues ascending through the fault fractures to the surface in the form of hot springs.

According to the proposed conceptual model (Fig. 3), the results of MT surveys over the Fang geothermal system may produce a different resistivity structure from the conventional interpretation of magmatic types. The batholith heat source would likely be “mapped” as a high resistivity body, while the weathered rocks and permeable sediment filled with fluid would have a moderate resistivity. The hot fluid reservoir along the fractures of the fault might be “seen” directly as a conductive zone. The possibility of mapping the conductive clay caprock as in the magmatic play type is raised. One of our objectives of conducting the AMT and MT surveys over the Fang area is therefore to verify and validate the proposed conceptual model in Fig. 3 and to probe these major components of the Fang system. Location and size, particularly of the shallow hot fluid reservoir, will be useful for the assessment of the capability of the

Fang geothermal system to expand its power production. We start the paper with the geology of the Fang hot spring. The AMT and MT data acquisition, data processing and inversion are described next. The interpretation to relate the inverted 3-D resistivity model with the previously proposed geothermal system is then discussed, followed by the conclusion.

2. Geology of the Fang hot spring

The Tertiary Fang basin is oriented NNE-SSW and is 50 km long and 20 km at the central widest part (Fig. 1). The Mae Chan fault (MCF) forms the NW boundary and separates the crystalline rocks on the north from the sediments of the basin. The MCF extends 150 km SW from the Thai-Lao border on the east to its termination in the Fang Basin (Fenton et al., 2003; Uttamo et al., 2003; Kosuwan and Lumjuan, 1998). The west end terminates against a N-S trending belt of west-dipping folded Paleozoic sediment. The Paleozoic belt is not offset by the fault, and motion must be taken up by N-S-trending western boundary faults of the Fang Basin. East of the Fang basin, the MCF exhibits an active left-lateral strike-slip offset (Fenton et al., 2003; Kosuwan and Lumjuan, 1998). Its left lateral motion implies that the SE block is pulling away from the N-S western boundary fault, and this may be the cause of permeable openings in the vicinity of the hot springs. Several hot springs emanate from along the MCF (Wood and Singharajwarapan, 2014) including the Fang hot spring. 40 km east of Fang is another prominent geothermal system, the Mae Chan hot spring studied by Amatyakul et al. (2015).

Fig. 2 summarizes the geology of the Fang Hot Springs. The hot springs and hot wells are in crystalline rocks comprised of gneissic granite and mylonite. The Age of the rocks and mylonitization is uncertain because no zircon ages have been obtained. Past studies have labeled these crystalline rocks as Carboniferous, and some studies have labeled the rocks as Triassic. Overlying the crystalline rocks are folded quartzose sandstone, quartzite, and lesser amounts of limestone and shale. Imsamut and Krawchan (2005) considered these sediments to be a part of the Mae Tha Group of late Carboniferous age.

The contact between crystalline rocks and the quartz sandstone dips gently ($\sim 12^\circ$) to the southeast and is considered to be a low-angle detachment fault and was called the Doi Kia Fault (DKF) by Chaturongkawanich et al. (1980) and is shown in Fig. 2. The crystalline rocks and the overlying Paleozoic sediment detachment are faulted down to the southeast along the high-angle MCF which appears here to have a large vertical displacement. The downthrown southeast block of the MCF is comprised of Cenozoic basin-fill sediment overlying Paleozoic quartzite. Petroleum exploration wells 4 km southeast of the fault were drilled to a depth of 772 m in this sediment resting on a “quartzite basement”.

The Fang Hot Springs do not directly emanate from the trace of the MCF. Instead they flow from crystalline rock north of the fault. We observe that the hottest seeps ($>90^\circ\text{C}$) align along a $350\text{--}355^\circ$ (N – NW) alignment for a distance of 100 m. One of the successful 500-m-deep wells is along this alignment 200 m south of the seeps. This N – NW trend is parallel to the linear stream valley of the Mae Chai creek (written as Mae Jai creek in Fig. 2). Previous investigators have assumed this lineament controls the fracture system of the hot springs. The fault is not observed in the stream valley, although bedrock exposure is good north of the hot springs. Shawe (1984) noted a fault of this orientation, with horizontal grooves and slickensides on the fault plane, in the open pit of the Huai Sai Fluorspar Mine (Fig. 2). He also noted warm springs at the southeast end of the pit. The mine pit, 1 km south of the 500-m well, is now a pond and cannot be examined. We use the name “Mae Jai fault (MJF)” for this N – NW feature, but its understanding awaits

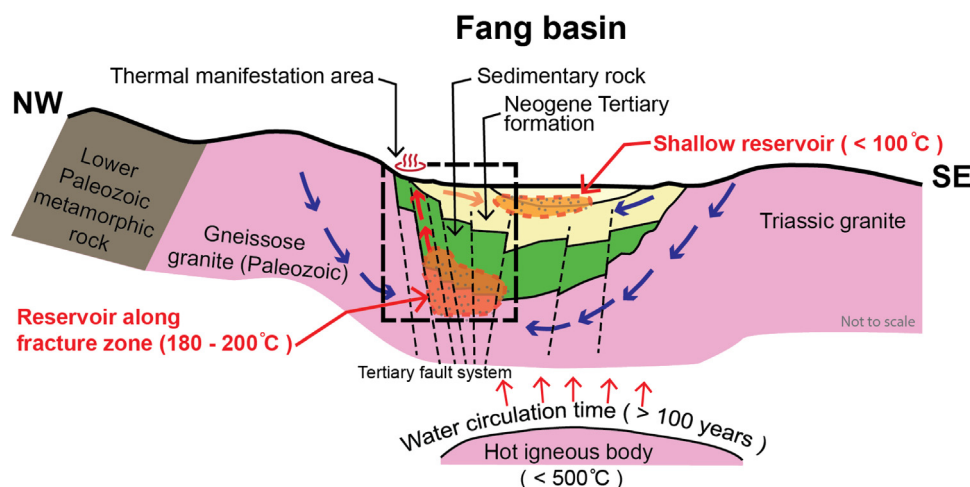


Fig. 3. The conceptual geothermal system of Fang hot spring redrawn after Takashima and Kawada (1981) and Takashima and Jarach (1987). The Black rectangle marks the area of our investigation.

more detailed mapping. Note: the name “Mae Chai” appears on the 1:50,000 topographic map 4848IV, but we use a spelling closer to the Thai pronunciation: “Mae Jai” to avoid confusion with the similar sounding Mae Chan fault.

3. Magnetotelluric survey

3.1. Data acquisition and data processing

In December 2014, 33 MT stations were deployed to cover the $6 \text{ km} \times 8 \text{ km}$ area of interest surrounding the Fang Hot Springs (Fig. 2). Since local communities are distributed in the area, the site was designed according to the accessibility of land. The site spacing between stations is 500 m on average. The northern part of the Fang hot spring is inaccessible as it belongs to the Doi Pha Hom Pok national park. Most of the sites are therefore located within the sedimentary basin which is easy to access, whereas only a few sites are located on granite, limestone and sandstone rocks. Four sets of MT equipment that record the electric fields in the x - and y -directions (E_x and E_y) and the magnetic fields in the x -, y - and z -directions (H_x , H_y and H_z) were deployed overnight at four locations for about 20 h in order to acquire broadband data up to 1000s, where x is oriented north, y is oriented east and z is vertically downward. These four sets of equipment were then moved to acquire data at other locations shown in Fig. 2 for the total of 33 stations. Coils, magnetometers and data acquisition units are from KMS Technologies – KJT Enterprises Inc., Houston, Texas. To improve the data quality, another set of equipment was set up about 600 km south of the study area in Kanchanaburi province (Fig. 1) as a remote reference site. The data from the four local sites was then processed with the data from the remote site using KMS processing software based on the robust multiple-station technique of Egbert (1997).

For high frequency magnetic fields ($>1000 \text{ Hz}$), high-frequency coils replaced the broadband magnetic coils to acquire the high frequency data for less than 30 min in each site. As we have only two sets of high-frequency coils, two local sites can therefore be acquired simultaneously. The two local sites then become a remote site for each other. However, as both are not too far from each other (less than 2–4 km), the data quality is not greatly improved.

After the data processing (Egbert, 1997), the high frequency band and broadband data were merged together. The very high frequency ($>3000 \text{ Hz}$) and the very long period ($>300 \text{ s}$) data are of much poorer data quality and were therefore removed. This leaves us the data (impedance tensor \mathbf{Z} and the vertical magnetic transfer

function \mathbf{T}) from a period of 3000 Hz to 300 s for each site. To proceed to the inversion part, about 16 periods per site of the data were chosen at regular intervals on a \log_{10} scale in this frequency range. Although the impedance tensor \mathbf{Z} was used in the inversion, here, for simplicity, we instead plot the apparent resistivity and phase of the xy - and yx -modes with the error bars for some selected stations in Fig. 4 and the vertical magnetic transfer function or tipper in Fig. 5. Most of the on-diagonal data is severely contaminated by local noise and will be discarded for the inversion.

3.2. Three-dimensional inversion and the inverted model

The 16 periods off-diagonal impedance tensors and the tippers of all sites with the minimum error floor for both data sets at 5% are included for the 3-D inversion using the WSINV3DMT parallel version (Siripunvaraporn and Egbert, 2009; Siripunvaraporn et al., 2005). The inverse model was discretized using a $60 \times 60 \times 55$ grid (with air layers on top of the topography) in the north-south, west-east and vertical directions, respectively. The grid spacing within the study area (Fig. 2) for the horizontal direction is 100 m. To avoid the boundary effects, the grid spacing is then increased in a logarithmic scale in both directions. In the vertical direction, the grid of the first layer was discretized finely enough to provide very high accuracy responses for all periods where the size of each subsequent layer is 1.2–1.8 times that of the previous layer. The accuracy of this discretized grid was tested with various half-space resistivity values from 1 to 1000 $\Omega \text{ m}$, and was shown to have less than 1% error, which is also less than the minimum error floors setting for the data. The workflow to obtain the final 3-D resistivity model is analogous to those presented in both Amatyakul et al. (2015) and Lindsey and Newman (2015) where coarse structures are recovered first followed by further sequential refinements performed here by adjusting the inversion parameters. The inversion was run with different initial models from a 10 $\Omega \text{ m}$ half-space to 1000 $\Omega \text{ m}$ half-space with a large smoothing factor. The inverted model from the initial half-space of 300 $\Omega \text{ m}$ fits the data better. It was then selected as a starting and reference model for re-inversion with a smaller smoothing factor. At the end, we obtained a preferred inverted model that yields an acceptable RMS of 2.1 and fits well with the geology of the area. The observed data and calculated responses of some selected stations are plotted in Figs. 4 and 5.

The final inverted resistivity model is displayed in top view in Fig. 6 and in cross-sectional views perpendicular to the MCF in Fig. 7. It consists of four main structures which will be interpreted in the

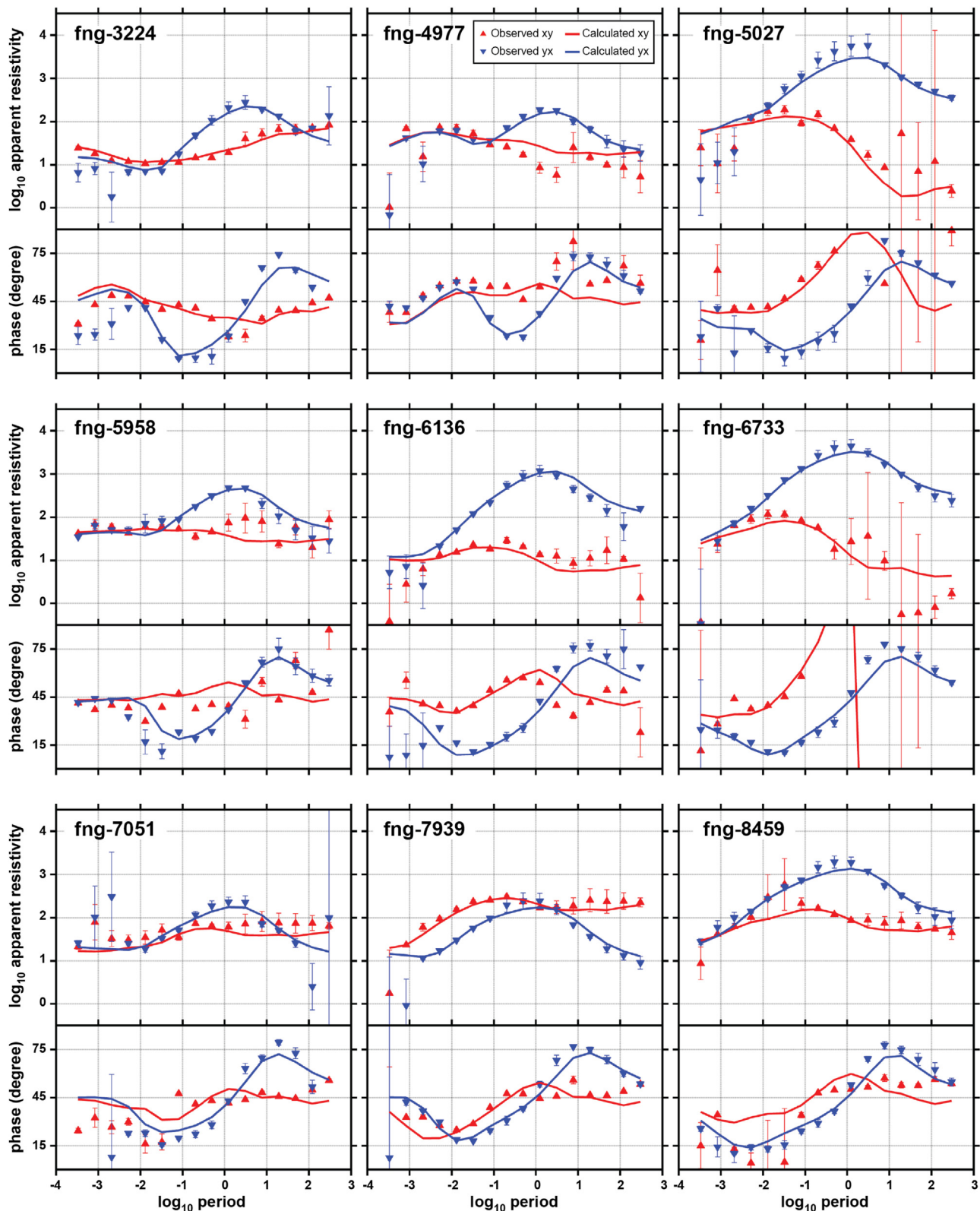


Fig. 4. Selected apparent resistivities (ohm-m) and phases (degree) as a function of \log_{10} periods (second) computed from the off-diagonal impedance tensor at various locations acquired in the locations marked as blue crosses in Fig. 2. Red is xy and blue is yx mode. The “upward” and “downward” triangles and error bars are from field measurement, and the solid lines are the calculated responses generated from the inverted model shown in Figs. 6 and 7. (For interpretation of the references to colour in this figure legend, the reader is referred to the web version of this article.)

next section. (1) The high resistivity structure labeled as R (in blue in Figs. 6 and 7), where the resistivity is greater than $300 \Omega \text{ m}$, appears mostly in the northern part of the study area before propagating

southeastward at greater depths. (2) The moderate resistivity structure marked as M (in yellow and green in Figs. 6 and 7), where the resistivity is around $30\text{--}300 \Omega \text{ m}$, is mostly in the southern

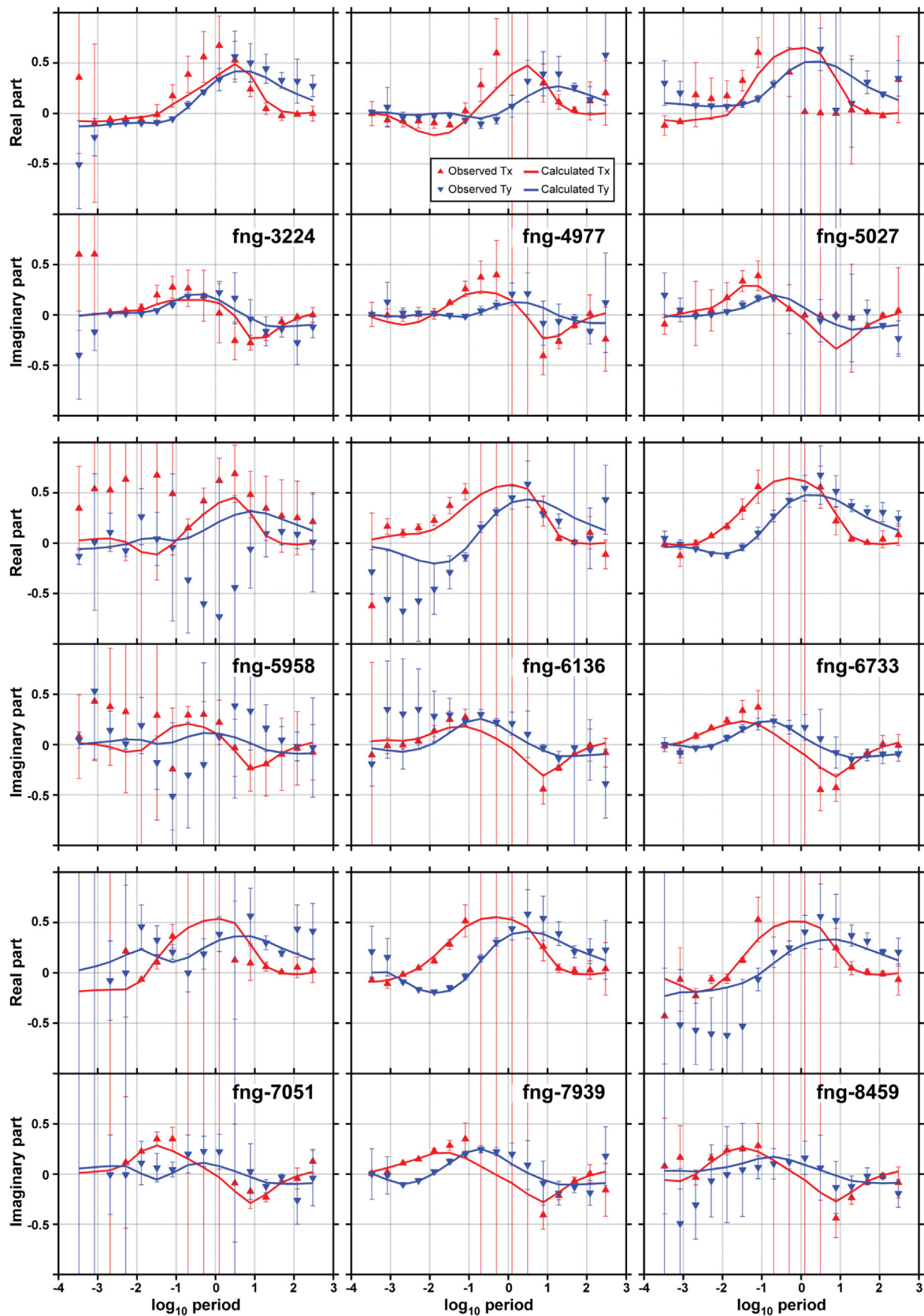


Fig. 5. Real and imaginary parts of vertical magnetic transfer functions (tipper) as a function of \log_{10} periods (second) at various locations acquired in the locations marked as blue crosses in Fig. 2. Red is zx and blue is zy mode. The “upward” and “downward” triangles and error bars are from field measurement, and the solid lines are the calculated responses generated from the inverted model shown in Figs. 6 and 7. (For interpretation of the references to colour in this figure legend, the reader is referred to the web version of this article.)

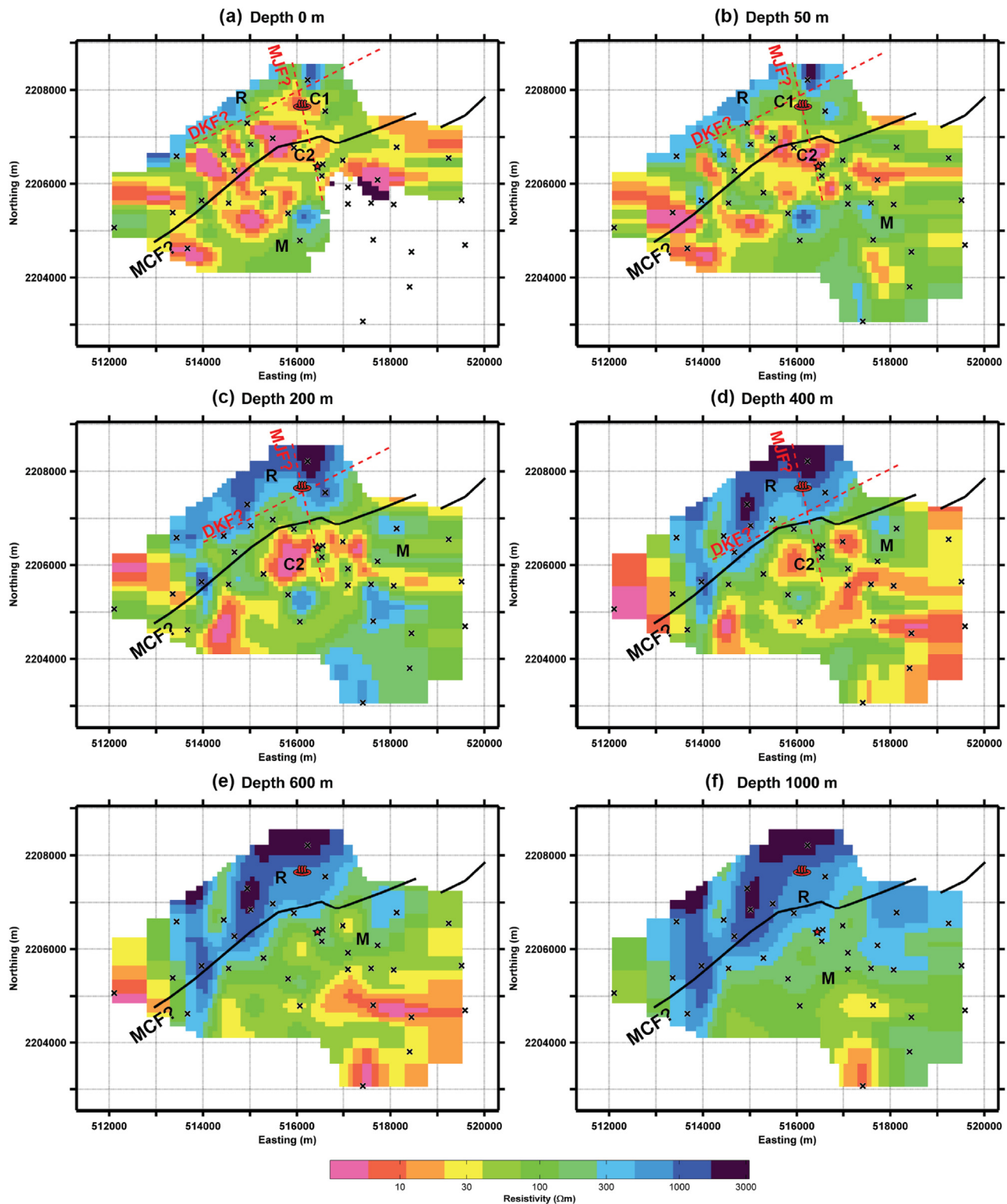


Fig. 6. The plane-view of the final inverted model shown as horizontal slices at (a) surface, depths of (b) 50 m, (c) 200 m, (d) 400 m, (e) 600 m, and (f) 1000 m. MT locations are marked as crosses (for the station names, refer to Fig. 2). MCF is the Mae Chan Fault based on the surface trace. The local faults are drawn in red dashed straight lines based on the observed resistivity contrasts, in which they also change with depth. R is the high resistivity zone associated with the granite rock, while M is for the lower resistivity zone corresponding to the sedimentary rock of the Fang basin. C1 and C2 are the two low resistivity zones expected to be hot geothermal reservoirs. (For interpretation of the references to colour in this figure legend, the reader is referred to the web version of this article.)

part and at shallow depth in the study area. At greater depth, it is replaced with the high resistivity structure. (3) The resistivity contrasts between both structures can be observed at shallower depth

to great depth. These resistivity contrasts seem to be associated with the presence of the major and minor faults in the area.

(4) Although there are many conductive anomalies distributed throughout the study areas, we are solely interested in just the two

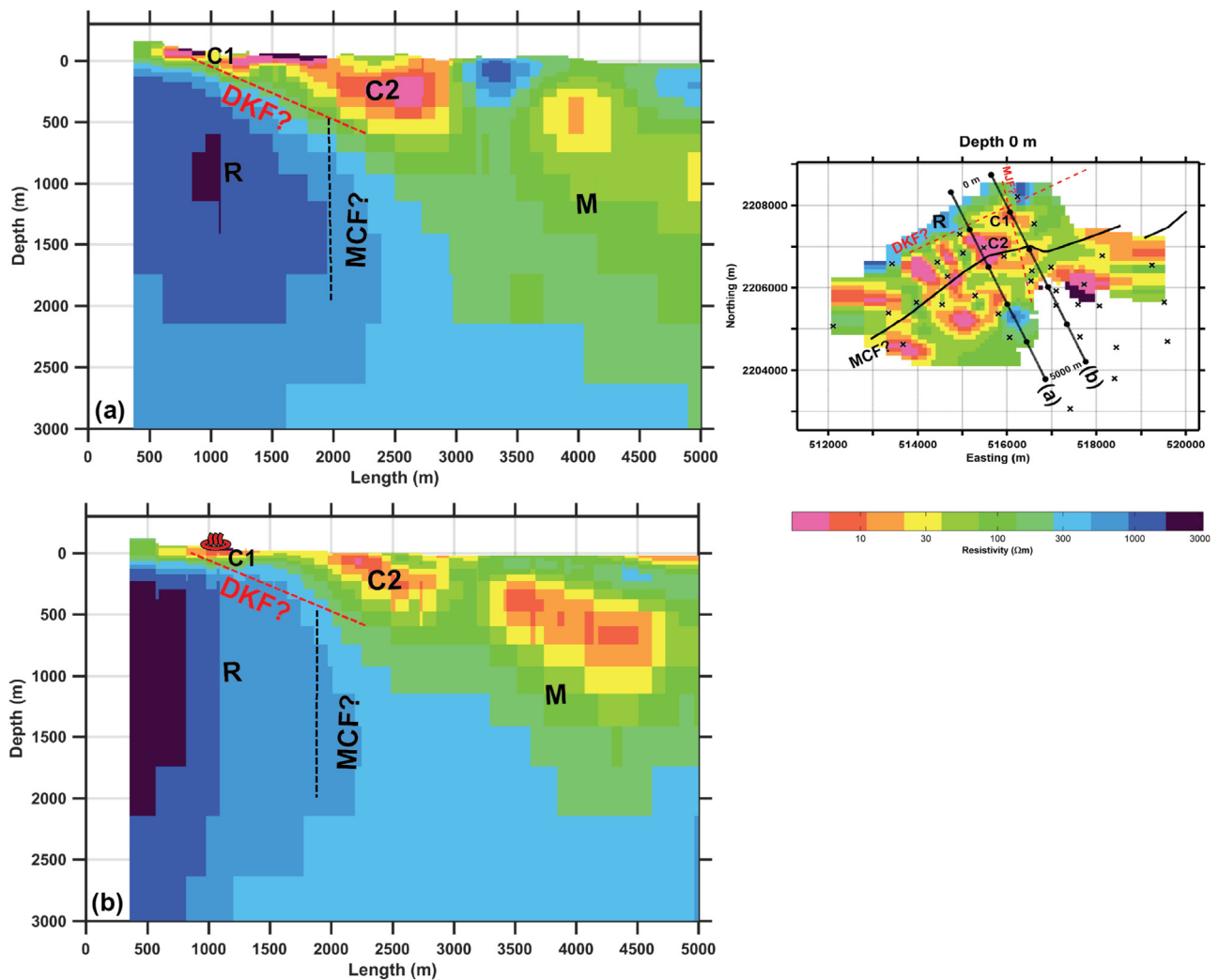


Fig. 7. (a) and (b) are cross-sectional plots of the final inverted model (Fig. 6) from northwest to southeast perpendicular to the Mae Chan Fault (MCF) and the Doi Kia Fault (DKF) where (b) cuts through the Fang hot spring and (a) is about 1 km south of (b). The red dashed lines are the estimated orientation of the DKF. The black dashed line shows the orientation of the MCF. (For interpretation of the references to colour in this figure legend, the reader is referred to the web version of this article.)

conductive anomalies (where the resistivity is lower than $30 \Omega \text{ m}$) located around the middle of the study area labeled as C1 and C2 (Figs. 6 and 7) since there is direct evidence of hot fluid found in the areas of these two conductors, and no hot fluid found in the area of the other conductors. Conductor C1 is located in the vicinity of the Fang hot spring zone but appears only within the upper 50 m. Conductor C2 is about 1 km south of the hot spring and can be seen from near the surface to a depth of 500 m. Its width decreases and its resistivity increases with depth.

As conductor C1 and C2 are important and will be mentioned numerous times in the next section, it is better to verify their existence. To validate the conductors C1 and C2 in Figs. 6 and 7, we replaced C1 first with the neighboring resistivity values (between $100\text{--}300 \Omega \text{ m}$) to simulate the case that C1 does not exist. We then ran the forward modeling to fit the observed data. The relative changes of the RMS values were calculated via

$$\text{Relative Change} = 100\% \times (\text{RMS}_{\text{new}} - \text{RMS}_{\text{original}}) / \text{RMS}_{\text{original}},$$

for each station and plotted in Fig. 7, where RMS_{new} is the fit to the data after replacing the conductor with the neighboring resistivity, and $\text{RMS}_{\text{original}}$ is the RMS value from the inverted model of Fig. 6. By replacing the conductor C1 with the neighboring resistivity, the overall RMS increases from 2.1 to 2.6 (a 24% increase)

indicating that the observed data really requires the C1 conductor. The relative change of RMS misfit at each site (Fig. 8a) shows that the misfits at the stations in the surrounding area of C1 change significantly certifying that C1 is needed by these stations.

A similar experiment is performed for the C2 conductor. We found that the overall RMS increases from 2.1 to 2.3 (a 9.5% increase). The overall change of RMS for C2 is less than that for C1. This is because C2 is deeper and smaller in size with a result that contribution from C2 is much less than from C1. Fig. 8b shows that the misfits of the stations in the surrounding area of C2 change dramatically after replacing C2 with neighboring resistivities. Both of these experiments (Fig. 8) confirmed that both conductors are required by the data and are not artifacts from the inversion.

4. Interpretation and discussion

Our inverted resistivity model (Figs. 6 and 7) is consistent with the surface geology of Fig. 2. By matching the surface resistivity (Fig. 6a) to the surface geology (Fig. 2), the high resistivity (R) zone in the northwest (in blue in Fig. 6a) is in agreement with the granite rock (Fig. 2). The lower resistivity zone (M) covering the southwestern part of the area (in yellow and green in Fig. 6a) corresponds to the Fang sedimentary basin in Fig. 2. The resistivity contrast between the high zone and low zone in the north matches well with

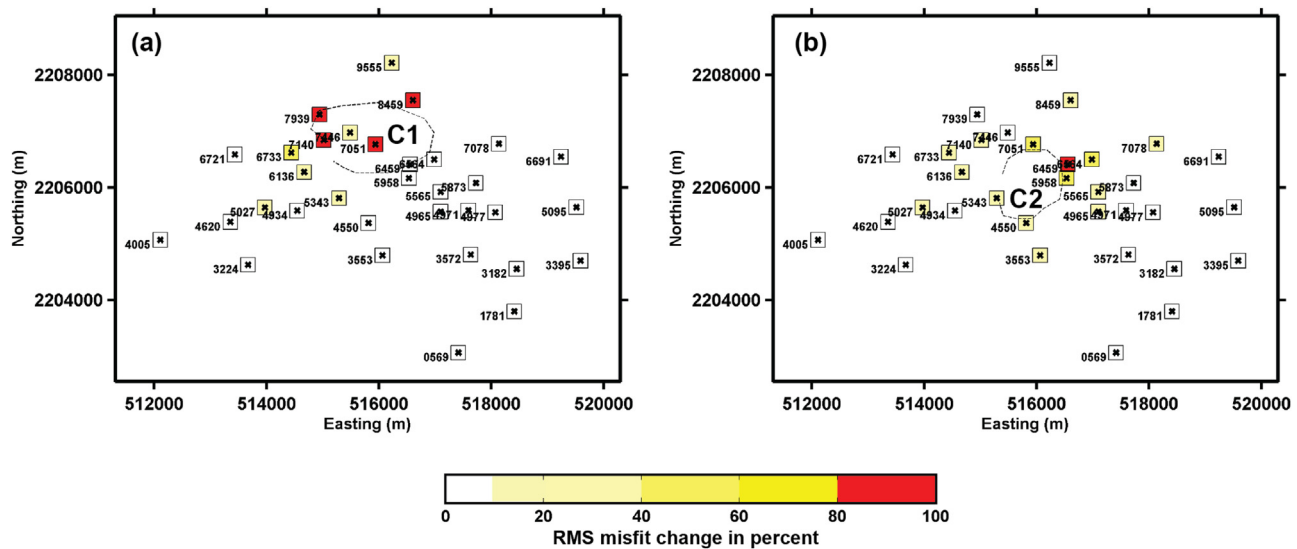


Fig. 8. Plots of relative change of RMS misfit between the observed data and the calculated data of each station (a) after replacing the C1 conductor of the inverted model (Figs. 6 and 7) with the neighboring resistivities and (b) after replacing the C2 conductor with the neighboring resistivities.

the surface trace of the Doi Kia Fault (DKF). Similarly, the resistivity contrast at the end of the thin conductive C1 zone in the northeast of the area appears to be consistent with the presence of the Mae Jai Fault (MJF). In Fig. 6a, for simplicity we represent the resistivity contrasts associated with both faults as straight lines instead of the actual surface trace as in Fig. 2. The intersection of both resistivity contrasts in the north encloses the high conductor C1 where its location corresponds to the position of the Fang hot spring (Figs. 6a and 2).

To infer the deeper structures, we assume that the same structures observed at the surface continue to greater depths. At depth (Fig. 6b–f), the resistive granite rock R showing in the northwest at the surface (Fig. 6a) appears in the southeast (Fig. 6b–f) and terminates at a depth of 600 m when it encounters the MCF. At depths below 2 km (Fig. 7), the study area overlies a high resistivity zone indicating the granite rocks lie beneath. It also indicates that the Fang basin has a thickness of around 2 km in this area. In earlier studies, geologists proposed that the possible heat sources of the Fang geothermal system are either a deep hot (>300 °C) igneous body or the radiogenic heat from the granite rock or both (Takashima and Kawada, 1981; Takashima and Jarach 1987). As our investigation depth is within the upper crust, one possible source of heat, the batholith granite lying beneath, is clearly imaged in this study (Fig. 7).

At the surface, the DKF separates the resistive granite and the conductive structure. The cross-sectional plots of the profiles perpendicular to the DKF and the MCF show that the resistivity contrast corresponding to the DKF at the surface dips southeast with a shallow angle and ends at the MCF (Fig. 7). Unfortunately, the cross-sectional plot parallel to the DKF and the MCF does not clearly show the MJF as in the case of the DKF. For the major MCF, the resistivity contrast near the surface is not distinct as the MCF's surface trace cuts through the high conductivity zones associated with the sedimentary rock and weathered granite rocks filled with fluid (Figs. 6 and 7). However, at depths deeper than 600 m, the resistivity contrast in the north and south of the MCF becomes prominent (Figs. 6e, f and 7). The MCF clearly separates the high resistivity granite rock in the northwest and the moderate resistivity sediments (M) of the Fang basin in the south.

Although there are many high conductivity zones in Fig. 6, here the most interesting feature and the focus of our study is just the C1 and C2 conductors labeled in Figs. 6 and 7. As stated before, there

is evidence to link the hot fluid to both conductors. There are three possible major sources for the low resistivity zones shown as C1 and C2 in Fig. 6. The 120 °C water at Fang has a resistivity of 4–8 Ω m as it contains ions dissolved from the rock mineral. When residing in fractures of weathered and altered rocks or sediments, it thus brings down the bulk resistivity of the rocks producing low resistivity zones. Another possible source is the clay-rich rock as interpreted in the other geothermal systems (e.g., Gasperikova et al., 2015; Heise et al., 2008; Rosenkjaer et al., 2015; Uchida and Sasaki, 2006). The third possible interpretation is a combination of both sources.

The C1 conductor is shallow (<100 m depth) and located only beneath the Fang hot spring zone (Figs. 6 and 7). The area beneath C1 was drilled during the 1980s and 1990s from a shallow depth (<100 m) to an intermediate depth (<500 m) (Raksaskulwong, 2011; Thienprasert et al., 1987; Wanakase and Takabut, 1986; Geotermica Italiana SRI, 1984). According to the X-ray diffraction analysis of the cuttings from one well near the hot spring (Ratanasthien et al., 1985), clay content is found intervening with weathered boulders and cataclastic granite at shallow depths (less than 50 m). Unfortunately, no other information about the clay content can be found from the other wells. It is therefore not certain that the low resistivity zone C1 is a result of just the clay-rich rock. Since hot fluid can be extracted from the shallow wells from various depths, one possible interpretation of the C1 is a shallow fracture reservoir trapping the hot fluid within the fractures of altered rock mixed with clay content. The hot fluid from the C1 reservoir then seeps through the surface via the DKF and the MJF. The hot fluid from the C1 reservoir has been used to generate the electricity for many decades.

Another interesting anomaly is the C2 conductor (Figs. 6 and 7) which was not discovered in the past exploration. It is about 1 km south of the Fang hot spring directly below the Huai San Fluorspar Mine (Fig. 6), and just south of the MCF. Unlike C1, the C2 anomaly extends from a shallow depth to a depth of 500 m. At a depth of 200 m, it is roughly 1 km wide. Based on the USGS open report (Shawe, 1984), there are warm water springs (whose temperature was not recorded) found at the bottom of the Huai San Fluorspar Mine, coincidentally above the C2 zone. The warm spring is likely to rise along the MCF from a greater depth. Since hot fluid is found in the area, we proposed two possible interpretations for C2.

First, the low resistivity might just be due to the clayey sedimentary rock (Fig. 2) which is part of the Fang basin. This is similar

to the case of the low resistivities found near petroleum exploration wells (Giao et al., 2011). Since hot fluid is found to rise from below, it is possible that this clay-rich semi-consolidate terrace deposit acts as an impermeable zone that traps the hot fluid reservoir directly beneath. This interpretation is basically similar to the caprock concept of the geothermal high temperature magmatic type (e.g., Gasperikova et al., 2015; Heise et al., 2008). According to the Fang conceptual model shown in Fig. 3, conducting an MT survey along the surface, we would expect to “see” the fracture geothermal reservoir as a conductive zone, as with the C1 conductor. Our second interpretation of the C2 conductor is therefore a fracture geothermal reservoir. The hot fluid ascending from deep below is stored in the pores of the sedimentary rock and the fractures of the altered granite beneath before rising to the surface. Whether it is the first or second interpretation, hot fluid residing at depths beneath the C2 anomaly is probably the source of the Fang hot spring. Since the high angle MJF and low angle DKF intersect the MCF in the north of the C2 zone, these local faults act like a passageway for the hot fluid to flow upward to the Fang hot spring as clearly shown in Fig. 7a and b. This is supported by the successful wells located along these faults (Fig. 2) to extract the hot fluid at intermediate depth.

Both interpretations indicate the value of the C2 anomaly as it helps with locating the geothermal reservoir. We therefore need to prove its existence. If the C2 zone fits with the first interpretation, the geothermal reservoir is deep and directly below the C2 anomaly. If it agrees with the second interpretation, the geothermal reservoir is the C2 zone itself which is less depth. Thus the C2 anomaly is possibly an important target for the future drilling location for the geothermal power plant expansion. Drilling over the C2 anomaly will clearly help reveal the geology of Fang geothermal system. We wish to know whether it is a clay-rich semi-consolidate terrace deposit or just a geothermal reservoir. Since the land above C2 lies just outside the Doi Pha Hom Pok national park where the Fang hot spring and the demonstration Fang geothermal power plant are part of, the proposed drilling location above the C2 is possible. In addition, if the fluid rises directly through the MCF from the deep source, its temperature can be expected to be higher than that at the Fang hot spring if it does not mix with the underground water.

5. Conclusion

A geothermal system with potential to generate electricity commercially is the Fang hot spring which currently hosts the only geothermal power plant in Thailand with a power of 0.3MW. The expansion project was halted due to the failure to access a greater flow of hot fluid. In the 2010s, the Fang geothermal project was resumed starting with a magnetotelluric survey. The goal was to gain more understanding about the geothermal system of the Fang hot spring. Thirty-three MT stations covering southern region of the Fang hot spring (northern part is inaccessible as it belongs to the national park) were then installed for 2–3 weeks. A remote site about 600 km south of the study area was also installed during the same period of time to improve the acquired data quality. After the data processing, the data was inverted to produce the 3-D resistivity model.

The obtained 3-D resistivity model is consistent with the geology of the area at the surface. There are many interesting features in the 3-D resistivity model. (1) The high resistive zone R observed in the north of the study area before dipping southward at great depths covers the whole area of study. The high resistivity is consistent with the crystalline granite rocks. It covers a large area and depth. The radiogenic heat from the granite rock may heat the trapped fluid at great depth. Outside of the resistive zone, (2) an

intermediate resistive zone (M) is found in the topmost few kilometers. It is interpreted as the Fang sedimentary basin. (3) The resistivity contrast between the high and lower resistivities also matches well with major and minor faults in the area. The resistivity contrasts in the northwest shows that the Doi Kia Fault (DKF) dips southward at a shallow angle and terminates at the major Mae Chan Fault (MCF) in the south. The resistivity contrast between the high resistivity R zone and the intermediate resistivity M zone does not appear until around a depth of 500 m. This contrast is in agreement with the MCF in which the region near the surface was covered with the high conductivity zone.

The focus of this study was mainly on (4) the two conductors: C1 beneath the Fang hot spring and shallow, and C2 about 1 km south of the Fang hot spring and deeper. Based on the evidence of the hot fluid found at the surface, both of them appear related to surface flows of hot water. C1 is a shallow fracture reservoir storing the hot fluid coming from the C2 zone using the DKF and the MJF as a passageway to rise to the surface. C2 is more interesting as it is interpreted as either the clay-rich semi-consolidate terrace deposit on top of the geothermal reservoir or the fracture geothermal reservoir. Either case may be a response to a larger geothermal system that leaked warm water through the MCF at the bottom of the fluorspar mine about 1 km south of the hot springs. The mine is currently filled with drainage water from the power plant and cannot be examined.

Our study is in agreement with the past drilling during 1990s in the vicinity of Fang hot spring above the C1 conductor. The shallow bore holes have been used to draw the hot fluid stored in the C1 conductor to produce electricity for the past few decades. Since C1 has been explored before, this study recommends the exploration and drilling over the C2 conductor which is deeper and might be larger in volume. If C2 is really the geothermal fluid reservoir, the drilled well can be shallow. However, if it is the clay-rich semi-consolidate terrace deposit, drilling may have to be made deeper below the C2 anomaly in order to reach the hot fluid. Both interpretations of the C2 conductor demonstrate that the expansion of the geothermal power plant in the Fang area is possible.

Acknowledgements

The authors would like to thank the Thailand Research Fund (RSA5780010) and the department of groundwater resource (DGR) for the support and permission to publish this study. Mr. Puwis Amatyakul would like to thank the Development and Promotion of Science Talents project (DPST) for a scholarship. We appreciate the technical support during the field work from Mr. Wiboon Kaentao and Miss Rapeeporn Sakulnee of Ensol Co., Ltd. & Panya Consultants Co., Ltd. and Mr. Benchawut Piromfong of Curl-E Geophysics Co., Ltd. We also would like to thank Dr. Kurt Strack and Mr. Tilmann Hanstein of KMS technologies – KJT Enterprises Inc. for the MT instruments used in the field survey and technical support, and Dr. Michael Allen for editing the English of this manuscript.

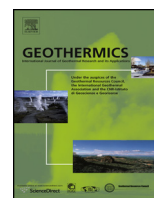
References

- Amatyakul, P., Rung-Arunwan, T., Siripunvaraporn, W., 2015. A pilot magnetotelluric survey for geothermal exploration in Mae Chan region, northern Thailand. *Geothermics* 55, 31–38.
- Chaturongkawanich, S., Wongwanich, T., Chuaviroj, S., 1980. *Geology of Amphoe Fang, Changwat Chiang Mai Scale 1:15,000*. Geological Survey Division, Department of Mineral Resources, Bangkok, Thailand (pp. 49).
- Coothongkul, V., Chinapongsanond, P., 1985. *Resistivity Survey Fang Geothermal Prospect, Ban Pong Nam Ron*. Electricity Generating Authority of Thailand, Amphoe Fang, Chiangmai, Thailand (pp. 61).
- Egbert, G.D., 1997. Robust multiple-station magnetotelluric data processing. *Geophys. J. Int.* 130, 475–496.
- Fenton, C.H., Charusiri, P., Wood, S.H., 2003. Recent paleoseismic investigations in northern and western Thailand. *Ann. Geophys.* 46, 957–981.

- Gasperikova, E., Rosenkjaer, G.K., Arnason, K., Newman, G. a., Lindsey, N.J., 2015. Resistivity characterization of the Krafla and Hengill geothermal fields through 3D MT inverse modeling. *Geothermics* 57, 246–257.
- Geotermica Italiana SRI, 1984. Geothermal Reconnaissance Survey of Northern Thailand – Final Report. Pisa, Italy, pp. 86 (unpublished report).
- Giao, P.H., Doungnoi, K., Senkhamwong, N., Srihiran, S., 2011. Assessment of Petroleum Resources for the South Fang Basin: Uncertainties and Difficulties. Department of Mineral Fuels, Ministry of Energy, Bangkok, Thailand, The 4th Petroleum Forum: Approaching to the 21st Petroleum Concession Bidding Round, May 26–27, 74 p.
- Heise, W., Caldwell, T.G., Bibby, H.M., Bannister, S.C., 2008. Three-dimensional modelling of magnetotelluric data from the Rotokawa geothermal field Taupo Volcanic Zone, New Zealand. *Geophys. J. Int.* 173, 740–750.
- IFC-IGA, 2014. Best practices guide for geothermal exploration, 196 p. http://www.ifc.org/wps/wcm/connect/topics_ext_content/ifc_external_corporate_site/ifc+sustainability/learning+and+adapting/knowledge+products/publications/publications.handbook.geothermal-bp-2ed.
- Imsamut, S., Krawchan, V., 2005. Geology of Amphoe Fang Quadrangle (4848 IV) and Doi Pha Wok Quadrangle (4748 I), scale 1:50,000: Bureau of Geological Survey. Department of Mineral Resources, Technical Report no BGS 33/2548, 157 p. (in Thai).
- Korjedge, T., 2002. Geothermal exploration and development in Thailand. *World Geotherm. Congr.* 11, 56–66 (2000).
- Kosuwat, S., Lumjuan, A., 1998. Neotectonics of Mae Chan Fault in Mae Chan District, Chiang Rai Province Geological Survey Division. Department of Mineral Resources, Bangkok, Thailand.
- Lindsey, N.J., Newman, G.A., 2015. Improved workflow for 3D inverse modeling of magnetotelluric data: examples from five geothermal systems. *Geothermics* 53, 527–532.
- Moeck, I.S., 2014. Catalog of geothermal play types based on geologic controls. *Renew. Sustain. Energy Rev.* 37, 867–882.
- Owens, L., 2012. Initial Assessment of High Potential Geothermal Sites in Northern Thailand. Ormat Technologies, Inc., NV, USA, pp. 8 (unpublished report).
- Pellerin, L., Johnston, J.M., Hohmann, G.W., 1996. A numerical evaluation of electromagnetic methods in geothermal exploration. *Geophysics* 61 (1), 121–130.
- Praserdvigai, S., 1986. Geothermal development in Thailand. *Geothermics* 15, 565–582.
- Pritchett, J.W., 2004. Finding Hidden Geothermal Resources in the Basin and Range Using Electrical Survey Techniques: a Computational Feasibility Study Report SAIC-04/1031. Science Applications International Corporation, San Diego, CA, USA (202 pp).
- Raksaskulwong, M., 2008. Thailand geothermal energy: development history and current status. *Proc. 8th Asian Geotherm. Symp.*, 39–46.
- Raksaskulwong, M., 2011. Four decades of geothermal research and development in Thailand. The 9th Asian Geothermal Symposium, 7–9.
- Ramingwong, T., Lertsrimongkol, S., Asnachinda, P., Praserdvigai, S., 2000. Update on Thailand geothermal energy research and development. *World Geotherm. Congr.* 2000 (2), 377–386.
- Ratanasthien, B., Panjasawatwong, Y., Yaowanoyothin, W., Lerdtthusnee, S., Haraluck, M., 1985. Water Qualities of Geothermal Fluids from San Kamphaeng and Fang Geothermal Systems. Final Report to Electrical Generating Authority of Thailand (249 p).
- Rosenkjaer, G.K., Gasperikova, E., Newman, G.A., Arnason, K., Lindsey, N.J., 2015. Comparison of 3D MT inversions for geothermal exploration: case studies for krafla and hengill geothermal systems in Iceland. *Geothermics* 57, 258–274.
- Shawe, D.R., 1984. Geology and Mineral Deposits of Thailand. Open-File Report. U.S. Geological Survey 84–403.
- Singharajwarapan, F.S., Wood, S.H., Prommakorn, N., Owens, L., 2012. Northern Thailand geothermal resources and development—a review and 2012 update. *Trans. Geotherm. Resour. Counc.* 36, 2–6.
- Siripunvaraporn, W., Egbert, G., 2009. WSINV3DMT: vertical magnetic field transfer function inversion and parallel implementation. *Phys. Earth Planet. Inter.* 173, 317–329.
- Siripunvaraporn, W., Egbert, G., Lenbury, Y., Uyeshima, M., Ogawa, Y., Junge, A., Jones, A.G., Siripunvaraporn, W., Egbert, G., Lenbury, Y., Uyeshima, M., 2005. Three-dimensional magnetotelluric inversion: data-space method. *Phys. Earth Planet. Inter.* 150, 3–14.
- Takashima, I., Jarach, W., 1987. Isotope geochemistry of six geothermal in northern Thailand. *Bull. Geol. Surv. Jpn.* 83, 33–40.
- Takashima, I., Kawada, K., 1981. Geothermal resources of Thailand, 325. *Chishitsu News*, pp. 16–29.
- Thienprasert, A., Chuaviroj, S., Chaturongkawanich, S., Jaraj, W., Sophonpongpihat, P., Surinkum, A., Raksaskulwong, M., 1987. Geothermal Energy Resources in Northern Thailand Geothermal Project, Report of Investigation 1. Geological Survey Division. Department of Mineral Resources, Bangkok, Thailand (pp. 208).
- Uchida, T., Sasaki, Y., 2006. Stable 3D inversion of MT data and its application to geothermal exploration. *Explor. Geophys.* 37, 223–230.
- Uttamo, W., Elders, C., Nichols, G., 2003. Relationships between Cenozoic strike-slip faulting and basin opening in northern Thailand. *Geol. Soc. Lond. Spec. Publ.* 210, 89–108.
- Wanakasem, S., Takabut, K., 1986. Present status of Fang geothermal project, Thailand. *Geothermics* 15, 583–587.
- Wood, S.H., Singharajwarapan, F.S., 2014. Geothermal systems of Northern Thailand and their association with faults active during the quaternary, in: transactions—Geothermal Resources Council. *Geotherm. Resour. Counc.*, 607–615.

ภาคผนวก ค. Reprint

- Puwis Amatyakul, Tawat Rung-Arunwan, and **Weerachai Siripunvaraporn**, 2015, A pilot magnetotelluric survey for geothermal exploration in Mae Chan region, northern Thailand, Geothermics, 55, 31 – 38. (**IF2015 = 2.323**)



A pilot magnetotelluric survey for geothermal exploration in Mae Chan region, northern Thailand



Puwis Amatyakul, Tawat Rung-Arunwan, Weerachai Siripunvaraporn*

Department of Physics, Faculty of Science, Mahidol University, 272 Rama 6 Road, Rachatawee, Bangkok 10400, Thailand

ARTICLE INFO

Article history:

Received 10 June 2014

Accepted 21 January 2015

Keywords:

Magnetotelluric

Geothermal

Thailand

ABSTRACT

There are many potential sites for geothermal power plants in Thailand. After many years of geological and geophysical surveys, a pilot magnetotelluric (MT) survey was made to assess the reservoir of the Mae Chan geothermal area, northern Thailand, which is one of the key areas for geothermal development. Seven MT sites were deployed in a $3\text{ km} \times 4\text{ km}$ area around the Mae Chan district covering the Mae Chan hot springs. The MT data were acquired at low and high frequency ranges and were inverted using a 3-D MT inversion to yield the 3-D resistivity structure of the area. The results show that there are two conductive zones near the surface associated with the hot fluid of the Mae Chan hydrothermal system. The hot fluid reservoir mostly resides at less than 500 m below the surface in weathered and fractured granite and in the overlying sedimentary deposits. Its source rock is imaged as a resistive zone corresponding to the hot granite batholith below it. The hot fluid rises up along the Mae Chan fault. The fault is clearly observed as a resistivity contrast extending from the surface to depth. It dips at a moderate angle. From the measured temperature of the fluid from a drill hole and the estimated temperature of the granite rock from the resistivity structure we conclude that the Mae Chan geothermal area is likely to be suitable for immediate development of a small-scale geothermal power plant.

© 2015 Elsevier Ltd. All rights reserved.

1. Introduction

To reduce Thailand's growing dependence on fossil fuels, finding alternative sources of energy is vital for the Thai economy. Geothermal energy has become a choice for many countries around the world during the past few decades because of its low cost and low emissions. Northern Thailand is one of the areas where the potential for geothermal power plants is very high (Barr et al., 1979; Chuaviroj, 1988; Owens, 2012; Singharajwarapan et al., 2012). Many of the hot springs in northern Thailand (Fig. 1a) have a temperature exceeding 80°C (Chuaviroj, 1988; Singharajwarapan et al., 2012; Subtavewung et al., 2005). These hot springs are commonly associated with strike-slip fault zones (Fig. 1a) such as the Mae Chan Fault (MCF), the Mae Hong Son Fault (MHF), and the Pha Yoa Fault. These faults formed as the Indian plate subducted beneath the Eurasian plate. Currently, only one geothermal power plant is operating in Thailand. It is a 0.3 MW Ormat binary power plant installed in 1989 in the Fang district of Chiang Mai province in northern Thailand (Fig. 1). The plant utilizes 130°C

water encountered in fractured granite at depths of 250–400 m (Ramingwong et al., 2000).

Another prominent area classified by the Thailand Department of Alternative Energy Development and Efficiency (DEDE) is the Mae Chan geothermal field (Raksaskulwong, 2008; Ramingwong et al., 2000), located about 30 km to the north of Chiang Rai province (Fig. 1b). The Mae Chan area along with the survey sites is shown in Fig. 2. The hot springs at Mae Chan are associated with the almost east-west left-lateral strike-slip Mae Chan Fault (Figs. 1b and 2), which extends from the northernmost part of Thailand near the Thailand–Myanmar border through the Mae Chan region to the Mekong River into Laos, a distance of 140 km. The thermal waters at Mae Chan seep into the base of the Mae Chan creek, which is only exposed during the dry season (shown as Y1 and Y4 in Fig. 2). They also form hot pools at Y3a and Y3b (Fig. 2) in which the measured temperatures can reach 99.5°C (Singharajwarapan et al., 2012). In addition, hot springs have been reported near MCH3 (Fig. 2).

The Mae Chan region is located at the boundary between a valley filled with Quaternary alluvium to the east and a Triassic granitic batholith to the west (Fig. 1b). Permian–Triassic rhyolite and ash-flow tuff can be found in the northeastern part of the Mae Chan area, and low-grade metamorphic rocks consisting of phyllite, quartzite, and schist formed during Devonian–Carboniferous time occur in the northwestern part of the area (Fig. 1b). It has been suggested

* Corresponding author. Tel.: +66 2 2015764; fax: +66 2 3547159.
E-mail address: wsiripun@gmail.com (W. Siripunvaraporn).

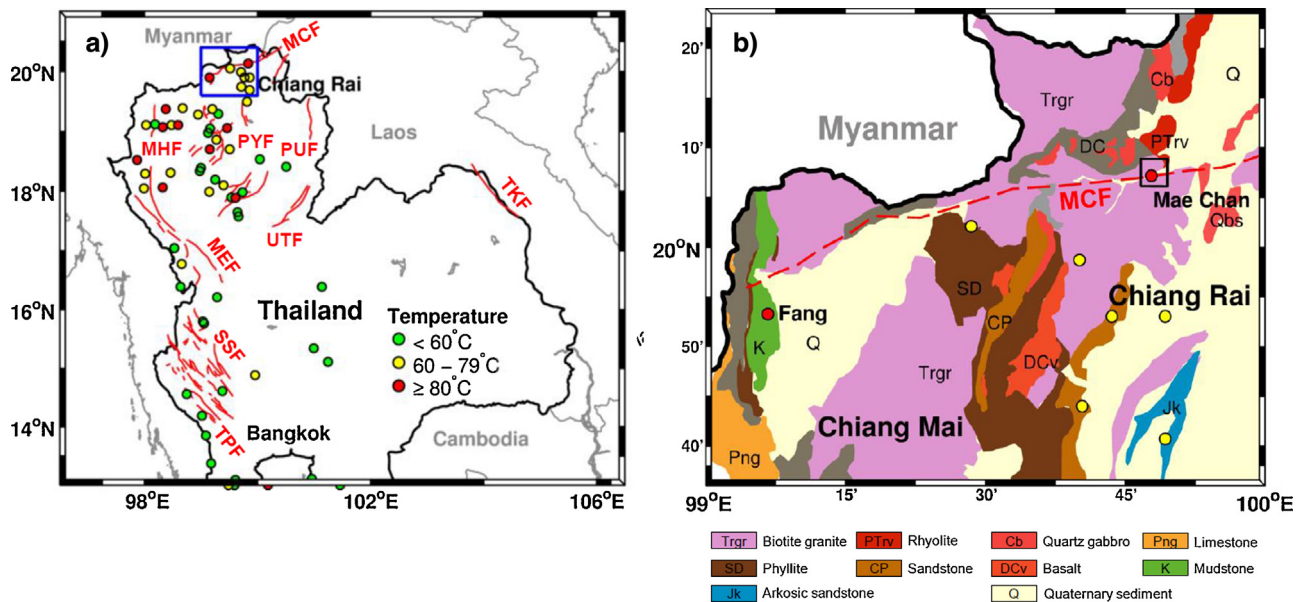


Fig. 1. (a) Locations of hot springs in northern Thailand in which red circles indicate the hot springs whose temperature exceeds 80 °C, yellow circles for temperature between 60 °C and 79 °C, and green for lower than 60 °C (Subtawewung et al., 2005). MCF, MHF, PYF, PUF, UTF, MEF, SSF, TPF, and TKF are for Mae Chan Fault, Mae Hong Son Fault, Pha Yoa Fault, Pua Fault, Uttaradit Fault, Moei Fault, Sri Sawat Fault, Three Pagoda Fault and Tha Khaek, respectively (after Kosuwan et al., 2006). (b) The detailed regional geological map of the blue rectangular block shown in (a). MCF is drawn according to Kosuwan and Lumjuan (1998). The “black” rectangular block indicates the area of the Mae Chan survey of this paper and is shown in detail in Fig. 2. (For interpretation of the references to colour in this figure legend, the reader is referred to the web version of this article.)

that the thermal water forms a shallow reservoir within the weathered, fractured granite and in the sedimentary basin and seeps to the surface through the Mae Chan Fault (Fig. 2). To further investigate the reservoir, vertical electrical sounding (VES) (DEDE, 2005; Thienprasert and Raksakulwong, 1997; Thienprasert, 1980) and seismic refraction surveys (Thienprasert, 1980) including drilled holes (DEDE, 2005; Geotermica Italiana SRI, 1984; Owens, 2012; Thienprasert and Raksakulwong, 1997) were conducted in the Mae Chan valley just near the hot springs (Y2 of Fig. 2). These studies indicated that the subsurface geology near Y2 consisted of a 10–20 m thick clay and sand layer above a 100 m thick weathered and fractured granite layer. At greater depths granite bedrock was encountered.

Even though spring temperatures can reach 99.5 °C (Singharajwarapan et al., 2012), the maximum temperature

reached at a depth of 100 m was 122 °C (Owens, 2012). In 2004, the area (Y2 of Fig. 2) was again drilled to a depth of 56 m to extract the hot fluid. Its temperature at that depth is around 94 °C (DEDE, 2005). The hot water is currently used for spas and drying agricultural products. In the initial assessments of the Mae Chan region, Owens (2012) concluded that the shallow fluids are not hot enough to generate electricity and drilling to depths of 1 km in the granite was not cost-effective. To assess the size of the reservoir without costly drilling, a magnetotelluric (MT) survey was conducted. The MT surveys are widely used in the past decades in geothermal exploration to reveal hydrothermal systems beneath the surface and to help define the drilling locations for the production wells (Heise et al., 2008; Newman et al., 2008). This is because of its major advantage as it is the only method that can directly sense a geothermal reservoir from its electrical resistivity from the surface down to depths of several kilometers (Árnason et al., 2010; Sinharay et al., 2010; Yu and Strack, 2010; Heise et al., 2008; Garg et al., 2007; Santos et al., 2007; Harinarayana et al., 2006; Uchida et al., 2005; Volpi et al., 2003; Lugão et al., 2002; Cumming et al., 2000; Bibby et al., 1995; Sandberg and Hohmann, 1982).

In this paper, we report on the analysis of a pilot MT survey in the Mae Chan area. The objectives of the experiment are to determine the source of the hot fluid and its location, and the size and depth of the reservoir. This information will be used to help determine the potential of the Mae Chan region for geothermal power production. We first describe the acquisition of the magnetotelluric data. Data processing, inversion and interpretation are then discussed.

2. Magnetotelluric survey: data acquisition, data processing and 3-D inversion

In July 2013, high frequency and broadband MT data were acquired at seven sites in a 3 km × 4 km area in the Mae Chan region which included many of the hot springs (Fig. 2). All sites used a KMS-820 data acquisition unit and coils and electrodes from KMS Technologies – KJT Enterprises Inc., Houston, TX, USA. Only the

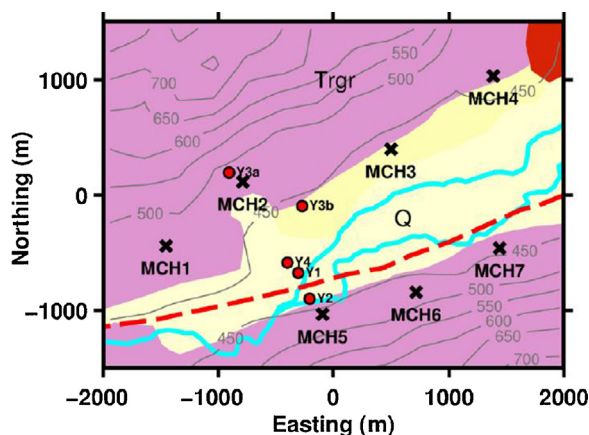


Fig. 2. Locations of seven MT sites (crosses sign) covering an area of 3 km × 4 km in Mae Chan district, Chiang Rai province, Thailand. Geological rock units and topography are plotted as the background on this map. Y1 and Y4 are the hot spring locations found at the river bed. Y2 is the drilled hole (DEDE, 2005), and Y3a and Y3b are the hot springs found at the surface. Additional hot springs are also found around the north of MCH3 but are not shown.

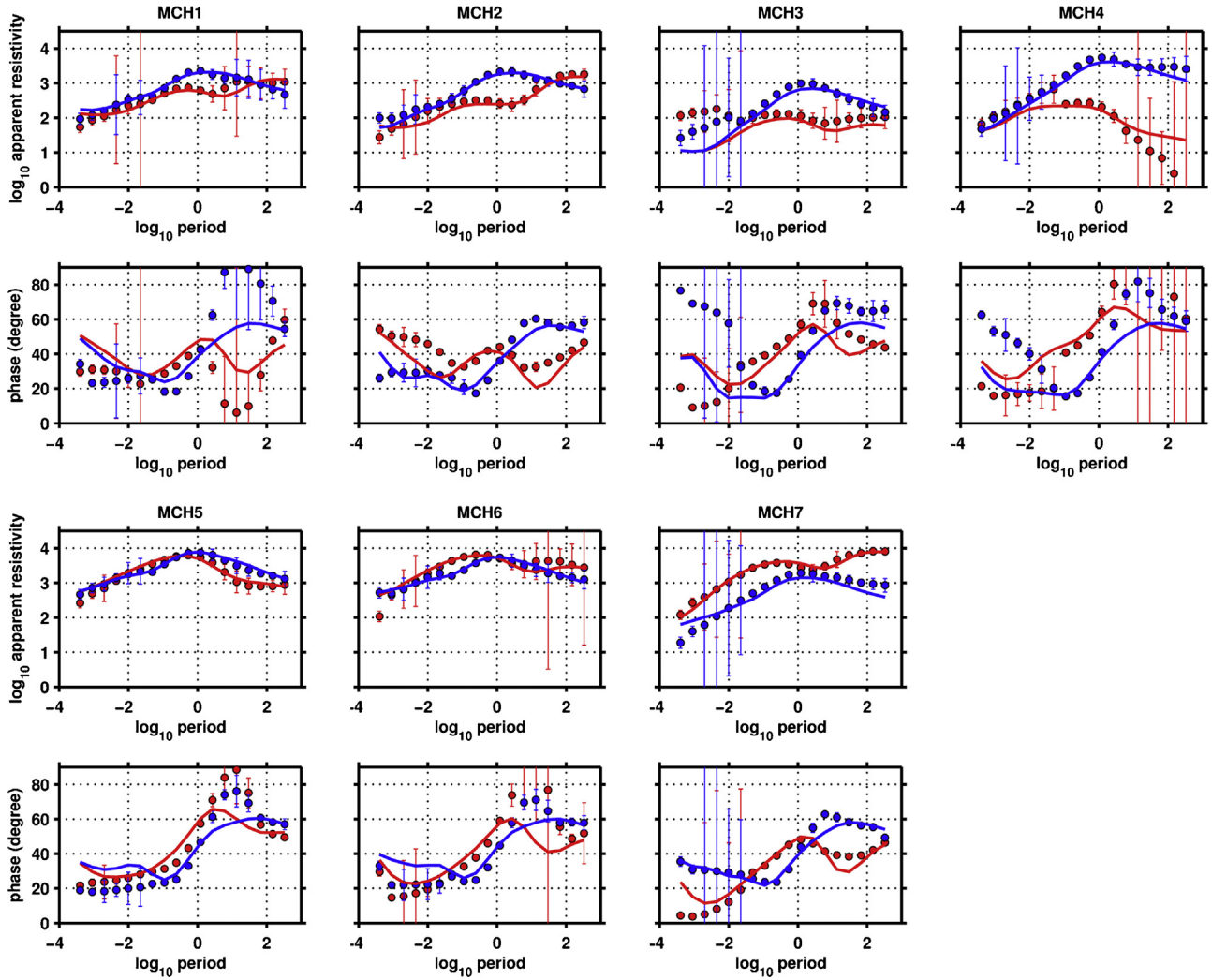


Fig. 3. The apparent resistivities (ohm m) and phases (degree) as a function of \log_{10} periods (second) computed from the off-diagonal impedance tensor at seven locations acquired in the locations shown in Fig. 2. Red is xy and blue is yx mode. The circles and error bars are from field measurement, and the solid lines are the calculated responses generated from the inverted model shown in Figs. 5–7. (For interpretation of the references to colour in this figure legend, the reader is referred to the web version of this article.)

horizontal electric and magnetic fields (E_x , E_y , H_x and H_y) were measured, where x is oriented north and y is oriented east. The electrodes (LEMI-701), broadband magnetic coils (LEMI-120) and the acquisition unit were left overnight to acquire the data for a total of about 20 h at each station (2 h of 1000 Hz sampling rate and 18 h of 250 Hz sampling rate). For the high frequency magnetic fields, the broadband coils LEMI-120 were replaced with the high frequency coils (LEMI-118) and data was acquired 30 min before or after the 20-h measurement using a sampling rate of 10,000 Hz. Both broadband and high frequency data were processed and combined to produce data ranging from 5000 Hz to around 1000 s.

Most of the sites are less than 10 km from the main district of Mae Chan where its population is less than 20,000. Cultural noise from electric cables and telephone poles in villages and resorts can dominate the data in some period ranges. In order to improve the quality of the data, a remote reference site (Gamble et al., 1979) was installed in the Fang district, Chiang Mai province, about 70 km southwest of the survey area. Similar sets of sampling rates were used at the reference site to acquire the broadband data simultaneously with the local sites. Due to the lack of another pair of LEMI-118 high frequency magnetic coils, we could not acquire the high frequency data at the remote reference site. The broadband data from 500 Hz and lower (or longer periods) was

therefore processed with remote reference techniques using KMS processing software based on robust multiple-station processing (Egbert, 1997), while the high frequency data from 5000 Hz to 500 Hz was only locally processed without remote reference data.

Because the high frequency data were not remotely processed and the data quality was poor, the data above 3000 Hz were omitted. Similarly, the data above 300 s are generally contaminated and were also omitted from the inversion process as they also correspond to structures that are deeper than the region of interest. As in other areas around the world, the data in the dead band (periods of 1–100 s) is relatively poor due to low signal. For the inversion, the combined and processed impedance tensor \mathbf{Z} from periods ranging from 3000 Hz to 300 s was selected linearly on a \log_{10} scale to give a total of 18 periods per site. The conversion of the impedance tensor to the apparent resistivity and phase of the xy- and yx- polarizations along with the error bars for each station are shown in Fig. 3.

The parallel version of WSINV3DMT (Siripunvaraporn and Egbert, 2009; Siripunvaraporn et al., 2005) was used to invert the selected impedance tensor \mathbf{Z} . The code has been widely used in many geothermal explorations (Árnason et al., 2010; Bertrand et al., 2013; Ghaedrahmati et al., 2013; Heise et al., 2008; Patro and Egbert, 2011; Tuncer et al., 2006). One major advantage of directly performing the 3-D inversion is that there is no requirement to

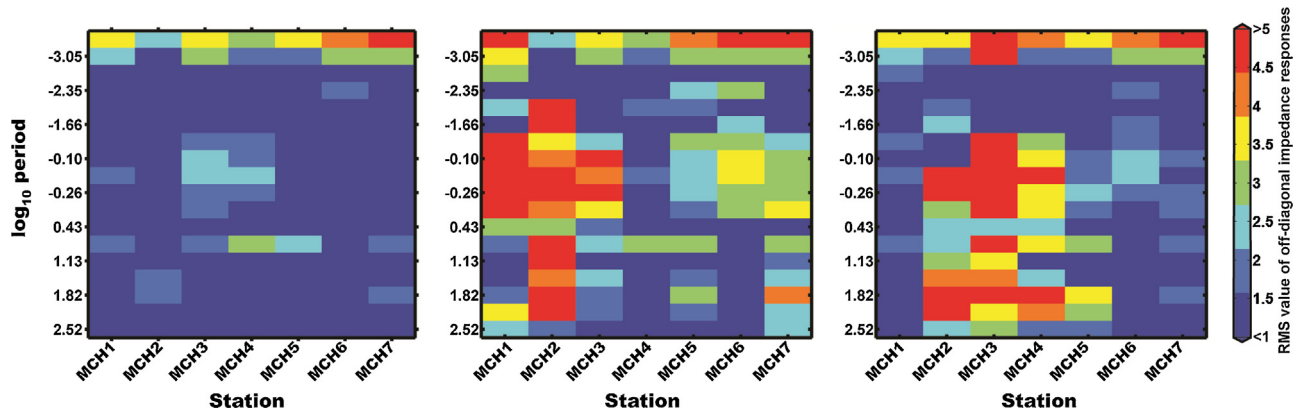


Fig. 4. RMS misfit maps show the misfit between the observed data and the calculated data of each site as a function of period. The calculated data are obtained (a) from the inverted model shown in Fig. 5; (b) by replacing the C1 conductor of Fig. 5 with a 300 Ω m zone; and (c) by replacing the C2 conductor of Fig. 5 with a 300 Ω m zone.

conduct the dimensionality analysis (Siripunvaraporn, 2012). Since Z_{xx} and Z_{yy} are more severely distorted, only the off-diagonal data, Z_{xy} and Z_{yx} , were used for the 3-D inversion to reduce the risk of producing artifacts in the inverted model. The minimum error floor was set at 5% of the $|Z_{xy}Z_{yx}|^{1/2}$. For the outliers, the error bars were increased to be large enough relative to the neighboring data. The area with topography was discretized into a $49 \times 52 \times 67$ grid in north-south, east-west and depth, respectively. For the vertical mesh, the first layer is discretized at 30 m to provide high accuracy responses for all data. The thickness of the subsequent layers increases by 1.5–1.8 times of the previous layers. The horizontal grid sizes in the survey region are 200 m on both directions. The model mesh outside of the investigation area was extended using a logarithmic scale to avoid boundary effects.

The inversion was run multiple times with different starting parameters. The preferred inversion result was obtained by using a 300 Ω m half-space as the initial model to produce the normalized RMS misfit of about 4.6. After 4 iterations, the misfit level decreased to about 1.6 RMS. This step was run with a larger length-scale parameter in the WSINV3DMT code (Siripunvaraporn et al., 2005; Siripunvaraporn and Egbert, 2009) to model the large scale structures that are required by the observed data. To further decrease the RMS level, a smaller length-scale was therefore used to allow the smaller features required by the data to be added in the inverted model, as with the techniques used in Boonchaisuk et al. (2013). The reduced length-scale inversion step also helps to fit the data that are affected by static distortion (Siripunvaraporn, 2012). After 2 more iterations of the inversion, this time starting from the previous model but with smaller length scale, the misfit level was stabilized at 1.5 RMS. At that point, we terminated the inversion. The observed data and the calculated responses from all 7 stations are shown in Fig. 3. The RMS misfits for each site and each period for this run are shown in Fig. 4a. The final inversion model is plotted in a plan view in Fig. 5 and in cross-sections in Figs. 6 and 7.

Three main features are shown in Figs. 5–7: the conductive zones C1 and C2 and the resistive structure labeled as R. All of these features also appear in other models with different inversion parameters inferring that they are required by the data. The conductor C1 is surrounded with MCH1, MCH2, MCH3, MCH5 and MCH6 sites, while conductor C2 is only enclosed by MCH2, MCH3 and MCH4 sites on just its southern side. The size and thickness of C2 might therefore be less constrained than those of C1. More stations located on the northern side may be necessary in order to further constrain C2. The conductive zones C1 and C2 are of particular interest because they can be linked to the geothermal reservoir discussed in the following section. We therefore do the feasibility tests in order to validate that C1 and C2 are required by the observed data.

To verify the existence of C1, the conductive volume C1 of the inverted model in Figs. 5–7 was replaced by a background resistivity of 300 Ω m and ran the forward modeling to fit the observed data. We found that the overall RMS dramatically increased to 3.4 indicating a poorer fit to the observed data. A similar experiment was conducted with the C2 zone. After the forward modeling run of the model without the C2 conductive zone, the overall RMS misfit increased to 3.1. Both of these experiments indicate us that both conductive C1 and C2 zones are required by the observed data. For a detailed investigation, Fig. 4b and c shows the RMS misfit of each site and each period after replacing C1 and C2, respectively, with a background resistivity of 300 Ω m. Fig. 4b shows that C1 is required by most sites, particularly MCH1, MCH2 and MCH3 as removing it results in a higher RMS misfit. The period range that senses conductor C1 is around 0.03–10 s. Fig. 4c shows that conductor C2 is required by MCH2, MCH3 and MCH4. The period range affecting C2 is slightly larger (around 0.03–100 s), which might be why C2 is interpreted to be thicker and deeper than C1.

3. Interpretation and discussion

The previous section shows that the final inverted model (Figs. 5–7) contains three prominent features: the shallow conductive zones, C1 and C2, the resistive structure, R, and the resistivity contrast between the conductive zones and the resistive block matches the Mae Chan Fault well (drawn as the dashed line in Fig. 5). In this section, we link these prominent features with the geology of the area.

The two conductive zones C1 and C2 form a thin conductive layer near the surface covering the Mae Chan valley (Fig. 5a) but separate into two zones below 50 m depth (e.g., Figs. 5b and 6a). C1 conductor dissipates at around 250 m while C2 continues to a depth of 500 m (Fig. 6a). C2 covers a larger area (around 1 km²). C1 and C2 are located within the Quaternary alluvium. The center of C1 is close to where the hot springs seep into the Mae Chan creek (indicated by Y1 and Y4 in Fig. 5) and also the drilled hole (indicated by Y2), while the center of C2 is associated with hot fluid emerging at the surface. Two hot springs (Y3a and Y3b) are also found between C1 and C2. Since there is a correlation between the hot springs and the conductors beneath, we can therefore suggest that C1 and C2 are reservoirs for the hot fluid. The reservoirs are connected in the top sedimentary deposits in the north of MCF (Figs. 5a, 6 and 7). They become separated on entering the weathered and fractured granite below (Figs. 6 and 7).

The resistor R appears in the southern region near stations MCH5, MCH6 and MCH7 (Fig. 5). It extends from surface to cover the entire survey area at a greater depth as clearly displayed in

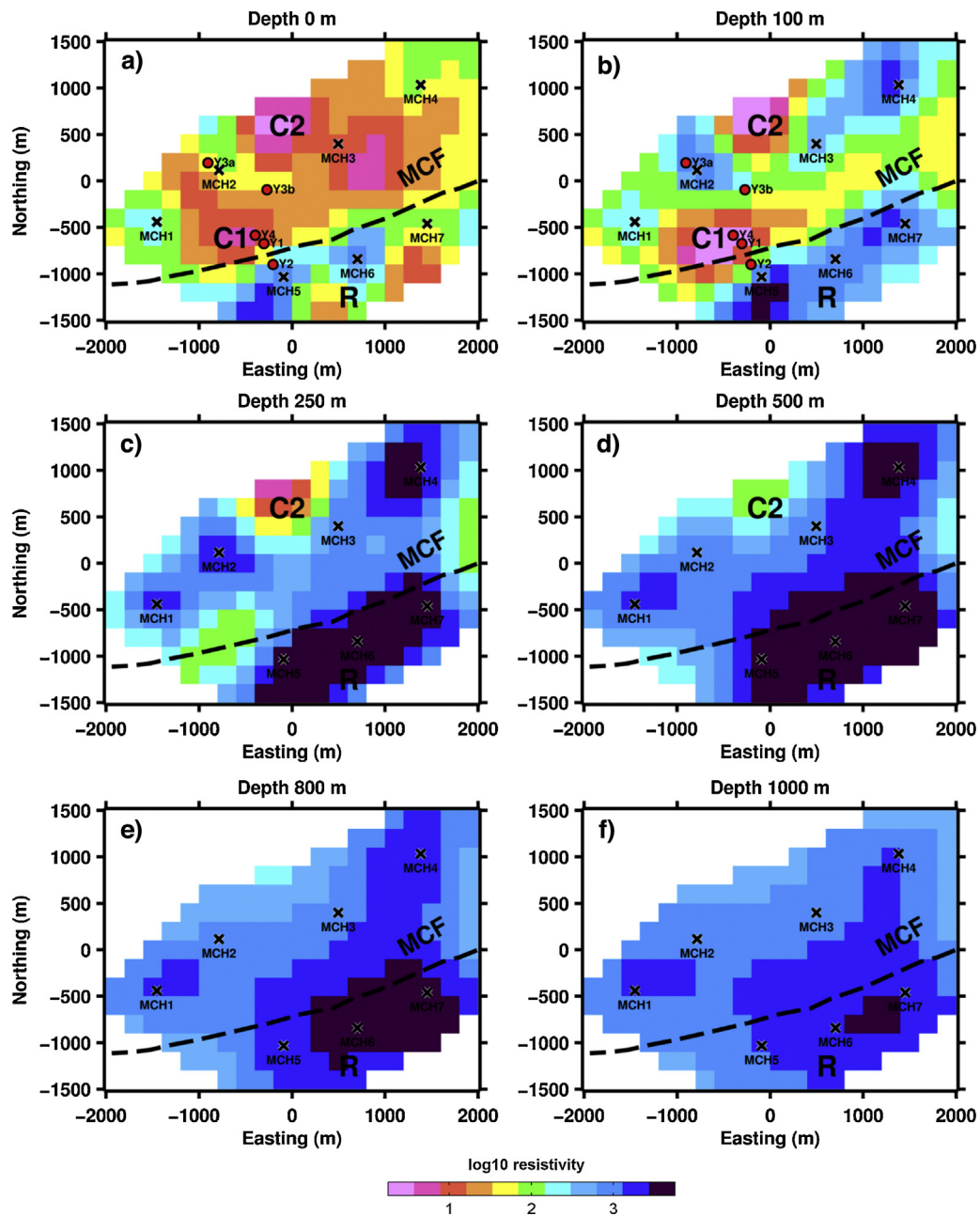


Fig. 5. The plane-view of the final inverted model at (a) surface, (b) 100 m, (c) 250 m, (d) 500 m, (e) 800 m and (f) 1000 m depths. MT locations and their name are marked as crosses. Mae Chan Fault (MCF) is drawn as a dashed line. C1 and C2 are the two conductive zones while R is the resistivity zone. They are only marked where they appear in the model.

Figs. 6 and 7. According to prior geological information (Kosuwat and Lumjuan, 1998) and the surface geology map (Fig. 1b), the resistive body R corresponds to the batholith Triassic granite. As its value is moderately high, 1000–3000 Ω m, it is interpreted as being unweathered granite. In the north, part of the weathered and fractured granite along with the sedimentary layer is interpreted to be filled with the hot fluid, which produces the low resistivity zones C1 and C2 (Fig. 5). As with other non-volcanic geothermal systems in granitic rocks (Gianelli et al., 1997; Harinarayana et al., 2006; Newman et al., 2008; Santos, 1997; Uchida et al., 2005), the heat source for the hot fluid in the Mae Chan region should come from the batholith granite R at great depth. When the rain water infiltrates into the ground, the ground water is heated by the hotter batholith resulting from the decay of radioactive elements of

the minerals in the granite. The hot water then rises to the surface along faults and fractures.

Using the resistivity curve versus temperature developed for two granite bodies in Japan (Llera et al., 1990), we can roughly estimate the temperature of the granite in our area where its mean resistivity is 1000 Ω m in the upper 5 km depth to be around 130 °C. Although the granite in our area is different in composition than the granite described by Llera et al. (1990), the estimated temperature value of 130 °C agrees well with temperatures of 122 °C and 127 °C calculated using the chalcedony and K-Mg geothermometers (Singharajwarapan et al., 2012). In addition, the resistivity of the hot granite tends to decrease at depth of more than 5 km. A decrease in resistivity may correspond to an increase in temperature as reported in many publications (Akpan et al., 2013; Árnason

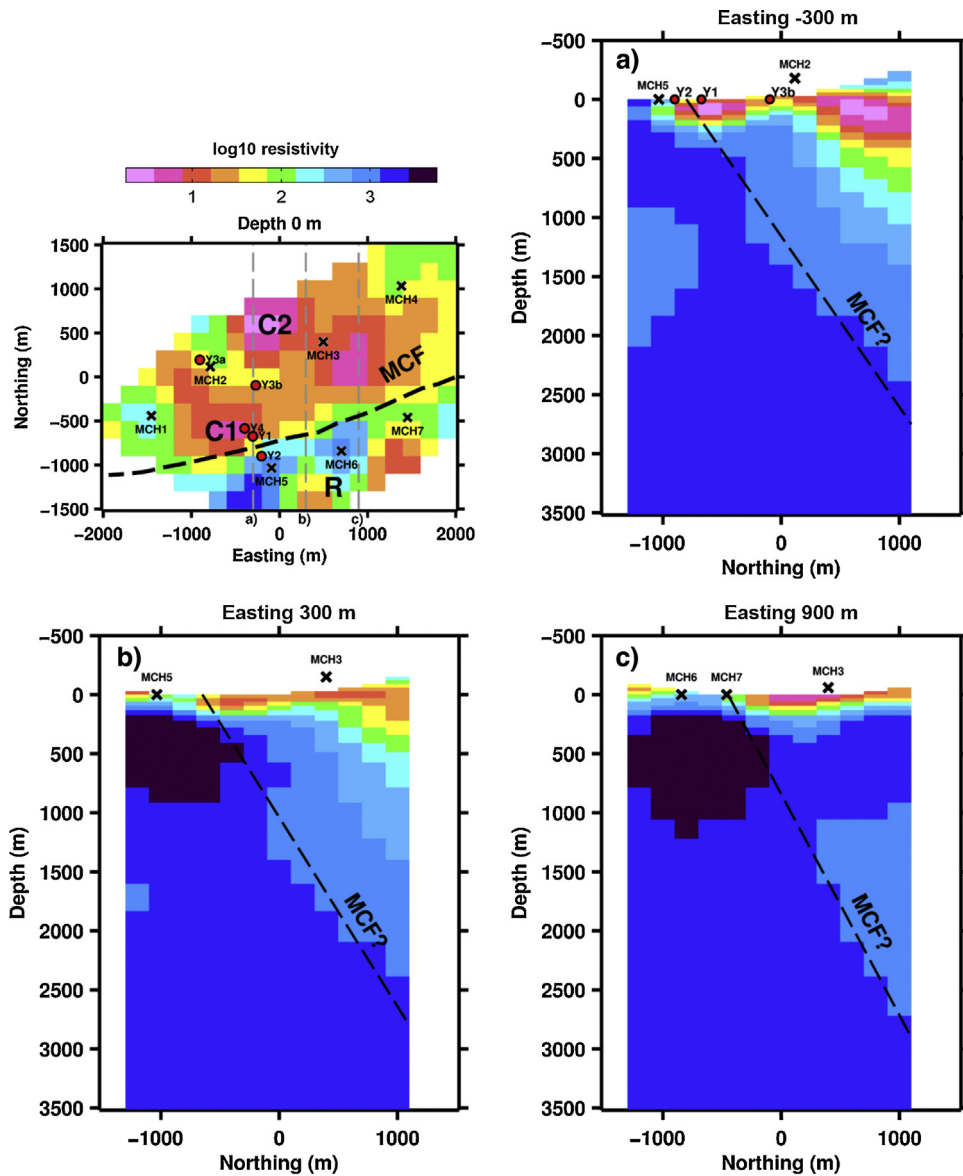


Fig. 6. North-south cross-section of the final inverted model (Fig. 5a) at east-west distances of (a) –300 m, (b) 300 m and (c) 900 m. The dashed line is the estimated orientation of the Mae Chan Fault (MCF). Locations of the MT stations are also mapped and shown at the surface along with the hot spring locations.

et al., 2010; Harinarayana et al., 2006; Nover, 2005; Llera et al., 1990; Olhoeft, 1981; Shankland and Ander, 1983).

Another feature that can be observed in our inverted model is the resistivity contrast between the conductive features C1 and C2 in the north and the resistive zone R in the south which is oriented in the northwest-southeast direction. The location of the abrupt change of the resistivity occurs at the Mae Chan Fault mapped by Kosuwan and Lumjuan (1998). The contrast is therefore interpreted as the fault line cutting through the granite in the middle of the survey area. The contrast vanishes at depth as shown in the cross-sections of Fig. 6a–c. By following the resistivity contrast from the fault trace at the surface (Fig. 2) to greater depths (Fig. 6a–c), we can infer that the Mae Chan Fault dips at 40–60° which is not as steep as expected (Fenton et al., 2003; Kosuwan and Lumjuan, 1998). Its hanging wall is in the north and consists of a sedimentary deposit and weathered and fractured granite on top of the unweathered granite. The foot wall is in the south and consists of mostly batholith granite. Below 2 km, both sides of the fault have the same resistivity suggesting granite forms both sides of the fault. Further detailed surveys with MT stations closer than the current

spacing of 1 km are needed to better define the fault location at depth.

This study helps confirm the study of Owens (2012) that the heat source for the Mae Chan hot springs is the hot granite. The reservoir is located within the first few hundred meters from the surface in the sedimentary deposits and weathered and fractured granite. Based on our study, the hot fluid in the C1 conductor can be considered as a potential area to develop a small-scale binary geothermal power plant similar to the 300 kW plant in the Fang district or a novel low enthalpy binary geothermal power plant (Gabbriellini, 2012). However, the reservoir appears relatively small. A lack of balance between usage and re-injection could distort the shallow hydrology of the area (Heise et al., 2008). The C2 conductor should be drilled to determine if the temperature of the hot fluid is high enough for development.

A larger scale geothermal power plant using the hot granite at a great depth is also possible. However, little is known about the granite at depth. This would require further measurements as our first phase of the MT survey covered only 10 km² which is a small part of the whole batholith exposed at the surface. Expanding the

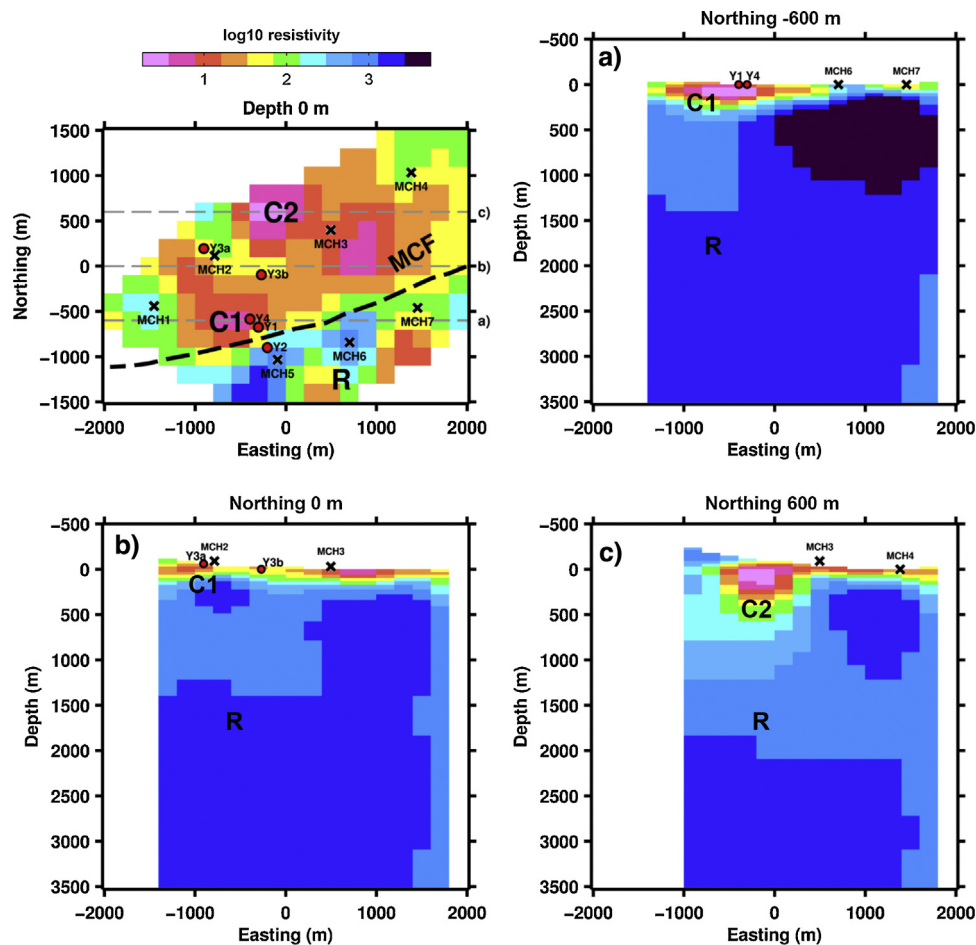


Fig. 7. East-west cross-section of the final inverted model (Fig. 5a) at north-south distances of (a) –600 m, (b) 0 m and (c) 600 m. Locations of the MT stations are also mapped and shown at the surface along with the hot spring locations.

MT site coverage to a larger scale may show the existence of permeable fractured granite at great depth which could be used for geothermal power. A combination with thermal gradient drilling would require assessing the granite potential.

4. Conclusion

A 3-D resistivity structure determined from a small number of MT stations sparsely distributed around the Mae Chan geothermal area provides very useful information to assess the potential for a geothermal power plant. In the Mae Chan hydrothermal system, hot fluid heated from the deeper granitic batholith, identified as high resistivity feature R, is stored in the fractured and weathered granite and the sedimentary rock indicated by two conductive zones C1 and C2. A fracture in the damaged zone of the fault (shown as a resistivity contrast) allows the pressurized hot fluid to reach the surface. Since the temperature of the Mae Chan hydrothermal system does not seem to be high, we propose the development of small-scale geothermal power plants over the two zones C1 and C2. Further detailed investigation with more MT coverage along with deep well drilling may be necessary in order to assess the potential to build a larger scale geothermal power plant in the area.

Acknowledgements

The authors would like to thank the Thailand Research Fund (RSA5780010) and the Thailand Department of Energy Development and Efficiency (DEDE) for the support and permission

to publish this study. We would like to thank Miss. Patchawee Nuallkhow for her dedicated participation during the field work. Mr. Puwis Amatyakul would like to thank the Development and Promotion of Science Talents project (DPST) for a scholarship. The authors appreciate the suggestions and collaboration of Mr. Suebsak Solkosoom, Mr. Tawan Sukho and Mr. Adisak Choosuk. We also would like to thank Dr. Kurt Strack of KMS technologies – KJT Enterprises Inc. for the MT instruments used in the field survey. The comments of an anonymous reviewer, Dr. Erika Gasperikova and the Editor are greatly appreciated.

References

- Akpan, A.E., Narayanan, M., Harinarayana, T., 2013. Estimation of subsurface temperatures in the Tattapani geothermal field, central India from limited volume of magnetotelluric data and borehole thermograms using a constructive back-propagation neural network. *Earth Interact.*, <http://dx.doi.org/10.1175/2013EI000539.1> (in press).
- Árnason, K., Eysteinnsson, H., Hersir, G.P., 2010. Joint 1D inversion of TEM and MT data and 3D inversion of MT data in the Hengill area, SW Iceland. *Geothermics* 39, 13–34. <http://dx.doi.org/10.1016/j.geothermics.2010.01.002>.
- Barr, S.M., Ratanasathien, B., Breen, D., Ramingwong, T., Sertsrivanit, S., 1979. Hot springs and geothermal gradients in northern Thailand. *Geothermics* 8, 85–95. [http://dx.doi.org/10.1016/0375-6505\(79\)90002-6](http://dx.doi.org/10.1016/0375-6505(79)90002-6).
- Bertrand, E., Caldwell, T.G., Hill, G.J., Bennie, S.L., 2013. 3-D inversion of a 200+ site magnetotelluric array for deep geothermal exploration. In: *5th International Symposium on Three-Dimensional Electromagnetics*, Sapporo, Japan, May 7–9, 2013, p. 3.
- Bibby, H.M., Caldwell, T.G., Davey, F.J., Webb, T.H., 1995. Geophysical evidence on the structure of the Taupo volcanic zone and its hydrothermal circulation. *J. Volcanol. Geotherm. Res.* 68, 29–58. [http://dx.doi.org/10.1016/0377-0273\(95\)00007-H](http://dx.doi.org/10.1016/0377-0273(95)00007-H).

- Boonchaisuk, S., Siripunvaraporn, W., Ogawa, Y., 2013. Evidence for middle Triassic to Miocene dual subduction zones beneath the Shan-Thai terrane, western Thailand from magnetotelluric data. *Gondwana Res.* 23, 1607–1616.
- Cumming, W., Nordquist, G., Astra, D., 2000. Geophysical exploration for geothermal resources: an application for combined MT-TDEM. In: *Society of Exploration Geophysicists Annual Meeting Technical Program Expanded Abstracts*, 6–11 August, Calgary, Canada, pp. 1071–1074.
- Chuaviroj, S., 1988. Geothermal development in Thailand. *Geothermics* 17, 421–428, [http://dx.doi.org/10.1016/0375-6505\(88\)90071-5](http://dx.doi.org/10.1016/0375-6505(88)90071-5).
- DEDE (Thailand Department of Alternative Energy Development and Efficiency), 2005. Hot Spring Development Project at Mae Chan – Chiang Rai. DEDE, pp. 177. Available at: <http://www3.dede.go.th/dede/fileadmin/upload/pic-tures.eng/Webpage-MaeChan-HotSpring.pdf>
- Egbert, G.D., 1997. Robust multiple-station magnetotelluric data processing. *Geophys. J. Int.* 130, 475–496, <http://dx.doi.org/10.1111/j.1365-246X.1997.tb05663.x>.
- Fenton, C., Charusiri, P., Wood, S., Boise, I., 2003. Recent paleoseismic investigations in Northern and Western Thailand. *Ann. Geophys.* 46, 957–981, <http://dx.doi.org/10.4401/ag-3464>.
- Gabbriellini, R., 2012. A novel design approach for small scale low enthalpy binary geothermal power plants. *Energy Convers. Manag.* 64, 263–272, <http://dx.doi.org/10.1016/j.enconman.2012.04.017>.
- Gamble, T.D., Goubau, W.M., Clarke, J., 1979. Magnetotellurics with a remote magnetic reference. *Geophysics* 44, 53–68, <http://dx.doi.org/10.1190/1.1440923>.
- Garg, S.K., Pritchett, J.W., Wannamaker, P.E., Combs, J., 2007. Characterization of geothermal reservoirs with electrical surveys: beowawe geothermal field. *Geothermics* 36, 487–517, <http://dx.doi.org/10.1016/j.geothermics.2007.07.005>.
- Geotermica Italiana SRI, 1984. *Geothermal Reconnaissance Survey of Northern Thailand-Final Report, Geology, Pisa, Italy*, pp. 86 (unpublished report).
- Ghaedrahmati, R., Moradzadeh, A., Fathianpour, N., Lee, S.K., Porkhial, S., 2013. 3-D inversion of MT data from the Sabalan geothermal field, Ardabil, Iran. *J. Appl. Geophys.* 93, 12–24, <http://dx.doi.org/10.1016/j.jappgeo.2013.03.006>.
- Gianelli, G., Manzella, A., Puxeddu, M., 1997. Crustal models of the geothermal areas of southern Tuscany (Italy). *Tectonophysics* 281, 221–239, [http://dx.doi.org/10.1016/S0040-1951\(97\)00101-7](http://dx.doi.org/10.1016/S0040-1951(97)00101-7).
- Harinarayana, T., Abdul Azeed, K.K.K., Murthy, D.N.N., Veeraswamy, K., Eknath Rao, S.P.P., Manoj, C., Naganjaneyulu, K., 2006. Exploration of geothermal structure in Puga geothermal field, Ladakh Himalayas, India by magnetotelluric studies. *J. Appl. Geophys.* 58, 280–295, <http://dx.doi.org/10.1016/j.jappgeo.2005.05.005>.
- Heise, W., Caldwell, T.G., Bibby, H.M., Bannister, S.C., 2008. Three-dimensional modelling of magnetotelluric data from the Rotokawa geothermal field, Taupo Volcanic Zone. *N. Z. Geophys. J. Int.* 173, 740–750, <http://dx.doi.org/10.1111/j.1365-246X.2008.03737.x>.
- Kosuwan, S., Lumjuan, A., 1998. *Neotectonics of Mae Chan Fault in Mae Chan district, Chiang Rai Province*. Department of Mineral Resources, pp. 56.
- Kosuwan, S., Takashima, I., Charusiri, P., 2006. Active Fault Zones in Thailand [WWW Document]. Department of Mineral Resources, <http://www.dmr.go.th/main.php?filename=fault.En>
- Llera, F., Sato, M., Nakatsuka, K., Yokoyama, H., 1990. Temperature dependence of the electrical resistivity of water-saturated rocks. *Geophysics* 55, 576–585.
- Lugão, P.P., LaTerra, E.F., Kriegshäuser, B., Fontes, S.L., 2002. Magnetotelluric studies of the Caldas Novas geothermal reservoir. *Braz. J. Appl. Geophys.* 49, 33–46, <http://dx.doi.org/10.1190/1.1442869>.
- Newman, G.A., Gasperikova, E., Hoversten, G.M., Wannamaker, P.E., 2008. Three-dimensional magnetotelluric characterization of the Coso geothermal field. *Geothermics* 37, 369–399, <http://dx.doi.org/10.1016/j.geothermics.2008.02.006>.
- Nover, G., 2005. Electrical properties of crustal and mantle rocks – a review of laboratory measurements and their explanation. *Surv. Geophys.* 26, 593–651, <http://dx.doi.org/10.1007/s10712-005-1759-6>.
- Olhoeft, G., 1981. Electrical properties of granite with implications for the lower crust. *J. Geophys. Res.* 86, 931–936, <http://dx.doi.org/10.1029/JB086iB02p00931>.
- Owens, L., 2012. *Initial Assessments of High Potential Geothermal Sites in Northern Thailand*. Ormat Technologies, Inc., NV, USA, pp. 8 (unpublished report).
- Patro, P.K., Egbert, G.D., 2011. Application of 3D inversion to magnetotelluric profile data from the Deccan Volcanic Province of Western India. *Phys. Earth Planet. Inter.* 187, 33–46, <http://dx.doi.org/10.1016/j.pepi.2011.04.005>.
- Raksaskulwong, M., 2008. Thailand geothermal energy: development history and current status. In: *Proceedings of the 8th Asian Geothermal Symposium*, pp. 39–46.
- Ramingwong, T., Lertsrimongkol, S., Asnachinda, P., Prasertvigai, S., 2000. Update on Thailand geothermal energy research and development. In: *World Geothermal Congress*, pp. 377–386.
- Sandberg, S., Hohmann, G., 1982. Controlled-source audiomagnetotellurics in geothermal exploration. *Geophysics* 47, 100–116, <http://dx.doi.org/10.2172/6749290>.
- Santos, F.M., Afonso, A.R.A., Dupis, A., 2007. 2D joint inversion of dc and scalar audio-magnetotelluric data in the evaluation of low enthalpy geothermal fields. *J. Geophys. Eng.* 4, 53–62, <http://dx.doi.org/10.1088/1742-2132/4/1/007>.
- Santos, F.M., 1997. Study of the Chaves geothermal field using 3D resistivity modeling. *J. Appl. Geophys.* 37, 85–102, [http://dx.doi.org/10.1016/S0926-9851\(97\)00010-4](http://dx.doi.org/10.1016/S0926-9851(97)00010-4).
- Shankland, T.J., Ander, M.E., 1983. Electrical conductivity, temperatures, and fluids in the lower crust. *J. Geophys. Res.* 88, 9475, <http://dx.doi.org/10.1029/JB088iB11p09475>.
- Singharajwarapan, F.S., Wood, S.H., Prommakorn, N., Owens, L., 2012. Northern Thailand geothermal resources and development: a review and 2012 update. *GRC Trans.* 36, 787–791.
- Sinharay, R.K.R., Srivastava, S., Bhattacharya, B.B.B., 2010. Audiomagnetotelluric studies to trace the hydrological system of thermal fluid flow of Bakreswar Hot Spring, Eastern India: a case history. *Geophysics* 75, B187–B195, <http://dx.doi.org/10.1190/1.3431532>.
- Siripunvaraporn, W., 2012. Three-dimensional magnetotelluric inversion: an introductory guide for developers and users. *Surv. Geophys.* 33, 5–27, <http://dx.doi.org/10.1007/s10712-011-9122-6>.
- Siripunvaraporn, W., Egbert, G., 2009. W3INV3DMT: vertical magnetic field transfer function inversion and parallel implementation. *Phys. Earth Planet. Inter.* 173, 317–329, <http://dx.doi.org/10.1016/j.pepi.2009.01.013>.
- Siripunvaraporn, W., Egbert, G., Lenbury, Y., Uyeshima, M., 2005. Three-dimensional magnetotelluric inversion: data-space method. *Phys. Earth Planet. Inter.* 150, 3–14, <http://dx.doi.org/10.1016/j.pepi.2004.08.023>.
- Subtavewong, P., Raksaskulwong, M., Tulyatid, J., 2005. The characteristic and classification of hot springs in Thailand. In: *Proceedings World Geothermal Congress*, p. 7.
- Thienprasert, A., 1980. *Mae Chan Geothermal Energy Resource, Geophysical Investigations Resistivity Method, Seismic Refraction Method and One meter Depth Temperature Reading Method*. Department of Mineral Resources, pp. 68.
- Thienprasert, A., Raksaskulwong, M., 1997. Resistivity and Heat Flow Studies at Mae Chan Geothermal Area, Chiangrai Province. Department of Mineral Resources, pp. 12 (online) library.dmr.go.th.
- Tuncer, V., Unsworth, M., Siripunvaraporn, W., Craven, J., 2006. Exploration for unconformity-type uranium deposits with audiomagnetotelluric data: a case study from the McArthur River mine, Saskatchewan, Canada. *Geophysics* 71, B201–B209, <http://dx.doi.org/10.1190/1.2348780>.
- Uchida, T., Song, Y., Lee, T., 2005. Magnetotelluric survey in an extremely noisy environment at the Pohang low-enthalpy geothermal area, Korea. In: *Proceedings World Geothermal Congress*, pp. 24–29.
- Volpi, G., Manzella, A., Fiordelisi, A., 2003. Investigation of geothermal structures by magnetotellurics (MT): an example from the Mt. Amiata area, Italy. *Geothermics* 32, 131–145.
- Yu, G., Strack, K., 2010. Integrated MT/Gravity geothermal exploration in Hungary: a success story. In: *21st ASEG Conference and Exhibition, Sydney, Australia*, p. 3.

ภาคผนวก ง. Reprint of the revised version

- Songkhun Boonchaisuk, Sutthipong Noisagool, Puwis Amatyakul, Tawat Rung-arunwan, Chatchai Vachiratienchai, and **Weerachai Siripunvaraporn**, 2017, 3-D magnetotelluric imaging of the Phayao Fault Zone, northern Thailand: evidence for saline fluid in the source region of the 2014 Chiang Rai earthquake, *moderate revision* for Journal of Asian Earth Sciences. (IF2015 = 2.647)

3-D magnetotelluric imaging of the Phayao Fault Zone, Northern Thailand: evidence for saline fluid in the source region of the 2014 Chiang Rai earthquake

Songkhun Boonchaisuk^a, Sutthipong Noisagool^{b,e}, Puwis Amatyakul^b, Tawat Rung-Arunwan^c, Chatchai Vachiratienchai^c and Weerachai Siripunvaraporn^{b,d,*}

^aGeoscience Program, Mahidol University, Kanchanaburi Campus, Saiyok, Kanchanaburi, Thailand.

^bDepartment of Physics, Faculty of Science, Mahidol University, 272 Rama 6 Road, Rachatawee, Bangkok, Thailand.

^cCurl-E Geophysics Co., Ltd., 85/87 Nantawan Village, Uttayan-Aksa Road, Salaya, Phutthamonthon, Nakornpathom, Thailand. 73170.

^dThEP Center, Commission on Higher Education, 328, Si Ayutthaya Road, Rachatawee, Bangkok, Thailand.

^eEarthquake Research Institute, University of Tokyo, 1-1-1 Yayoi, Bunkyo-ku, Tokyo, Japan.

*Corresponding author. Tel.: + 66 2 2015764; fax: + 66 2 3547159.

Email address: wsiripun@gmail.com (W. Siripunvaraporn).

Abstract

Seismicity in Thailand had been relatively low for decades prior to the Mw 6.5 earthquake of 5 May 2014 which came as a surprise and was followed by thousands of aftershocks. Most of the epicenters were located in the transition region between the Mae Lao Segment (MLS) and the Pan Segment (PS) of the Phayao Fault Zone (PFZ). We conducted a 3-D magnetotelluric (MT) survey (31 sites) to image the deep PFZ structure. The shallow 3-D resistivity structure matches very well with the surface geology, while the deeper structures disclose many interesting resistive and conductive anomalies. However, the most interesting feature of this study is the large conductive anomaly (ML) located at a depth of 4 km to the mid-crust beneath the MLS just near the seismogenic zone. Our current hypothesis is that the ML conductor has a highly interconnected aqueous fluid content and also plays crucial role in the earthquake sequence of the 5 May 2014 event. As our previous seismic waveform study revealed that the MLS has a relatively high fault plane instability, the fluid within the fractured fault would further reduce the fault strength. The accumulated pre-existing tectonic stress from the north can therefore overcome the maximum frictional strength of the MLS, and hence cause it to slip and so produce the main shock. With the local structural heterogeneities and fluid in the fractured fault zones,

the aftershocks then occurred on both the PS and MLS. This is in contrast to the Mae Chan Fault Zone (MCFZ) in the north which many scientists expected to generate a larger magnitude earthquake than any other faults. Since instrumental record, it has only generated a few Mw 4 earthquakes. Some of our MT stations were located within the MCFZ. However, there is no deep conductor as the conductor lies beneath the MLS. A lack of interconnected fluid within the deep fault beneath the MCFZ might be one reason for the lower seismic activity from the MCFZ. Other geophysical methods, such as seismic tomography, are necessary in order to confirm the presence of the fluid beneath the MLS and also the lack of a deep conductor beneath the MCFZ.

Key words: magnetotelluric; Northern Thailand; earthquake; fluid; Phayao Fault Zone

1. Introduction

Most of the seismicity in Thailand is localized in the north as there are many fault zones that cut through the region (Fig. 1a). The number and magnitude of earthquakes is generally lower than neighboring countries like Myanmar. Nevertheless, an unexpected moderate earthquake occurred on 5 May 2014 in Pan District, Chiang Rai province, northern Thailand (Fig. 1a and 1b) with thousands of aftershocks (Fig. 1b). The local magnitude (M_l) of the main shock was reported as 6.3 by the Thai Meteorological Department (TMD) with a hypocenter depth of 7 km, but later regional moment tensor inversion studies by Noisagool et al. (2016) suggested M_w 6.5 with a depth of 14 km. The main event was the largest earthquake in Thailand since the installation of the seismometer in 1974. The epicenters of the main shock and aftershocks were mostly in the Phayao Fault Zone (PFZ, Fig. 1b) which runs from south to north and is clearly separated into three major segments (Fig. 1b; Uttamo et al., 2003; DMR, 2007; and DMR, 2014). The two segments involved with the recent events are the left-lateral strike-slip Mae Lao Segment (MLS) and the right lateral strike-slip Pan Segment (PS) (Fig. 1b). Interestingly, most of the epicenters are in the transition area between the MLS and the PS (Fig. 1b). The focal mechanisms (Noisagool et al., 2016) of most events ($M_l > 4$) indicate strike-slip motions in agreement with the characteristics of these fault segments.

It is interesting that the second largest recent earthquake in northern Thailand (M_l 5.2, 15 km depth, on 11 September 1994; USGS) also occurred in the PFZ (Fig. 1b). The focal mechanism of this earthquake was the normal motion (ISC, 2012; Fig. 1b). However, Noisagool et al. (2016) pointed out that its focal mechanism should be similar to the main event of the 5 May 2014. In fact, its epicenter is still in doubt as in 1994 there were no seismometers installed nearby. Since the PFZ is classified as a tentatively active fault (Charusiri et al., 1999) due to the lack of the data, even with the 1994 event (M_5) and a few M_4 events between 1994 and 2014 in this area, no scientists expected the PFZ to have enough energy to rupture and produce a M_w 6.5 earthquake so soon. This might be because of its very slow slip rate of about 0.1 mm/yr (Fenton et al., 2003), and relatively short length (45 km). In addition, Noisagool et al. (2016) has suggested a very crucial point about the regional stress and the fault plane instability revealed from the inversion of derived focal mechanisms from the 5 May 2014 earthquake sequences. They found that the Mae Lao Segment (MLS) has a higher shear stress than the other segments of the PFZ. With the stress from the north ($\approx N18E$; Noisagool et al., 2016), the MLS is likely to be the fault that produced the main shock. Its movement has induced the Pan Segment (PS) which has a lower shear stress to slip. Noisagool et al. (2016) showed that there were mixtures of all three kinds of focal mechanisms: strike-slip, normal, and thrust motions. These mixed mechanisms result from the motions of both the MLS and PS and the structural heterogeneities between them.

In contrast to the PFZ, the east-trending Mae Chan Fault Zone (MCFZ, Fig. 1a) in the north of the PFZ has a slightly faster slip rate and is longer (155 km). It was classified as an active fault in the study of Charusiri et al. (1999). Most of the scientists then believed that the

MCFZ would be the fault that produces large events based on its paleo-seismicity (Nutalaya et al., 1985; Charusiri et al., 2000; Fenton et al., 2003). This has led to many geological and geophysical studies on the MCFZ (e.g., Wood, 1995; Hinthong, 1995; Rymer et al., 1997; Kosuwan et al., 1998; Kosuwan and Lumjuan, 1999; Kosuwan et al., 2000; Wood, 2001; Kosuwan et al., 2003; Fenton et al., 2003; Wood et al., 2004; Phodee et al., 2014; Wood et al., 2015) in the past decades and little attention on the PFZ. In the end, only a few M4 earthquakes occurred in the MCFZ since the installation of first seismometer. With the accumulated tectonic stress coming from the north to both faults, this leads to the intriguing question of why the PFZ slipped instead of the MCFZ. Answers probably lie in the characteristics of these two faults, e.g. the fault plane, the frictional coefficient, and the interconnected fluid in the fault.

The occurrence of the largest earthquake in Thailand history on the PFZ is a good reason to conduct geological and geophysical investigations to probe the characteristic of the PFZ. One of the geophysical methods conducted worldwide is the magnetotelluric (MT) method. A magnetotelluric survey yields the resistivity structure which can be used to image faults and to study the fault properties and characteristics and its relation with earthquakes (Bedrosian et al., 2002; Becken and Ritter, 2012; Rao et al., 2004; Patro et al., 2005; Wannamaker et al., 2014; among many others). In many regions around the world, MT results reveal that high conductivity anomalies are often associated with the faults and seismicity of the region. In the San Andrea Fault, seismicity along each fault segment was linked to resistivity anomalies probed by MT surveys (Bedrosian et al., 2002; Bedrosian et al., 2004; Unsworth and Bedrosian, 2004a, 2004b; Becken and Ritter, 2012). For the creeping segment of the fault, the high conductivity zone was observed within the fault indicating the presence of saline fluid. In contrast, in the locked fault segment, there was no high conductivity zone within the fractured fault. In the tectonic studies of the Central Indian Tectonic Zone, many conductors were found at different depths, e.g., from upper crust to mid-crust, and/or from mid- to lower crust, in association with the faults where seismicity also took place (e.g., Rao et al., 2004; Patro et al., 2005; Naganjaneyulu and Santosh, 2010; Abdul Azeez et al., 2013). Their interpretations of the low resistivity bodies were mainly based on either the mafic magmatic underplating and/or the presence of the aqueous fluid either in the fractures or intruding from the deep. In the Cascadia subduction system, USA (Wannamaker et al., 2014), the relatively high resistivity anomalies were interpreted as a lack of fluid and sediment indicating a plate locking zone, while the low resistivity anomalies were associated with the no plate lock zone implying with the presence of shallow sediment, and the fluid at great depth. In an arc-continent collision of Taiwan, Bertrand et al. (2012) found conductive zones at great depth and these have some relationship with the crustal seismicity. They interpreted the low resistivity zones as the interconnected saline fluid. A deep crustal conductor associated with the fluid was also observed in the New Zealand Southern Alps (Wannamaker et al., 2002) and in Japan (Mitsuhata et al., 2001; Ogawa and Honkura, 2004). The low resistivity anomalies were also found to be related to the low velocity zone in the lower crust beneath the Tangshan area indicating the existence of fluids which help to weaken the upper and middle crustal seismogenic layers and so cause large earthquakes (Wang et al., 2013). Similar

scenarios were also found in the 1995 Kobe earthquake, Japan (Zhao et al., 1996), the 2001 Bhuj earthquake, India (Mishra and Zhao, 2003), the 2000 western Tottori earthquake, western Japan (Zhao et al., 2004) and the 2008 Iwate-Miyagi inland earthquake, Japan (Ichihara et al., 2011), among many others. With the correlation of low velocity and low resistivity, one of the explanations for the earthquake occurrence in these regions is the crustal heterogeneities, rather than just the stress condition alone (Zhao et al. 1996; Mishra and Zhao, 2003; Zhao et al., 2004; Wang et al., 2013)

Many of these studies have shown the importance of MT method for studying fault zones and earthquake mechanisms. Here, to study the characteristic of the PFZ, we conducted a 3-D MT survey covering the PFZ with more stations in the region where the Pan Segment intersects the Mae Lao Segment which is the area where most of the epicenters were located. In the absence of any geological and geophysical studies, our resistivity model obtained from the MT survey is therefore the first providing detailed information in the region around the PFZ.

2. Regional geologic framework of the Phayao Fault Zone and Northern Thailand

The tectonic setting and the regional geologic map around the Phayao Fault Zone (PFZ) are shown in Fig. 2a and 2b, respectively. According to the tectono-stratigraphic zone (Metcalf, 2013; Morley et al., 2011; DMR, 2014), the tectonics of the northern Thailand is divided into the Inthanon zone on the west (west of the Mae Tha Fault Zone, MTFZ, in Fig. 2a), the north – south trend Sukhothai fold belt in the center which covers most of our study area (Fig. 2a), and the Indochina terrane on the east (east of the Nan province in Fig. 2a) which is mostly outside our study area. The Inthanon zone which is part of the larger Shibumau terrane (Metcalf, 1997) that collided with the Indochina terrane during the Permian and Triassic comprises mainly of the high grade metamorphic rocks and the igneous intrusion overlain by the Upper Paleozoic rocks. The Sukhothai fold belt, considered as the magmatic arc developed along the margin of the Indochina Terrane (Sone and Metcalfe, 2008; Sone et al., 2012), is underlain by the Paleozoic and Mesozoic sedimentary rocks and the volcanic rocks, intruded by the Triassic S-type granite of the Central Granitoid Belt (Charusiri et al., 1993). The folds and the strike-slip faults found in the Sukhothai fold belt is mostly associated with the collision of the Indian and Eurasian plates during the Cenozoic.

There are three major active fault zones in the northern Sukhothai fold belt: the Mae Chan Fault Zone (MCFZ), the Phayao Fault Zone (PFZ), and the Mae Tha Fault Zone (MTFZ) as shown in Fig. 1b and Fig. 2b. Unlike the orientations of the other fault zones, the left–lateral strike–slip MCFZ cuts almost east to west across the Triassic granite in northern Thailand from the Thai – Lao border in the east to terminate in the Fang basin (Fig. 2b) for a total length of around 185 km (Morley et al., 2011). Its slip rate is between 0.3 and 3 mm/yr (Fenton et al., 2003). It almost embraces one side of the 50 km long Fang basin (Fig. 2b). On the southwest of

the study area, the Mae Tha Fault Zone (MTFZ) is another zone with high seismicity ($< M4$) in recent years. Its orientation is N – S trending in the north but gradually forms an arcuate trace about 140 km long (Morley et al., 2011) and is convex toward the Chiang Mai basin (Fig. 1a). Interestingly, some geologists have documented the MTFZ as a strike – slip fault while some regard it as a thrust with a low dip angle (Wood and Singharajwarapan, 2014).

The Phayao Fault Zone (PFZ) which is the main focus of our study here runs from south to north. It is separated into three major segments (Fig. 1b and Fig. 2b; Uttamo et al., 2003; DMR, 2007; and DMR, 2014) with similar lengths of 50 km. In the south, the Mae Jai Segment (MJS) is oriented in the NNW – SSE trending and was classified as a normal fault by Uttamo et al. (2003). West of the MJS but slightly north is the Pan Segment (PS) which is a right lateral strike – slip fault running in an almost N – S direction. The northern end of the PS almost intersects with the NE – SW trending left lateral strike – slip Mae Lao Segment (MLS) which is the third segment of the PFZ. The transition zone between the PS and MLS is the epicenters of the 5 May 2014 events (Fig. 1b). On the west of the PFZ, the Triassic granite (Tgr) and the Carboniferous sandstone and shale (C) are aligned in the north – south direction parallel to the fault (Fig. 2b). Both are overlain by the Quaternary NNE – SSW Fang basin in the north and the Chiang Mai basin in the southwest (Fig. 2b). The surface geology of the PFZ is a mix of the Quaternary alluvial deposits (Qa), Triassic biotite granite (Tgr), and Silurian/Devonian meta-sediments and volcanic rocks (SD). The eastern side of the PFZ is mostly overlain by Quaternary sediments (Qa) on top of the Mesozoic non marine sedimentary rock (JK). The Mesozoic marine and the extrusive rocks are found to be aligned in the NE – SW and parallel to the Mae Lao segment and the MCFZ in the north east of the study area.

These three major faults (MCFZ, MTFZ and PFZ) have produced many hot springs along their surface traces. The prominent hot springs (Fig. 2) are the Mae Chan hot spring (Amatyakul et al., 2015) located at almost the center of the MCFZ, the Fang hot spring (Amatyakul et al., 2016) located at the west end of the MCFZ near the Fang basin, the mid-temperature Huai Sai Khao hot spring of the PFZ (Fig. 2b), and also many hot springs along the MTFZ.

3. Magnetotelluric Survey and the Three-Dimensional Inversion

In November 2015, 29 MT stations were deployed covering a $140 \text{ km} \times 140 \text{ km}$ area (Fig. 1b and Fig. 2) to ensure that the MT technique can “image” the near surface down to the lower crust. Uniform coverage of the stations is impossible as some of the land was not accessible due to lack of navigable terrain and/or permission from the owner. Most of the MT sites were above sedimentary rocks (Fig. 2b) in rice and corn farms. Only a few sites were placed over the granitic rocks. The main interest of this study is the junction of the PFZ between the PS and the MLS where the epicenters of the 5 May 2014 and its aftershocks were located. Many MT stations were installed in the vicinity of these segments. Many sites were also located outside to constrain the

resistivity within the area of interest. In addition to these 29 newly deployed stations, two stations from previous geothermal experiments, one from Fang hot spring area (Amatyakul et al., 2016) and another from Mae Chan hot spring area (Amatyakul et al., 2015), were also incorporated bringing the total to 31 stations.

One set of KMS Technologies MT system was deployed in the morning and left overnight to record the electric and magnetic fields. The equipment was recovered and moved to the next site the next day. To improve the data quality, the MT data was acquired simultaneously from another MT system 600 km south of the study area in Kanchanaburi province where it was treated as a remote reference site. The acquired data around the PFZ was processed with the data at the remote reference site based on the robust multiple-station technique of Egbert (1997). After the data processing, the impedance tensor \mathbf{Z} and the vertical magnetic transfer function \mathbf{T} were logarithmically chosen to cover 16 periods starting from 1,000 Hz to about 600 s, for each site. Some selected apparent resistivities and phases of the xy - and yx -modes with the error bars are shown in Fig. 3 and the vertical magnetic transfer functions or tippers in Fig. 4.

The off-diagonal \mathbf{Z} (Z_{xy} and Z_{yx}) and the tipper \mathbf{T} from these 31 sites were inverted with the WSINV3DMT parallel version (Siripunvaraporn et al., 2005; Siripunvaraporn and Egbert, 2009). The minimum error floors for both data sets were set at 5%. Several inversions were started from the homogeneous earth with 1 to 1000 Ω m. All of these initial models were discretized using a $52 \times 52 \times 44$ grid (with 7-air layers on top of the topography) in the north-south, west-east and vertical directions, respectively. The horizontal grid spacing of 4 km in the study area were discretized on average in both directions. Outside of the study area, the horizontal grid spacing was increased in a logarithmic scale to avoid the boundary effects from the forward modeling routine (Siripunvaraporn et al., 2002). The first layer in the vertical direction was finely discretized to provide high accuracy solutions for all periods. The thickness of a given layer was 1.2 – 2.0 times that of the previous layer.

Most of the inversions starting from different initial models can reduce the RMS misfit from around 15 RMS to within an acceptable level of around 2. Most of the final inverted models show similar resistive and conductive anomalies at the same locations but in some cases of different sizes and depths. However, inverted models starting from low and high resistivity values often produce rough models which over-fit the observed data and are therefore discarded. In addition to the RMS misfit, another constrain to select the final inverted model is basically that it should produce some agreements with the surface geology. Based on these two conditions, the final inverted model was selected from the 300 Ω m initial model after 6 iterations with an RMS of 1.97 and is shown in Figs. 5 – 7. The correspondence with the surface geology is described in the next section. The 30 hypocenters obtained from Noisagool et al. (2016) for earthquakes with $M_w > 3.5$ are also plotted in Figs. 5 and 6.

There are many interesting anomalies listed and described in the next section. As in Amatyakul et al. (2016), we performed sensitivity analysis to verify their existence. By replacing

the resistivity of the anomaly with the background resistivity (around 100 – 300 Ω - m), implying that this anomaly does not exist, we then run the forward modeling routine and re-compute the misfit of each station. The relative change of the RMS values of each station is computed via, $\text{Relative Change} = 100\% \times (\text{RMS}_{\text{new}} - \text{RMS}_{\text{original}})/\text{RMS}_{\text{original}}$, where RMS_{new} is the fit after replacing the anomaly with the background resistivity, and $\text{RMS}_{\text{original}}$ is from the inverted model in Fig. 5 – 7. Relative changes from two interesting anomalies (ML and Qa), as examples, are shown in Fig. 8. By replacing the anomalies with the background, MT stations located near the anomalies show significant changes. This means that these anomalies are required by the observed data and are not the artifacts from over-fitting the data.

4. Interpretation and Discussion

As stated earlier, there are two main reasons why we prefer the inverted model in Fig. 5 and 6 as our final model. First, it can produce the responses that fit the observed data with an RMS of 1.97 (Fig. 3 and Fig. 4). Second, the surface geology (Fig. 7a) corresponds closely with the final inverted model at 50 m depth (Fig. 7b). West of the PFZ, the Triassic granite rock (Tgr) corresponds well with high resistivity bodies ($> 100 \Omega$ m). Most of the Quaternary alluvial deposit (Qa; Fig. 7a) within the study area is imaged as the high conductivity bodies ($< 30 \Omega$ m; Fig. 7b). On the east, the Mesozoic non marine (JK) is scattered around the Qa (Fig. 7a). The JK is mapped as the high resistivity body. Within the PFZ at this depth, the Silurian/Devonian meta-sediments (SD) and volcanic rocks are seen as a moderate resistivity ($\approx 100 \Omega$ m).

Correspondence of the shallow conductors to the hot springs at surface, and to the basins

Locations of many hot springs in our study area have already been shown in Fig. 2. However, since many readers may not be familiar with the local geography, in this section, we also plot the locations and the labels on Fig. 6a and 7b. On the west and north of the PFZ, even though there is a large resistive region (T; Fig. 5, 6 and 7b) which dominates from the surface to a depth of around 20 km, there are still many conductive anomalies within the resistive T zone. In the north of the study area, near the Fang hot spring (Fig. 6a), the conductive F anomaly (Fig. 6a – 6b) can be mapped to about 2 - 3 km depth. This F conductive zone with similar thickness was also seen in the earlier MT geothermal survey using more closely spaced MT stations (Amatyakul et al., 2016) and was interpreted as the sedimentary rock of the Fang basin. The F anomaly here is therefore likely to represent the Fang basin, also confirming a study of Sethakun and Pimasarn (1990) which estimated the Fang basin to be about 3 km thick (Morley et al., 2011).

About 40 km to the east of the F anomaly and to the north of the study area, there is another large conductive zone (MCH) occurring slightly south of the Mae Chan Fault Zone (MCFZ) located in between the famous Mae Chan hot spring and Mulika hot spring in the west

(Fig. 2b, Fig. 6a and 7b). This MCH conductor extends to a depth of 3 km before being replaced by the resistive body. This MCH conductor did not appear in our previous MT survey (Amatyakul et al., 2015) as the earlier study was focused just around a few square kilometers of the Mae Chan hot spring. It is therefore very interesting to have this high conductivity body in the region dominated by the Triassic granite at the surface which was interpreted as the heat source of the Mae Chan hot spring (Amatyakul et al., 2015). To determine whether this MCH conductor plays any roles with the MCFZ or acts as the hot reservoir serving the two hot springs, more geophysical and geological studies should be conducted to probe this conductive feature.

In the vicinity of the PFZ, there are two large and shallow conductors (PF1 and PF2; Fig. 6a – 6b and Fig. 5c) located next to the Phu Faung hot spring (Fig. 2b; Fig. 6a). PF1 (Fig. 6a) is very shallow and south of the hot spring, whereas PF2 (Fig. 6b) is deeper and north of the hot spring. At this point, we do not know whether PF1 and PF2 are connected. Further closely spaced MT sites around the region are necessary to probe the connection. As PF1 and PF2 are closer to the hot spring and have similar thickness and depth to the fluid reservoir of the Fang hot spring (see Amatyakul et al., 2016), it is possible that both are involved with the Phu Faung hot spring, or just the Silurian/Devonian meta-sediments with high water content as found in the surface. In contrast to the MCH, F, PF1 and PF2 conductors found beneath the other hot springs, there is no conductor found beneath the Huai Sai Khao hot spring (Fig. 2b; Fig. 6a). In between the Mae Lao Segment (MLS) and the Pan segment (PS), there is an S conductor located around 500 m to 3 km depth (Fig. 6b). Unlike other conductors (F, PF1 & PF2 and MCH), the location of this S conductor cannot be linked to any of the hot springs. This might be one piece of evidence to indicate that this kind of conductor is not necessarily associated with the hot springs, and vice versa for the case of the Huai Sai Khao hot spring.

On the east of the PFZ, the Quaternary alluvial deposit (Qa; Fig. 7) mapped at the surface as the conductive body, appears to be less than 1 km thick (Fig. 7a, and Fig. 7b) which is thinner than the basin on the west and north of the PFZ. The alluvial deposit is overlain on a resistive body (J; Fig. 6a – 6b) where at the surface the J is in agreement with the Mesozoic non marine (JK; Fig. 2b and Fig. 7a). The J resistor remains to about 3 km depth, which might be a typical thickness of the Mesozoic non marine sedimentary rock, before being replaced with the moderate resistivity layer. Near the eastern edge of the study, there is another resistive body at a depth greater than 4 km (Fig. 6c). We are not certain whether this resistive body is the continuation of the J resistor going deeper to the east or a different anomaly since we have limited data.

Mid to lower crust conductive and resistive anomalies of and around the PFZ

There are many interesting conductive and resistive features located both in between the Mae Lao segment (MLS) and the Pan segment (PS) of the PFZ (Fig. 2b and Fig. 6a), and along the sides of the PFZ. In the upper to middle crust, Fig. 5, and 6 clearly show that the PFZ cuts into

the resistive zones: the resistive (T; Fig. 5b – 5f and Fig. 6a – 6e) zone on the west of the MLS, and another narrow resistive band (R1; Fig. 5d – 5f; and Fig. 6b – 6d) located in between the PS and the Mae Jai Segment (MJS). Based on the geology map (Fig. 2b; Fig. 7a), the Triassic granite is observed on the west of the MLS and corresponds well with the T resistive zone. Both features can then be conveniently linked together, similar to what we found in the Fang geothermal study (Amatyakul et al., 2016) and in the Mae Chan geothermal study (Amatyakul et al., 2015) where the high resistive zone was linked to the Triassic granite.

In contrast to the west, granite is rarely found on the surface on the east of the PS (Fig. 2b and 7a), as the area is mostly overlain by the alluvial deposits and the meta-sediments (Fig. 2b) at the surface. It is interesting to observe that the narrow resistive R1 zone that appears in between the PS and the MJS has about the same depth as the T resistive zone (Fig. 5d – 5f). We therefore identify the R1 as the batholith granite, similar to the T resistive zone. If R1 and T are the same granite belt, it indicates that the PFZ has separated the intrusive granite rocks into two zones, where R1 is in the eastern edge of the rock and T is on the west. If not the same type, it indicates that R1 had slipped from the north to attach here. Another interesting resistive anomaly is R2 (Fig. 6d – 6f; Fig. 5b – 5c, 5g and 5h). R2 does not appear until below 10 km. Its appearance coincidentally marks the termination of the PS segment. Its role is also very important for the seismicity of the 5 May 2014 event and aftershock as most of the seismicity occurred above it (Fig. 6d). Similarly, R2 and the T and R1 resistive zones can be interpreted as the S-type biotite granites that originated during the collision of the Sibumasu and Indochina terranes during the mid-Triassic.

In between the MLS and PS faults, there is an ML conductor (Fig. 5d and 5g, and Fig. 6c – 6e) near the center of the study area, and the P2 conductor (Fig. 5f and 5h, and Fig. 6c – 6f) in the south of study area. The Mae Lao segment just runs through this ML conductive anomaly which is why we named it ML. The location of ML is almost identical to the very shallow PF1 (Fig. 6a) and near the Phu Faung hot spring (Fig. 6a). As the ML conductor has a depth from about 4 km to the lower crust (Fig. 5f), its relationship with the hot spring is uncertain. At about the same depth, most of the epicenters occurred just north of the ML conductor. This indicates that the ML conductor might play an important role in the earthquake sequence of the 5 May 2014 event occurring on both MLS and PS.

Seismicity and the resistivity anomalies

Based on the recent calculation from the regional waveforms (Noisagool et al., 2016), most of the seismicity on 5 May 2014 ($M_w > 3.5$) occurred in the seismogenic zone, above a depth of 15 km. As large earthquakes often occur at the highest strength of the brittle crust (Tse and Rice, 1986; Scholz, 1988), the hypocenter depth of the main shock estimated by Noisagool et al. (2016) is therefore reasonable and in agreement with the estimated brittle – ductile transition of

Morley et al. (2011) at the depth around 12 km. The inverted model at the depth of 12 km (Fig. 6d) reveals that the seismicity lies mostly around the edge of the ML conductor at the transition zone of the PS and the MLS. Fig. 5g, which displays the cross sectional plot along the MLS segment from north to south, shows that the seismicity is localized around the region of moderate resistivity (around 100 Ω m), above the R2 resistor, but not inside the ML conductor. Similarly, a cross sectional plot from north to south along the PS segment (Fig. 5h) also shows similar patterns; the seismicity just lies above the lower resistive anomaly which might be an extension of the ML conductor to the west, and along the edge of the R1 resistor. The seismicity along the edges of the resistors and conductors were also observed in numerous publications (e.g., Mitsuhashi et al., 2001; Ogawa et al., 2001; Ogawa and Honkura, 2004; Ichihara et al., 2011; Bertrand et al., 2012; Unsworth and Bedrosian, 2014a; Rawat et al., 2014; Wannamaker et al., 2014).

As described earlier, there are at least three major possible interpretations to explain the high conductivity around the fault zones in the mid-crust: saline fluid, graphite, and partial melt. It is not easy to pin-point the cause of the low resistivity ML around the PFZ as we have very limited geological and geophysical information on the area. Although northern Thailand is currently experienced an east – west extension (Morley, 2001; Simon et al., 2007; Morley, 2007; Charusiri and Pum-Im, 2009), the temperature of the hot springs around the PFZ is not high enough. The Huai Sai Khao hot spring has a temperature of just around 56°C at the surface. A partial melt at the upper and mid-crust for the ML conductor is therefore very unlikely. Although graphite was reported to be found in the Fang district, there is no graphite mining in the region. It is therefore unlikely that graphite or other high conductivity ores are a major source for the high conductivity ML.

Here, the aqueous fluid explanation seems to be the most suitable hypothesis for the cause of the earthquakes in this region. This is similar to other publications which often give the high conductivity found to the saline fluid as a possible cause for the seismicity in the region (e.g., Mitsuhashi et al., 2001; Bedrosian et al., 2004; Ogawa and Honkura, 2004; Ichihara et al., 2009; Becken and Ritter, 2012; Unsworth and Bedrosian, 2014a; 2014b;). The role of high pressure fluid in causing the seismicity has been widely studied (e.g., Tullis et al., 1996; Cox, 2002; Fujimoto et al., 2002). The saline fluid that is trapped and stored within the ML conductor aids in reducing the strength of the faults, particularly the MLS as this segment is richer in fluid than other segments, by lowering the effective normal stress. The high pore fluid pressure in the MLS segment (found from this study) and the higher shear stress from its own geometry (Noisagool et al., 2016) make the fault mechanically weak. The continuous pre-existing tectonic stress coming from the north (Tingay et al., 2010) to northern Thailand (Noisagool et al., 2016) has become larger than the maximum strength that the fault can withstand. The result was that the MLS slipped producing the main shock of 5 May 2014 followed by many aftershocks ($M_w > 3.5$) occurring between the MLS and PS just within a localized zone of moderate resistivity (around 100 Ω m between the ML conductor and the R2 resistor; Fig. 5c, 5g and 5h; and Fig.

6d), not directly within the ML conductor nor inside the resistor R2 for both the PS and MLS. This is summarized in the diagram shown in Fig. 9.

Directly above the ML conductor is the PF1 and slightly north is the PF2. In between the PF1 and PF2 conductors and the ML conductor is a thick moderate resistivity layer (about 4 km thick) as shown in Fig. 5g. It is therefore unclear whether PF1 and PF2 have any direct connection to the ML as the magnetotelluric resolutions might not be detailed enough to validate this. However, as the fault cuts through the middle of both conductors, a connection might exist within the MLS segment. If there is a connection, it might indicate that the hot fluid of the Phu Faung hot spring (Fig. 2b; Fig. 7b) comes from the deep ML conductor by rising through the fractured granite pathways of the MLS and getting stored in the shallow PF1 and PF2 conductors. We suspect that this is how the high pressure fluid of the ML conductor releases the pressure to the environment without causing large earthquakes. Occasionally, when the high pressure becomes large enough, it causes the fault to suddenly slip causing the earthquakes as a way to release the high pressure. Several of the aftershock focal mechanisms indicate all kinds of motions: strike-slip, normal, and thrust motions. The mixed focal mechanisms might be induced by the presence of the fluid in the fault zone. Although we prefer the fluid explanation for the ML conductor, to fully confirm the existence of the fluid, other geophysical techniques are necessary. These include observing the S-wave reflector as in Mitsuhashi et al. (2001), Umino et al., (2002) and Aoki et al., (2016), or the Poisson's ratio and the low-Vp and low-Vs features (Zhao et al., 1996; Mishar and Zhao, 2003; Zhao et al., 2004; Lei and Zhao, 2009; Mahesh et al., 2012; Wang et al., 2013) or the low density zone (Ichihara et al., 2009).

In the south, there is a large P2 conductor extending from about a depth of 5 km to the 32 km depth Moho and to the mantle (Fig. 5f; Fig. 6c – 6f). The P2 conductor covers a large area but is mostly within the PFZ. There is also a P1 conductor at a shallow depth above the P2. Nearby P1 is a Sob Pong hot spring. It might therefore be interpreted in a similar way to the other conductors as the resistivity is lowered by the aqueous fluid. The hot fluid of P2 can rise through the many fault segments and get stored in P1, as with the Phu Faung geothermal system in the north. Nevertheless, the difference is there is no seismicity in the region near the P1 and P2 conductors as in the ML conductor. There are many possible reasons to explain the lack of the seismicity in this area. The P1 and P2 conductors are not really fluid related but just conductive rocks. Another possibility is that the geometry of the fault segments in the south is mostly north–south trending. As indicated in the Mohr's diagram of Noisagool et al. (2016), this geometry requires much greater stress from the north to slip than that of the MLS lying in the NE – SW direction. It is therefore more difficult to slip even with the fluid localized in the faults as in the MLS segment. The bottom of the P2 conductor is not well defined as it extends deep into the mantle. As there are not many MT sites in the region near the P2 conductor, we might need more MT measurements in this area to verify the existence of the P1 and P2 conductors and determine their size and depth. As with the ML conductor, other geophysical techniques, particularly the seismic tomography, are necessary.

To the north of the study area, our resistivity structure (Fig. 5 and 6) shows that there is no clear large conductor within the seismogenic zone beneath the Mae Chan Fault Zone (MCFZ). The lack of the large conductor beneath the MCFZ could be one explanation for the lack of the moderate to large seismicity generated by the MCFZ. Without the fluid (as is presented beneath the MLS fault) the MCFZ would require a larger amount of stress in order to slip. Paleo-seismicity (Charusiri et al., 2000; Fenton et al., 2003) has indicated that several large earthquakes have occurred on the MCFZ. Nevertheless, our MT station coverage for this work is mostly in the PFZ region. To further confirm the non-existence of the highly conductive zone within the MCFZ in the upper to mid-crust, more MT stations across the MCFZ would be necessary. Geodetic measurement for the slip rate in the area might also be necessary to assess the present-day motions of the faults in the northern Thailand.

Fig. 5 and 6 shows the existence of the deeper conductors, C1 and C2 on the eastern side of the PFZ in the lower crust below the estimated brittle – ductile transition (Morley et al., 2011). Although the presence of C1 and C2 are beyond the scope of the current study, they both might be related to the crustal extension in northern Thailand (Morley, 2001; Morley, 2007; Simon et al., 2007; Charusiri and Pum-Im, 2009;) and both conductors might be dehydrated metamorphic rocks in the lower crust (Hyndman and Sheare, 1989) or fluids released from the magma (Abdul Azeez et al., 2013). They could also be remnant dehydration fluid accumulated during the Permo-Triassic subduction like what lies beneath Kanchanaburi province, western Thailand (Boonchaisuk et al., 2013). However, both hypotheses require further investigation via other geological and geophysical techniques.

5. Conclusion

A year and a half after the largest earthquake (Mw 6.5) in recent Thailand history on 5 May 2014, a 3-D magnetotelluric survey was started in order to investigate the Phayao Fault Zone (PFZ) rupture area. A total of 31 stations were deployed within a 140 km × 140 km area covering the PFZ. The remote reference site was installed 600 km south of the data acquisition area and operated simultaneously with these 31 sites. The acquired data were then processed using the robust multiple-station technique (Egbert, 1997) to obtain a broad frequency range impedance tensors and the vertical magnetic transfer functions or tippers. The impedance tensors and the tippers from all stations were then re-sampled to 16 periods to be included in the 3-D inversion code (WSINV3DMT of Siripunvaraporn et al., 2005; Siripunvaraporn and Egbert, 2009).

The final 3-D inverted model displayed many resistive and conductive anomalies. The surface anomalies match well with the local surface geology. The Triassic granite rock matches well with the resistive zone in the west, while conductive features agree with the Quaternary basins distributed around the study area. In the top few kilometers, there are many conductive

features that correspond well with the hot springs at the surface, such as beneath the Mae Chan hot spring, the Fang hot spring, and the Phu Faung hot spring. However, one hot spring has no shallow conductive zone. Another shallow conductive zone was imaged in the area of no hot spring.

The most interesting feature was the conductive anomalies found beneath the Mae Lao Segment (MLS) and partially beneath the Pan Segment (PS) from a depth of 4 km to mid-crust where both MLS and PS are part of the PFZ. The conductive anomaly was just in the south of the seismogenic zone where we interpreted it as the saline fluid rich zone. As many studies indicate that the fluid helps weaken the fault zone, we also have the same hypothesis that the saline fluid found beneath the MLS played an important role in the 5 May 2014 earthquake. **The processes that drive the main shock are summarized in Fig. 9.** The presence of fluid in the MLS and the high fault plane instability govern the slip of the PFZ. The continuing pre-existing tectonic stress from the north applying to northern Thailand exceeded the maximum frictional strength of the MLS causing it to slip and so produce the main event of 5 May 2014. The energy was then transferred to the PS resulting in slipping in both the MLS and PS causing the aftershocks. Since there is no deep conductor found beneath the Mae Chan Fault Zone (MCFZ), it might indicate that a larger tectonic stress is needed to cause the MCFZ to slide. However, to confirm the presence of the fluid beneath the MLS and no fluid beneath the MCFZ, other geophysical techniques are required and also more MT sites might be necessary.

As this is the first geophysical attempt in the region, we hope that more geophysical studies such as seismic reflection, seismic tomography, geodetic measurement and gravity will follow to help constrain our results.

6. Acknowledgement

This research has been supported by the Development and Promotion of Science and Technology Research Grant 037/2557, the Thailand Center of Excellence in Physics (ThEP), and the Thailand Research Fund (RSA5780010). We would like to thank Dr. Michael Allen for editing the English of this manuscript, and the two reviewers who provide many good comments to improve the manuscript.

7. References

- Abdul Azeez, K.K., Unsworth, M.J., Patro, P.K., Harinarayana, T., Sastry, R.S., 2013. Resistivity Structure of the Central Indian Tectonic Zone (CITZ) from Multiple Magnetotelluric (MT) Profiles and Tectonic Implications. *Pure Appl. Geophys.* 170, 2231-2256. <http://dx.doi.org/10.1007/s00024-013-0649-y>
- Aoki, S., Iio, Y., Katao, H., Miura, T., Yoneda, I., Masayo, S., 2016. Three-dimensional distribution of S wave reflectors in the northern Kinki district, southwestern Japan, *Earth Planets Space*, 68: 107.
- Amatyakul, P., Rung-Arunwan, T., Siripunvaraporn, W., 2015. A pilot magnetotelluric survey for geothermal exploration in Mae Chan region, northern Thailand. *Geothermics* 55, 31-38. <http://dx.doi.org/10.1016/j.geothermics.2015.01.009>
- Amatyakul, P., Boonchaisuk, S., Rung-Arunwan, T., Vachiratienchai, C., Wood, S.H., Pararai, K., Fuangswasdi, A., Siripunvaraporn, W., 2016. Exploring the shallow geothermal fluid reservoir of Fang geothermal system, Thailand via a 3-D magnetotelluric survey. *Geothermics* 64, 516-526. <http://dx.doi.org/10.1016/j.geothermics.2016.08.003>
- Becken, M., Ritter, O., 2012. Magnetotelluric studies at the San Andreas fault Zone: Implications for the role of fluids. *Surveys in Geophysics* 33, 65 – 105.
- Bedrosian, P.A., Unsworth, M.J., Egbert, G., 2002. Magnetotelluric imaging of the creeping segment of the San Andreas Fault near Hollister. *Geophys. Res. Lett.* 29, 1-4. <http://dx.doi.org/10.1029/2001GL014119>
- Bedrosian, P.A., Unsworth, M.J., Egbert, G., Thurber, C.H., 2004. Geophysical images of the creeping segment of the San Andreas fault: implications for the role of crustal fluids in the earthquake process, *Tectonophysics* 385, 137-158. <http://dx.doi.org/10.1016/j.tecto.2004.02.010>
- Bertrand, E.A., Unsworth, M.J., Chiang, C.-W., Chen, C.-S., Chen, C.-C. , Wu, F.T., Türkoğlu, E., Hsu, H.-L., Hill, G. J., 2012. Magnetotelluric imaging beneath the Taiwan orogen: An arc-continent collision. *J. Geophys. Res.* 117, B01402. <http://dx.doi.org/10.1029/2011JB008688>.
- Boonchaisuk, S. Siripunvaraporn, W., Ogawa, Y., 2013. Evidence for middle Triassic to Miocene dual subduction zones beneath the Shan-Thai terrane, western Thailand from magnetotelluric data. *Gondwana Research* 23, 1607-1616. <http://dx.doi.org/10.1016/j.gr.2012.08.009>
- Charusiri, P., Clark, A.H., Farrad., E., Archibald., D., Charusiri, B., 1993. Granite belts in Thailand: evidence from the $^{40}\text{Ar}/^{39}\text{Ar}$ geochronological and geological syntheses. *Jour. of*

532 Southeast Asian Earth Sciences 8, 127-136. [http://dx.doi.org/10.1016/0743-9547\(93\)90014-](http://dx.doi.org/10.1016/0743-9547(93)90014-G)
533 G

534 Charusiri, P., Kosuwan, S., Lumjuan, A., Wechbunthung, B., 1999. Review of active faults and
535 seismicity in Thailand. GEOSEA'98 Proceedings, Geol. Soc. Malaysia Bull. 43, 653 -655.

536 Charusiri, P., Kosuwan, S., Daorerk, W., Wechbunthung, B., Kuthranon, S., 2000. Earthquake in
537 Thailand and Southeast Asia Mainland, Complete Report (in Thai), Thailand Research Fund.
538 212 pp.

539 Charusiri, P., Pum-Im, S., 2009. Cenozoic Tectonic Evolution of Major Sedimentary Basins in
540 Central, Northern, and the Gulf of Thailand. BEST 2, 40-62.

541 Cox, F., 2002. Fluid flow in mid-to deep crustal shear systems: Experimental constraints,
542 observations on exhumed high fluid flux shear systems, and implications for seismogenic
543 processes. Earth, Planets and Space 54, 1131-1125. <http://dx.doi.org/10.1186/BF03353312>

544 Department of Mineral Resource, 2007. Geology and Resource Chiang Rai Province
545 Classification and Management. Department of Mineral Resource, Thailand (in Thai).

546 Department of Mineral Resource, 2014. Report on a Study of 5th May 2014, 6.3 Earthquake.
547 Department of Mineral Resource, Thailand (in Thai).

548 Egbert, G.D., 1997. Robust multiple-station magnetotelluric data processing. Geophys. J. Int.
549 130, 475-496. <http://dx.doi.org/10.1111/j.1365-246X.1997.tb05663.x>

550 Fenton, C.H., Charusiri, P., Wood, S.H., 2003. Recent paleoseismic investigations in Northern
551 and Western Thailand. Annals of Geophysics 46, 957-981. [http://dx.doi.org/10.4401/ag-](http://dx.doi.org/10.4401/ag-3464)
552 [3464](http://dx.doi.org/10.4401/ag-3464)

553 Fujimoto, K., Ohtani, T., Shigematsu, N., Miyashita, Y., Tomita, T., Tanaka, H., Omura, K.,
554 Kobayashi, Y., 2002. Water-rock interaction observed in the brittle-plastic transition zone,
555 Earth Planets Space, 54, 1127 – 1132

556 Kosuwan, S., Charusiri, P., Takashima, I., Lumjuan, A., 1998. Active tectonics of the Mae Chan
557 Fault, northern Thailand. In: Proceedings of the Ninth Regional Conference on Geology,
558 Mineral and Energy Resources of Southeast Asia, Geological Society of Malaysia, Kuala
559 Lumpur, 16-20 August 1998 (extended abstract).

560 Kosuwan, S. and A. Lumjuan, 1999. Neotectonics of the Mae Chan Fault in Mae Chan District,
561 Chiang Rai Province. Technical Report, Geological Survey Division, Department of Mineral
562 Resources, Bangkok, Thailand.

563 Kosuwan, S., Saithong, P., Lumjuan, A., Takashima, I., Charusiri, P., 2000. Preliminary Results
564 of Paleoseismic Studies on the Mae Ai segment of the Mae Chan Fault Zone, Chiang Mai,

565 Northern Thailand. Proceedings of the International Symposium on Coordinating
566 Committee for Coastal and Offshore Geoscience Programmes in East and Southeast Asian
567 CCOP), Bangkok, P. 17-27.

568 Kosuwan , S., Saithong, P., Lumjuan. A., 2003. Paleoearthquake on the Mae Ai Segment of the
569 Mae Chan Fault Zone, Chiang Mai, Northern Thailand: Report of Geological Survey
570 Division, Department of Mineral Resources, 57 p. (in Thai with English abstract).

571 Hinthong C, 1995. The study of active faults in Thailand. Proceedings of the technical
572 conference on the progression and vision of mineral resources development, Bangkok:
573 Department of Mineral Resources, 129-140.

574 Hyndman, R.D., and Shearer, P.M., 1989. Water in the lower continentalcrust: Modeling
575 magneto-telluric and seismic reflection results Geophys. J. Int. 98, 343 – 365.
576 <http://dx.doi.org/10.1111/j.1365-246X.1989.tb03357.x>

577 Ichihara, H., Mogi, T., Hase, H., Watanabe, T., Yamaya, Y., 2009. Resistivity and density
578 modeling in the 1938 Kutcharo earthquake source area along a large caldera boundary. Earth
579 Planets Space 61, 345-356. <http://dx.doi.org/10.1186/BF03352916>

580 Ichihara H., Uyeshima M., Sakanaka S., Ogawa T., Mishina M., Ogawa Y., Nishitani T.,
581 Yamaya Y., Watanabe A., Morita Y., Yoshimura R., Usui Y., 2011. A fault-zone conductor
582 beneath a compressional inversion zone, northeastern Honshu, Japan. Geophys. Res. Lett.
583 38, L09301, <http://dx.doi.org/10.1029/2011gl047382>

584 International Seismological Centre, 2012, On-line Bulletin. Internatl. Seis. Cent., Thatcham,
585 United Kingdom. <<http://www.isc.ac.uk>>.

586 Lei, J., Zhao, D., 2009. Structural heterogeneity of the Longmenshan fault zone and the
587 mechanism of the 2008 Wenchuan earthquake (Ms 8.0). Geochem. Geophys. Geosyst. 10,
588 Q10010, <http://dx.doi.org/10.1029/2009GC002590>.

589 Mahesh, P., Gupta, S., Rai, S.S., Rajagopala Sarma, P., 2012. Fluid driven earthquakes in the
590 Chamoli Region, Garhwal Himalaya: evidence from local earthquake tomography. Geophys.
591 Jour. Inter. 191. 1295 – 1304

592 Metcalfe, I., 1997. The Palaeo-Tethys and Palaeozoic-Mesozoic tectonic evolution of Southeast
593 Asia. Proceedings of GOTHAI '97, pp. 260-272. (Department of Mineral Resources,
594 Thailand).

595 Metcalfe, I., 2013. Gondwana dispersion and Asian accretion: Tectonic and palaeogeographic
596 evolution of eastern Tethys. Journal of Asian Earth Sciences, 66, 1-33.
597 <http://dx.doi.org/10.1016/j.jseaes.2012.12.020>

598 Mishar, O.P., Zhao, D., 2003. Crack density, saturation rate and porosity at the 2001 Bhuj, India,
599 earthquake hypocenter: a fluid-driven earthquake?. *Earth Planet. Sci. Lett.* 212, 393-405.
600 [http://dx.doi.org/10.1016/S0012-821X\(03\)00285-1](http://dx.doi.org/10.1016/S0012-821X(03)00285-1)

601 Mitsuhashi, Y., Ogawa, Y., Mishina, M., Kono, T., Yokokura, T., Uchida, T., 2001.
602 Electromagnetic heterogeneity of the seismogenic region of 1962 M6.5 northern Miyagi
603 earthquake, northeastern Japan. *Geophys. Res. Lett.* 28, 4371-4374.
604 <http://dx.doi.org/10.1029/2001GL013079>

605 Morley, C. K. 2001. Combined escape tectonics and subduction rollback back-arc extension: a
606 model for the evolution of Cenozoic rift basins in Thailand, Malaysia and Laos. *Journal of*
607 *the Geological Society, London*, 158, 461–474.

608 Morley, C.K., 2007. Variations in Late Cenozoic–Recent strike-slip and oblique-extensional
609 geometries, within Indochina: The influence of pre-existing fabrics. *J. Struct. Geol.* 29, 36-
610 58. <http://dx.doi.org/10.1016/j.jsg.2006.07.003>.

611 Morley, C.K., Charusiri, P., Watkinson, I.M., 2011. Structural geology of Thailand during the
612 Cenozoic. In: Ridd, M.F. Barber, A.J., Crow, M.J. (Eds.), *The Geology of Thailand*.
613 Geological Society of London, pp. 273-334. <http://dx.doi.org/DOI:10.1144/GOTH.11>

614 Noisagool, S., Boonchaisuk, S., Pronsopin, P. Siripunvaraporn, W., 2016. The regional moment
615 tensor of the 5 May 2014 Chiang Rai earthquake (Mw = 6.5), Northern Thailand, with its
616 aftershocks and its implication to the stress and the instability of the Phayao Fault Zone.
617 *Journal of Asian Earth Sciences* 127, 231-246. [http://dx.doi.org/](http://dx.doi.org/10.1016/j.jseaes.2016.06.008)
618 [10.1016/j.jseaes.2016.06.008](http://dx.doi.org/10.1016/j.jseaes.2016.06.008)

619 Naganjaneyulu, K., Santosh, M., 2010. The Central India Tectonic Zone: A geophysical
620 perspective on continental amalgamation along a Mesoproterozoic suture. *Gondwana*
621 *Research* 18, 547-564. <http://dx.doi.org/10.1016/j.gr.2010.02.017>

622 Nutalaya, P., Sodsri, S., Arnold, E.P., 1985. Thailand, Series on seismology, Southeast Asia
623 Association of Seismology and Earthquake Engineering, vol. II, pp. 403.

624 Ogawa, Y., Mishina, M., Goto, T., Satoh, H., Oshiman, N., Kasaya, T., Takahashi, Y., Nisitani,
625 T., Sakanaka, S., Uyeshima, M., Takahashi, Y., Honkura, Y., Matsushima, M., 2001.
626 Magnetotelluric imaging of fluids in intraplate earthquakes zones, NE Japan back arc.
627 *Geophys. Res. Lett.* 28, 3741-3744. <http://dx.doi.org/10.1029/2001GL013269>

628 Ogawa, Y., Honkura, Y., 2004. Mid-crustal electrical conductors and their correlations to
629 seismicity and deformation at Itoigawa-Shizuoka Tectonic Line, Central Japan, *Earth*
630 *Planets Space*, 56, 1285 – 1291.

631 Patro, P.K., Harinarayana, T., Sastry, R.S., Rao, M., Manoj, C., Naganjaneyulu, K., Sarma,
632 S.V.S., 2005. Electrical imaging of Narmada-Son Lineament Zone, Central India from
633 magnetotellurics. *Phys. Earth Planet. Inter.* 148, 215-232.
634 <http://dx.doi.org/10.1016/j.pepi.2004.09.001>

635 Phoddee, P., Trisirisatayawong, I., Aobpaet, A., 2014. Coseismic and postseismic displacement of
636 2011 Mw 6.8 Tarlay Earthquake, Myanmar using InSAR techniques and inversion analysis.
637 *Engineering Journal*. 19, 157-169. <http://dx.doi.org/10.4186/ej.2015.19.2.157>

638 Rao, C.K., Ogawa, Y., Gokarn, S.G., Gupta, G., 2004. Electromagnetic imaging of magma
639 across the Narmada Son lineament, central India. *Earth Planet Space* 56, 229-238.
640 <http://dx.doi.org/10.1186/BF03353405>

641 Rawat, G., Arora, B. T., Gupta, P. K., 2014. Electrical resistivity cross-section across the
642 Garhwal Himalaya: Proxy to fluid-seismicity linkage. *Tectonophysics*. 637, 68-79.
643 <http://dx.doi.org/10.1016/j.tecto.2014.09.015>

644 Rymer, M.J., Weldon II, R. J., Prentice, C.S., Kosuwan, S., Lumjuan, A., Muangnoicharoen, N,
645 1997. Tectonic setting and Late Quaternary activity along the Mae Chan Fault, Northern
646 Thailand and Western Laos, *Geol. Soc. Am., Abstracts with Programs*, **29**, 229-230.

647 Scholz, C.H., 1988. The critical slip distance for seismic faulting. *Nature* 336, 761-763.
648 <http://dx.doi.org/10.1038/336761a0>

649 Sethakul, N., Pimasarn, V., 1990. Source rock screening and oil/source correlation in the IF 30-
650 01G and 30-02S wells, Fang Field, Thailand. In: *Proceedings of the Annual Technical*
651 *Meeting 1989 and IGCP-246 (1991)*. Department of Geological Sciences, Chiang Mai
652 University, Thailand, pp. 111-140.

653 Simons, W.J.F., Socquet, A., Vigny, C., Ambrosius, B.A.C., Abu, S.H., Promthong, C.,
654 SubaryaSarsito, D.A., Matheussen, S., Morgan, P., and Spakman, W., 2007. A decade of
655 GPS in Southeast Asia: resolving Sundaland motion and boundaries. *J. Geophys. Res.* 112,
656 B06420. <http://dx.doi.org/10.1029/2005JB003868>.

657 Siripunvaraporn, W., Egbert, G., Lenbury, Y., 2002. Numerical accuracy of magnetotelluric
658 modeling: A comparison of finite difference approximations. *Earth Planet Space* 54, 721-
659 725. <http://dx.doi.org/10.1186/BF03351724>

660 Siripunvaraporn, W., Egbert, G., Lenbury, Y., Uyeshima, M., 2005. Three-dimensional
661 Magnetotelluric inversion: data-space method. *Phys. Earth Planet. Inter.* 150, 3-14.
662 <http://dx.doi.org/10.1016/j.pepi.2004.08.023>

663 Siripunvaraporn, W., Egbert, G., 2009. WSINV3DMT: vertical magnetic field transfer function
 664 inversion and parallel implementation. *Phys. Earth Planet. Inter.* 173, 317–329.
 665 <http://dx.doi.org/10.1016/j.pepi.2009.01.013>

666 Sone, M., Metcalfe, I. 2008. Parallel Tetyan sutures in mainland Southeast Asia: New insights
 667 for Palaeo-Tethys closure and implications for the Indosinian Orogeny. *Comptes Rendus*
 668 *Geoscience*, 340, 166–179. <http://dx.doi.org/10.1016/j.crte.2007.09.008>

669 Sone, M., Metcalfe, I., Chaodumrong, P., 2012. The Chanthaburi terrane of southeastern
 670 Thailand: Stratigraphic confirmation as a disrupted segment of the Sukhothai Arc. *Journal of*
 671 *Asian Earth Sciences* 61, 16–32. <http://dx.doi.org/10.1016/j.jseaes.2012.08.021>

672 Tingay, M.R.P., Morley, C.K., Hillis, R.R., Meyer, J., 2010. Present-day stress orientation in
 673 Thailand's basins. *J. Struct. Geol.* 32, 235–248. <http://dx.doi.org/10.1016/j.jsg.2009.11.008>

674 Tullis, J., Yund, R.A., Farver, J., 1996. Deformation-enhanced fluid distribution in deldspar
 675 aggregates and implicates for ductile shear zones. *Geology* 24, 63–66.

676 Tse, S. T., Rice, J.R., 1986. Crustal earthquake instability in relation to the depth variation of
 677 frictional slip properties, *Jour. Geophys. Res.*, 91, 9452 – 9472.

678 Unsworth, M.J., Bedrosian, P.A., 2004a. Electrical resistivity structure at the SAFOD site from
 679 magnetotelluric exploration. *Geophys. Res. Lett.* 31, L12S05.
 680 <http://dx.doi.org/10.1029/2003GL019405>

681 Unsworth, M.J., Bedrosian, P.A., 2004b. On the geoelectric structure of major strike-slip faults
 682 and shear zones. *Earth Planets Space* 56, 1177–1184. <http://dx.doi.org/10.1186/BF03353337>

683 Umino, N., Ujikawa, H., Hori, S., Hasegawa, A., 2002. Distinct S-wave reflectors (Bright spots)
 684 detected beneath the Nagamachi-Rifu fault, NE Japan, *Earth Planets Space*, 54. 1021 – 1026.

685 Uttamo, W., Elders, C., Nichols, G., 2003. Relationships Between Cenozoic Strike-Slip Faulting
 686 and Basin Opening in Northern Thailand. *Geological Society Special Publication* 210, 89-
 687 108. <http://dx.doi.org/10.1144/GSL.SP.2003.210.01.06>

688 Wang, J., Zhao, D., Yao, Z., 2013. Crustal and uppermost mantle structure and seismotectonics
 689 of North China Craton. *Tectonophysics* 582, 177–187.
 690 <http://dx.doi.org/10.1016/j.tecto.2012.10.004>

691 Wannamaker, P.E., Jiracek, G.R., Stodt, J.A., Caldwell, G., Gonzalez, V.M., Mcknight, J.D.,
 692 Porter, A.D., 2002. Fluid generation and pathways beneath an active compressional orogen,
 693 the New Zealand Southern Alps, inferred from magnetotelluric data. *J. Geophys. Res.* 107,
 694 ETG 6-1–ETG 6-20. <http://dx.doi.org/10.1029/2001JB000186>

- 695 Wannamaker P.E., Evans, R.L., Bedrosian, P.A., Unsworth, M.J., Maris, V., McGary, R.S.,
696 2014. Segmentation of plate coupling, fate of subduction fluids, and modes of arc
697 magmatism in Cascadia, inferred from magnetotelluric resistivity. *Geochem. Geophys.*
698 *Geosyst.* 15, 4230-4253. <http://dx.doi.org/10.1002/2014GC005509>
- 699 Wood, S.H., 1995. Late Cenozoic faulting in mountainous regions of low but persistent historic
700 seismicity: Hells Canyon (NW U.S.A.) and Northern Thailand and the meaning of active
701 fault, in IUGG XXI General Assembly, Abstracts Week B, B344.
- 702 Wood, S.H., 2001. Slip-rate estimate from offset streams, valley volumes, and denudation rate:
703 Mae Chan Fault, Northern Thailand, *Eos, Trans. Am. Geophys. Un.*, **82**, 932.
- 704 Wood, S.H., Singharajwarapan, F.S., Bundarnsin, T., Rothwell, E., 2004. Mae Sai Basin and
705 Wiang Nong Lom: radiocarbon dating and relation to the active strike-slip Mae Chan Fault,
706 Northern Thailand. In: Rieb, S., Wongpornchai, P., Chantprasert, S. (Eds.), *Proceedings of*
707 *the International Conference on Applied Geophysics*. Chiang Mai University, Chiang Mai,
708 Thailand, pp. 60–69.
- 709 Wood, S.H., Singharajwarapan, F.S., 2014. Geothermal systems of northern Thailand and their
710 association with faults active during the Quaternary. *Geothermal Resources Council*
711 *Transactions* 38, 607-615
- 712 Wood, S.H., Wood, L.R., Ziegler, A.D., 2015. Natural degradation of earthworks, trenches, walls
713 and moats, Northern Thailand. *Journal of Field Archaeology* 40, 675-694.
714 <http://dx.doi.org/10.1080/00934690.2015.1103645>
- 715 Zhao, D.P., Kanamori, H., Negishi, H., Wiens, D., 1996. Tomography of the source area of the
716 1995 Kobe earthquake: evidence for fluids at the hypocenter? *Science* 274, 1891-1894.
717 <http://dx.doi.org/10.1126/science.274.5294.1891>
- 718 Zhao, D.P., Tani, H., Mishra O.P., 2004. Crustal heterogeneity in the 2000 western Tottori
719 earthquake region: effect of fluids from slab dehydration. *Phys. Earth Planet. Inter.* 145,
720 161-177. <http://dx.doi.org/10.1016/j.pepi.2004.03.009>

721

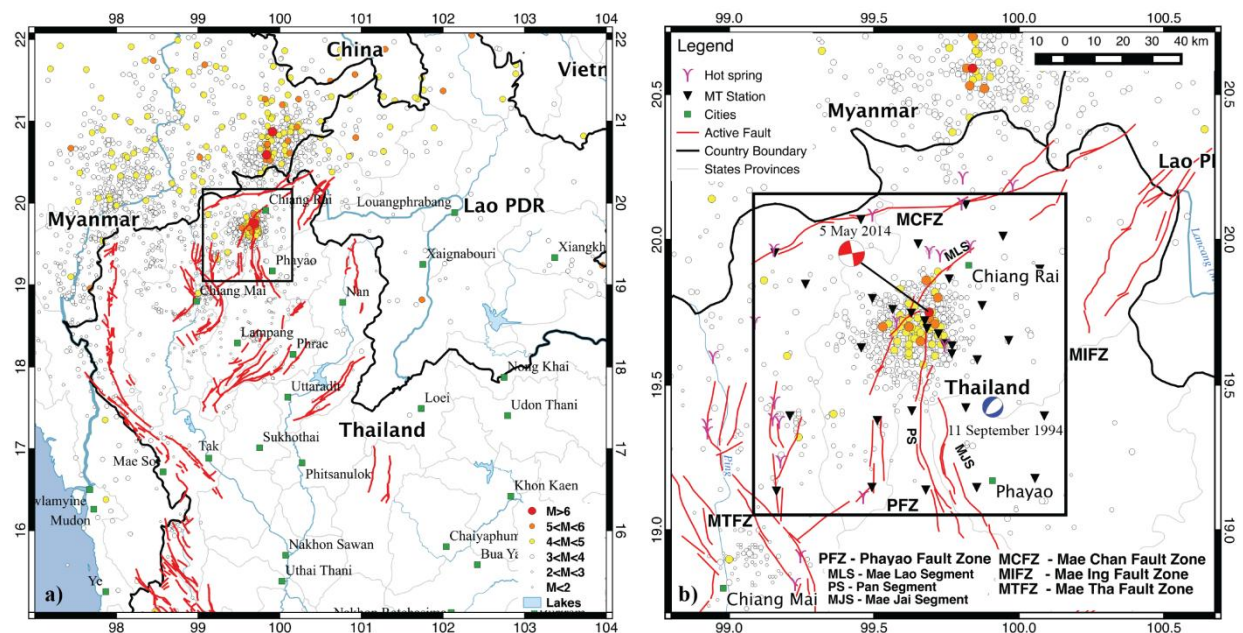
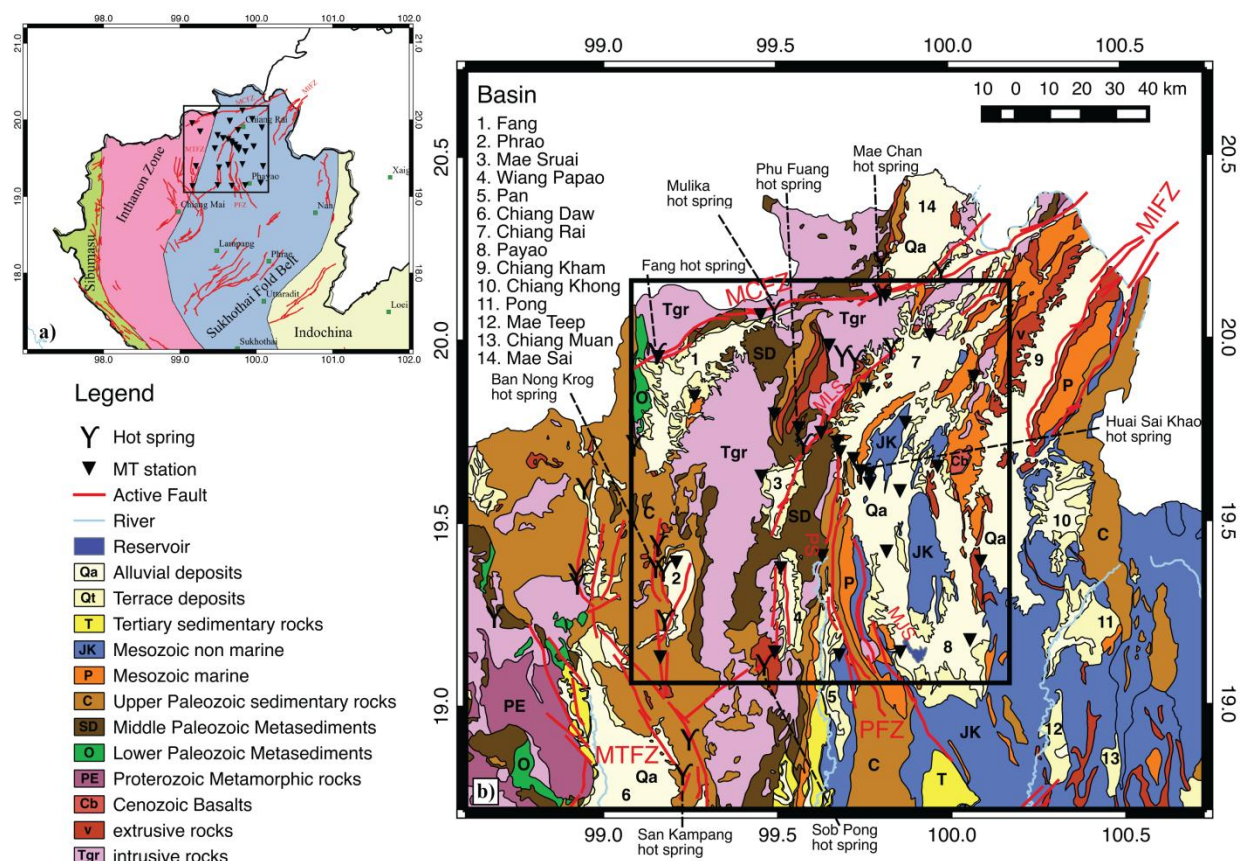


Fig. 1. (a) Northern Thailand and its neighboring countries with fault traces (red solid line) and seismicity from the TMD (from January 2007 – October 2016). (b) shows the study area in more detail. Triangles are the locations of the MT survey. Focal mechanisms of the 5 May 2014 (red) and 11 September 1994 (blue) are derived from Noisagool et al. (2016) and ISC (2012), respectively. The rectangles in (a) and (b) show the study area. PFZ is the Phayao Fault Zone divided into three segments, PS: Pan Segment, MLS: Mae Lao Segment and MJS: Mae Jai Segment. Legends are displayed inside the Figure.

740



741

742 **Fig. 2.** (a) Tectonic setting of northern Thailand (after Mecalfe, 2013). (b) Regional geology
 743 covering the area of the study (rectangular block). The triangles are the locations of the MT
 744 stations.

745

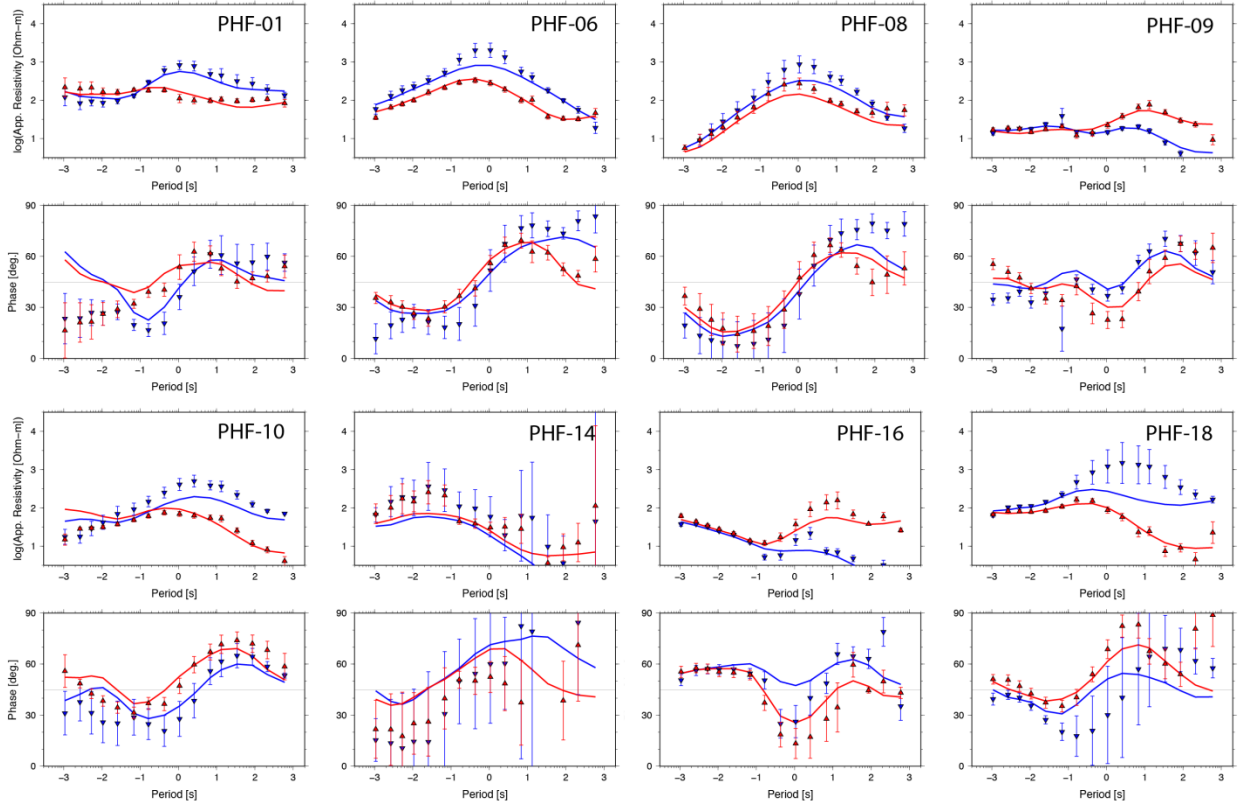


Fig. 3. Selected apparent resistivities (Ω m) and phases (in degrees) as a function of \log_{10} periods (seconds) computed from the off-diagonal impedance tensor at various locations acquired in the locations marked as blue crosses in Fig. 2. Red is xy and blue is yx mode. The upward and downward triangles and error bars are from field measurements, and the solid lines are the calculated responses generated from the inverted model shown in Fig. 5.

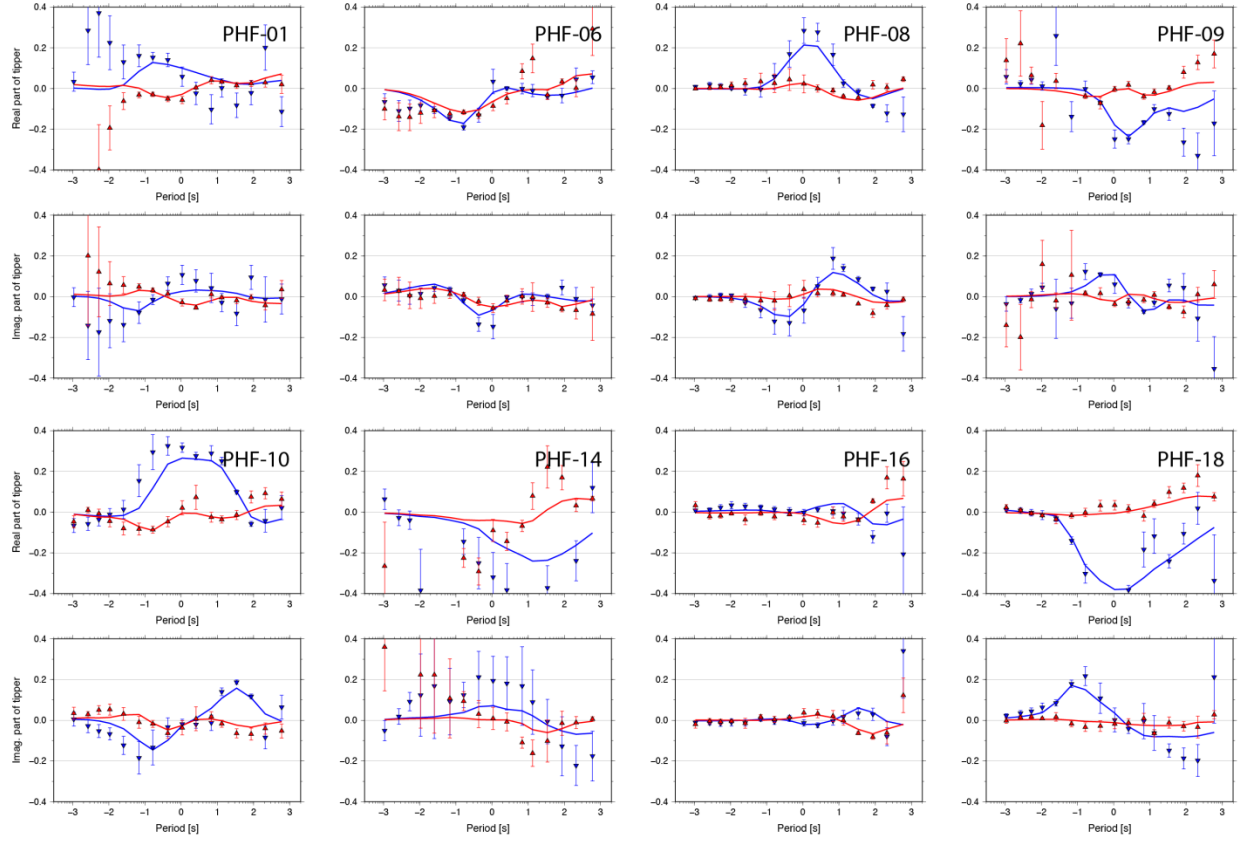


Fig. 4. Real and imaginary parts of the vertical magnetic transfer functions (tipper) as a function of \log_{10} periods (seconds) at various locations acquired in the locations marked as blue crosses in Fig. 2. Red is zx and blue is zy mode. The upward and downward triangles and error bars are from field measurements, and the solid lines are the calculated responses generated from the inverted model shown in Fig. 5.

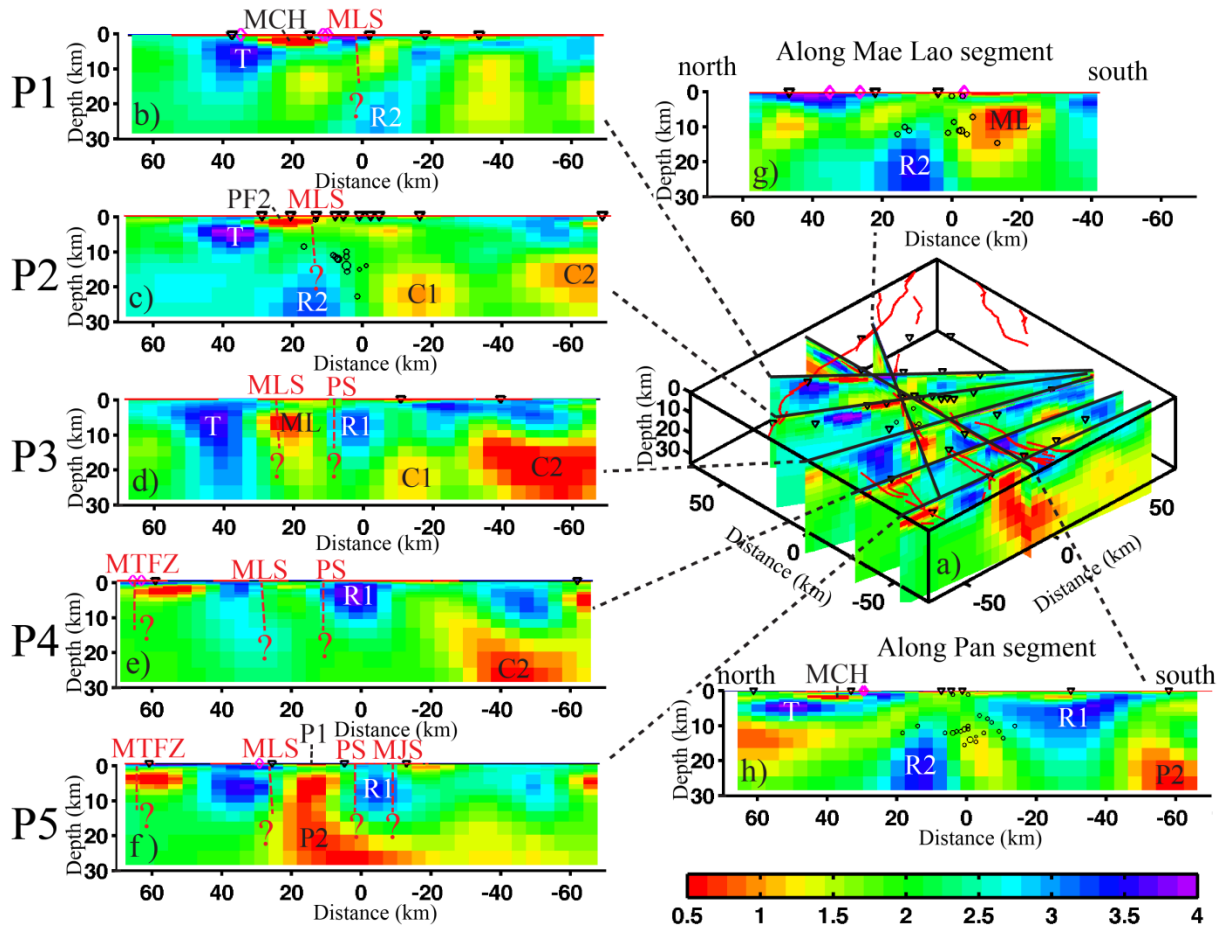


Fig. 5. The final inverted model and their cross sections. Epicenters (Noisagool et al., 2016) were projected with 10 km bins (5 km each side of the profile). The color bar is the \log_{10} resistivity in $\Omega \cdot m$.

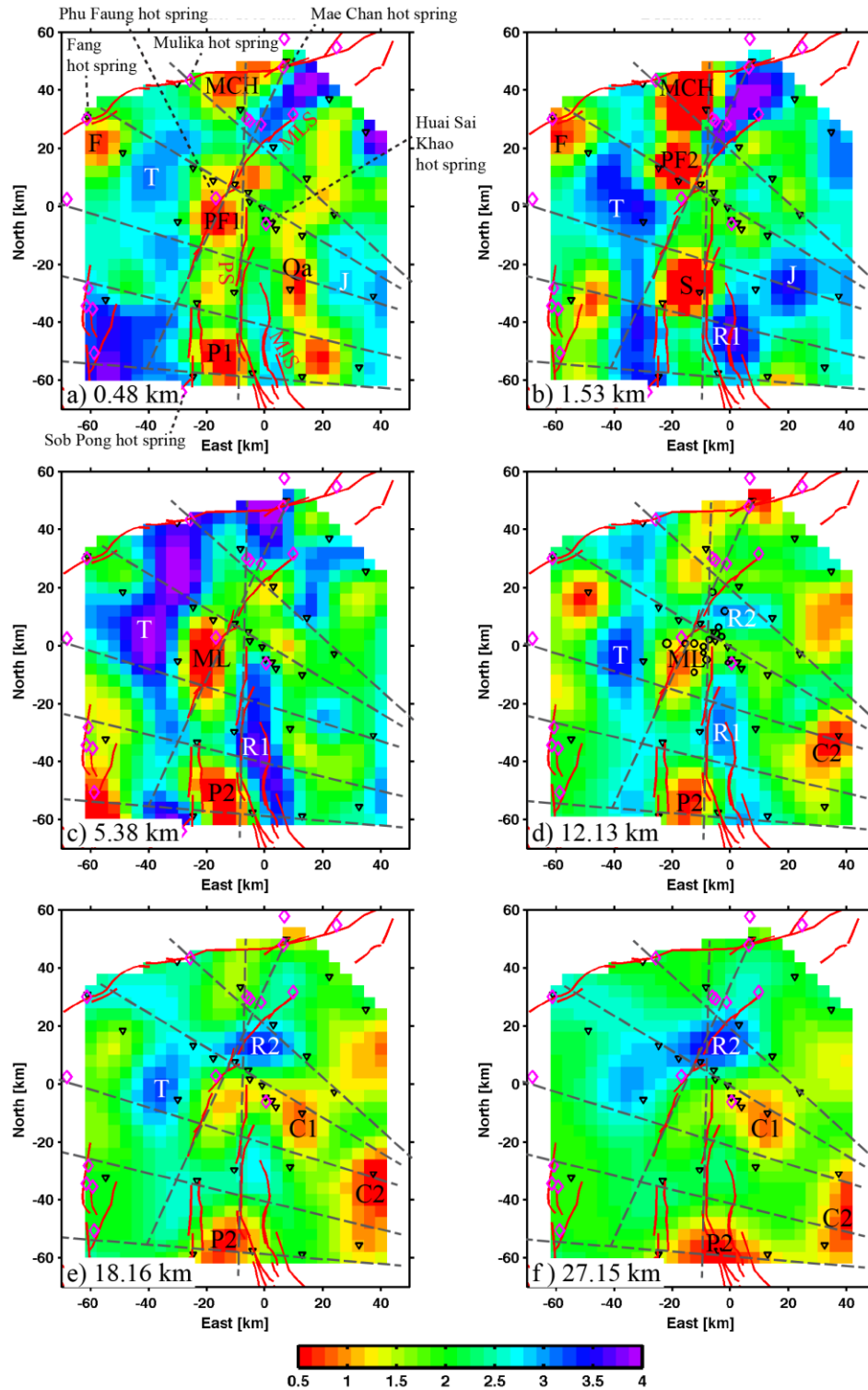


Fig. 6. Top view of the final inverted model (Fig. 5) at various depths: (a) 0.5 km, (b) 1.5 km, (c) 5.4 km, (d) 12.1 km, (e) 18.1 km and (f) 27.1 km. MT locations are marked as black triangles, hot springs are pink diamonds. Dashed lines indicate the locations of the cross section in Fig. 5. The color bar is the \log_{10} resistivity in $\Omega \text{ m}$.

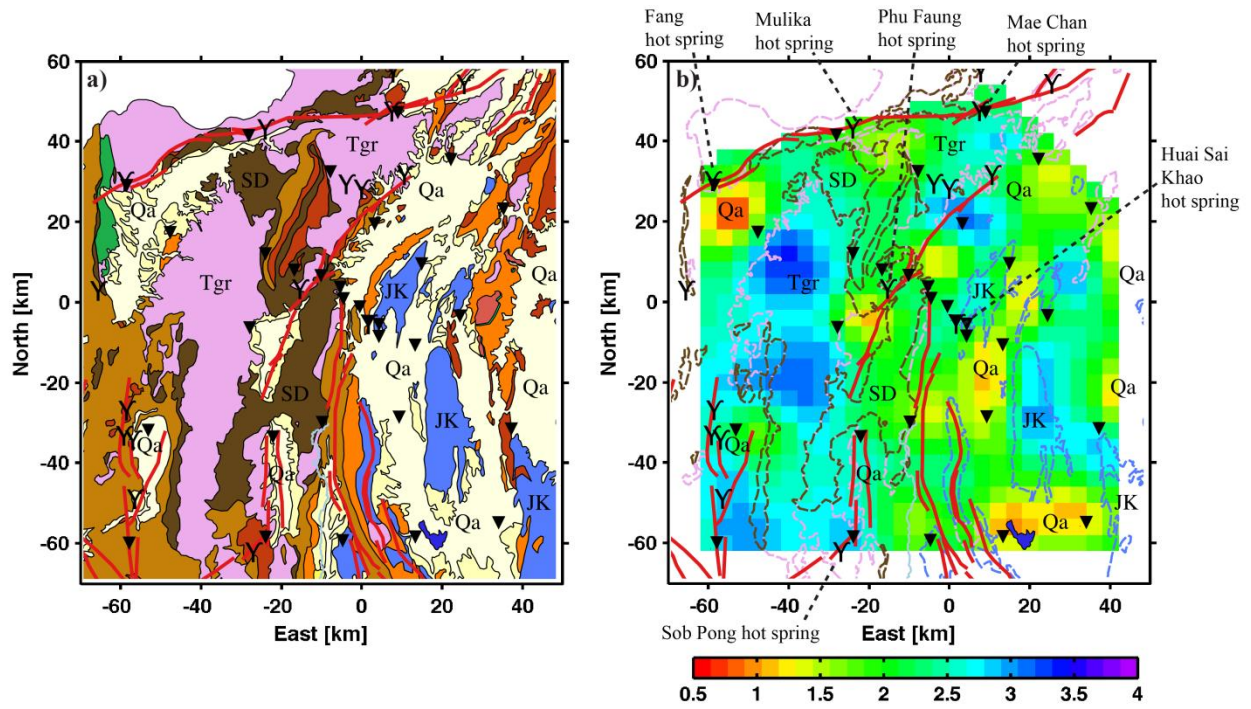


Fig. 7. A comparison of (a) the surface geology with (b) a 50 m depth slice of the final inverted model (Fig. 5). The color bar is the \log_{10} resistivity in Ω m.

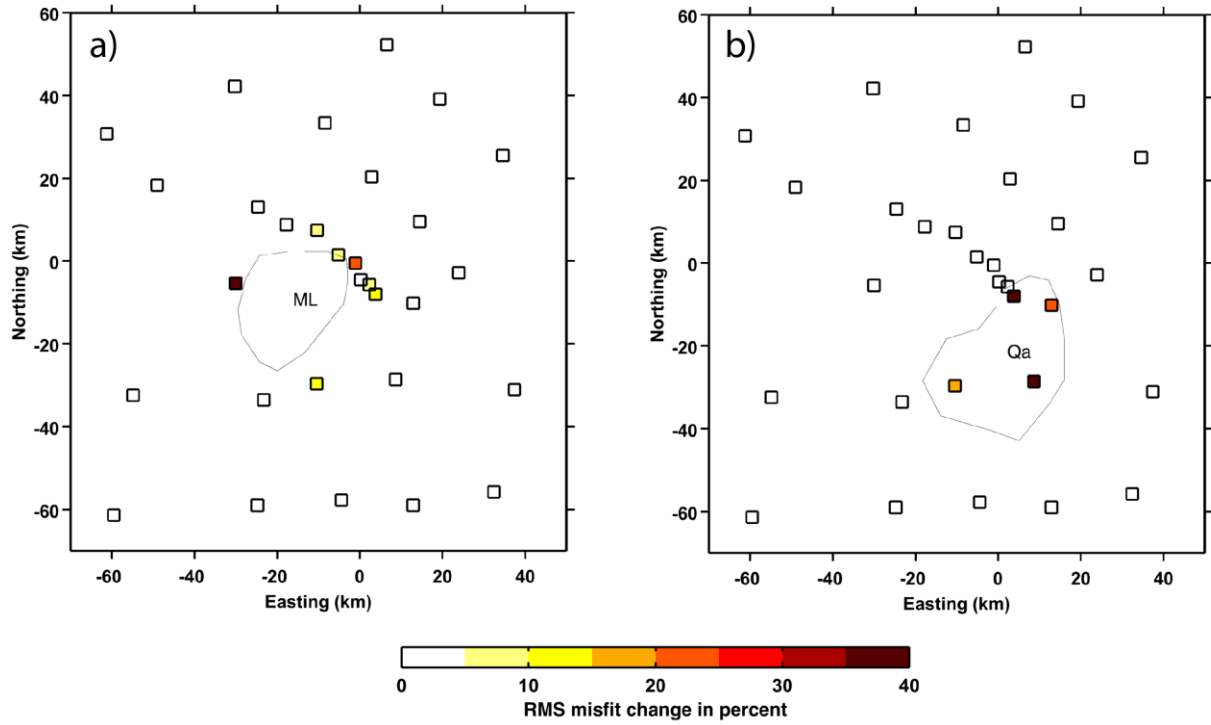


Fig. 8. Plots of relative change of RMS misfit of each station in percent (a) after replacing the ML conductor of the inverted model (Fig. 5 – 7) with the background resistivity, and (b) after replacing Qa conductor with the background resistivity.

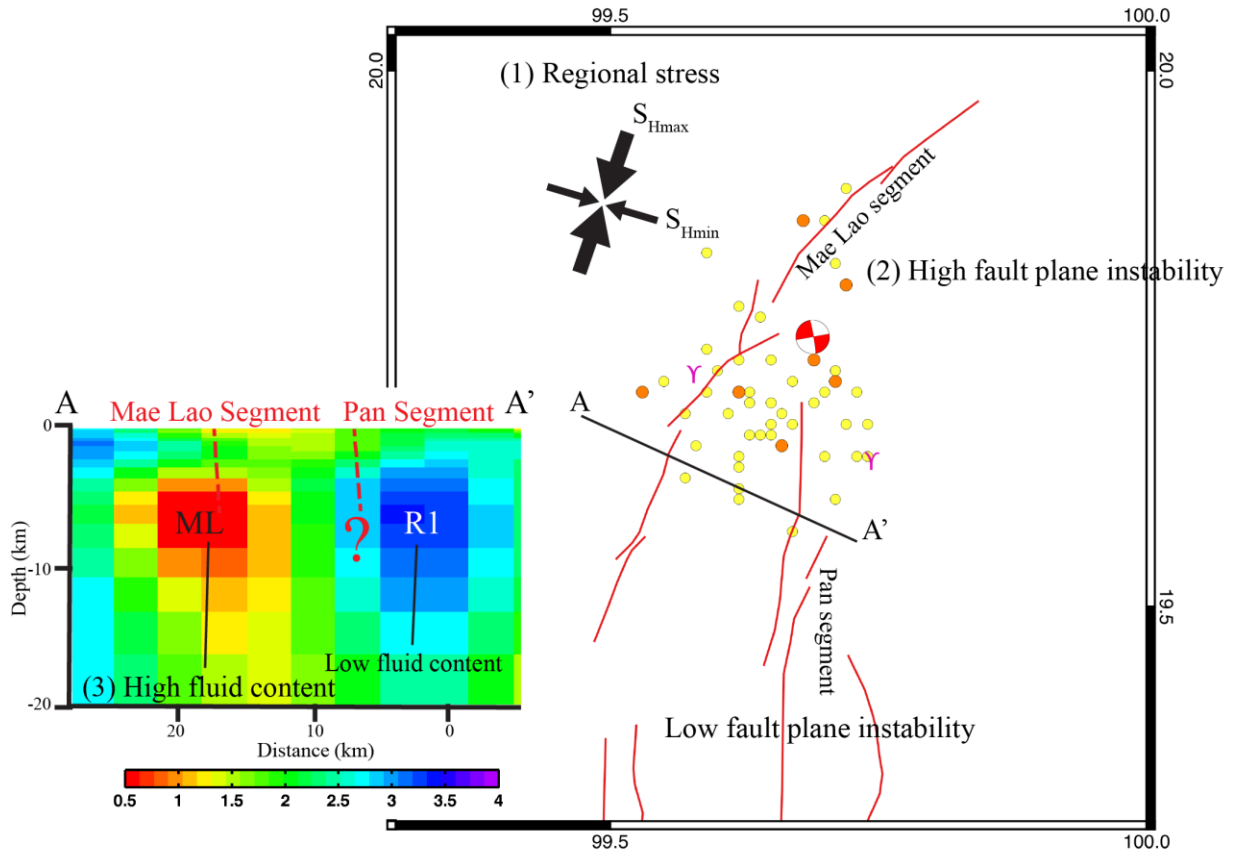


Fig. 9. A diagram explaining a hypothesis about the cause of the 5 May 2014 main shock. (1) A pre-existing tectonic stress is continuously being exerted to the northern Thailand region. (2) The Mae Lao Segment (MLS) and the Pan Segment (PS) have different geometry resulting in a higher fault plane instability for the MLS, and lower fault plane instability for the PS. (3) High fluid content from the low resistivity zone is found next to the MLS, but not the PS. The combination of (2) and (3) on the MLS helps to lower the maximum frictional strength of the MLS fault. This makes the MLS fault weaker relative to that of the PS. When accumulated tectonic stress (1) becomes large, it will make the MLS slip first and so produce the main shock.